Tackling Key Engineering Challenges in Liquid Metal Batteries: Temperature and Mass Transport

by

Rakan F. Ashour

Submitted in Partial Fulfillment of the

Requirements for the Degree of

Doctor of Philosophy

Supervised by Professor Douglas H. Kelley

Materials Science Program

Arts, Sciences and Engineering

Edmund A. Hajim School of Engineering and Applied Sciences

University of Rochester

Rochester, NY

2019

Dedication

To my daughter Ayah Ashour

Table of Contents

Biographical Sketch

Prior to joining the University of Rochester, the author completed his Bachelor of Science degree in Mechanical Engineering at King Abdulaziz University in Saudi Arabia and his Master of Science degree in Materials Science and Engineering at Rochester Institute of Technology (RIT). Afterwards, his passion for applied research lead him to the PhD program in Materials Science at the University of Rochester (UofR). At UofR, he worked as graduate research assistant under the supervision of Professor Douglas H. Kelley. His dissertation work on liquid metal batteries has lead to several collaborative projects with academic and industrial researchers from the U.S. and Europe. Besides his research activity, he has also served as a teaching assistant for the class Practical Electron Microscopy OPT 407 during the period of 2015-2017 and under supervision of Brian McIntyre in The Institute of Optics.

List of Publications:

1. R.F. Ashour, H. Yin, T. Ouchi, D.H. Kelley, D.R. Sadoway, Molten Amide-Hydroxide-Iodide Electrolyte for a Low-Temperature Sodium-Based Liquid Metal Battery, J. Electrochem. Soc. 164 (2017) A535–A537. doi:10.1149/2.1451702jes.

2. R.F. Ashour, D.H. Kelley, A. Salas, M. Starace, N. Weber, T. Weier, Competing forces in liquid metal electrodes and batteries, J. Power Sources. 378 (2018) 301–310. doi:10.1016/j.jpowsour.2017.12.042.

3. R.F. Ashour, D.H. Kelley, Convection-Diffusion Model of Lithium-Bismuth Liquid Metal Batteries, Mater. Process. Fundam. (2018) 41–52.

Acknowledgments

I would like to thank my PhD advisor Doug Kelley for his continual support and guidance through many years of research. Doug is a remarkable individual and a great leader who always welcomes new ideas and is never shy about learning from his students. I also want to thank my colleagues and friends in the lab: Thomas Nevins, Jeff Tithof, Ibrahim Mohammad, Ruy Ibanez and Bitong Wang. Our political discussions will always be remembered.

I would like to thank Professor Donald R. Sadoway for welcoming me in his group at MIT. You have truly inspired my passion for solving big problems and putting science in service to society, and not just for career building. I also would like to thank Takanari Ouchi and Huayi Yin for their great mentorship and help with electrochemical experiments. Many parts of this thesis would not have been possible without their help.

Last, but certainly not least. I'm forever grateful for my family: My wife Jomana, my daughter Ayah, my parents and my brother. Thank you for your love and support.

Abstract

The liquid metal battery (LMB) has already emerged out of the lab bench and into commercial deployment for grid-scale energy storage. However, there are still various engineering challenges that need to be solved in order to improve the LMB’s ability to supply energy at lower cost. This thesis will focus on overcoming the challenges of high operating temperature and mass transport kinetic losses.

To address the problem of high operating temperature, a rigorous experimental research program was undertaken. The feasibility of low and intermediate temperature electrolytes for sodium based liquid metal batteries operating at temperatures below 300°C was investigated. First, the binary NaOH, NaI electrolyte was studied by building and cycling Na|Bi LMBs at temperatures below 280°C. Side reactions leading to capacity fade were identified and their free energies were calculated. Second, the electrochemical feasibility of a novel ternary $NaNH_2$, NaOH, NaI electrolyte for Na|PbBi LMBs was investigated using a three-electrode setup. Cycling voltammetry was used to measure an electrochemical window of 1.3V at 180°C. Thermodynamic calculations were used to determine the limiting oxidation reaction. A second three-electrode setup that employs Na in β''-Al_2O_3 as a reference electrode, eutectic Bi-Pb working electrodes and a Na-Bi-Pb counter electrode was used to investigate the optimal operating conditions for a Na|PbBi LMB. PbBi electrodes were discharged to a predetermined molar concentration of Na and cross-sectioned. Samples were analyzed using energy dispersive x-ray spectroscopy and scanning electron microscopy.

To understand the fundamentals of mass transport in LMBs, a comprehensive experimental model was developed to investigate the flow in PbBi electrodes operating at a temperature between 160 and 180°C. Ultrasound Doppler Velocimetry (UDV) was used to measure the flow in shallow PbBi electrodes at current densities ranging from 0 to 640 mA/cm^2. We identified two competing flow phenomena, namely, thermal convection and electro-vortex flow. A simple dimensionless ratio was also developed to predict their relative strength. The same setup was also used to study the impact of electrical connection and current topology on the emergence of swirling flow in LMBs. Stray axial fields from nearby wires or even that of the earth were found to cause tornado-like flows in shallow PbBi electrodes. The engineering ramifications and design implications of the experimental results are also discussed.

The last part of this thesis serves as an engineering application for the result of our experimental models. A two-dimensional convection-diffusion model was developed to quantify the effect fluid flow on the performance of LMBs. Using a two dimensional stream function to represent thermal convection, we solved the convection-diffusion equation for Li^+ in Bi. Using the obtained concentration profiles, we determined the voltage drop due to the accumulation of Li^+ products at the interface. Increasing flow speed was found to reduce Li^+ accumulation and reduce transport related losses.

Contributors and Funding Sources

Professor Douglas H. Kelley served as an academic advisor and the principle investigator of the liquid metal battery project. Professors Jacob Jorne (Chemical Engineering) served as an internal committee member and provided valuable feedback on the electrochemical experiments on lithium metal oxide batteries. Professor David Foster (Chemical Engineering) provided valuable inputs on the results of chapter 3.

Chapter 2 of this dissertation was done in collaboration with Professor Donald Sadoway who served as co-advisor during my visit to his group at Massachusetts Institute of Technology (MIT). The collaborative project between our lab at Rochester and MIT started with the goal of building novel low temperature sodium based liquid metal batteries. Postdoctoral associates Takanari Ouchi and Huayi Yin helped devise plans to measure electrochemical window of molten salts in chapter 2.

Throughout the period of my research funding for equipment, travel, and supplemental income came from the National Science Foundation under award number CBET-1552182. Stipends and tuition were covered by a scholarship from the Saudi Arabian Cultural mission. The work in chapter 2 was partially supported by TOTAL S. A. and the National Science Foundation (NSF).

List of Tables

List of Figures

Chapter 1: Introduction

1.1 Grid scale energy storage

One of the most sophisticated engineering marvels of the modern day world is the electrical grid. It consists of complex networks of power stations, high voltage transmission and distribution lines. The electric grid was designed back when energy storage did not exist. Therefore, this complicated network operates around the clock to balance electricity production by power stations and consumption by end consumers. In the United States, power is generated from multiple sources and in 2011 coal plants produced 33% of the total 4 trillion kWh of energy consumed on the grid. In the same year, renewable energy sources produced around 13% of the total energy. [1] Even though it is predicted that the total percentage of energy from renewable energy is expected to increase in the coming years, the integration of more renewable energy sources such as solar, wind and tidal waves creates a major challenge due to the inability of existing grids to handle the intermittency of renewable energy sources. In a 2013 report by U.S. department of energy, it was estimated that the United States will require a total of 4 to 5 Tera Watt-hour of storage capacity by 2050.[2] In its current state, the grid handles fluctuations in energy demands above the peak power supply using gas-fired peaker plants. These power-modulating plants are only employed to meet the sudden change in demand. However, these plants are inefficient and in some case are not able to respond to the rapid shift in demand. Energy storage can enable the seemingly impossible task of decoupling supply and demand. By allowing energy to be stored during low demand periods and then releasing it when the demand increases, thus, allowing the grid to operate steadily at a set base-load. Aside from that, energy storage can also play an essential role in frequency modulation and overall grid resilience. More importantly, by allowing wide spread deployment of multiple energy sources on the existing grid; energy storage can also create major economic growth opportunities.

Currently, storage takes a small fraction of about 2.3% of the total energy produced with pump-hydro representing 95% of total storage capacity. [2] Even though pump-hydro is considered an efficient and cost effective technology for storing large amounts energy, it is still geographically constrained. Other existing technologies include compressed air energy storage (CAES), electrochemical capacitors, flywheels and batteries. It is important to note that the choice of one technology over the other depends on the target application. That is, not all energy storage technologies compete for the same application. For example, electrochemical capacitors and flywheels' target market is in high power applications such as frequency regulation and power quality, due to their ability to discharged on a time scale of a few seconds. Batteries on the other hand, such as lithium ion, sodium-sulfur and liquid metal batteries target markets are in renewable energy integration and load shifting where discharge time is measured in hours.

According to the department of energy, current and future energy storage technologies should focus on cost reduction and competitiveness (unsubsidized) as well as the ability to integrate with existing infrastructure. Similarly, the US advanced research projects agency (ARPA-e) has set a target cost of 100 $/kWh for an energy storage technology to be considered viable for grid scale storage. Therefore, it's important to consider where current technologies stand in terms operational energy and power cost. In figure 1, the capital cost of energy is plotted against the power cost. Here one must consider that there are two target applications for storage technologies: high power and high energy. By considering the ARPA-e's target power cost of 1000 \$/kW, [3] then we can draw two lines set by the target power and energy cost. Here every technology that falls to the left of the 100 \$/kWh line are considered viable for high-energy applications such as renewable energy integration and decoupling supply and demand. In this case the most competitive technologies are the liquid metal battery, compressed air and pumped hydro. Similarly, by considering all technologies that fall around the 1000 \$/kW line, we see that several technologies are considered economically viable such as the liquid metal battery, flow batteries, sodium-sulfur (Na-S), flywheels and capacitors.

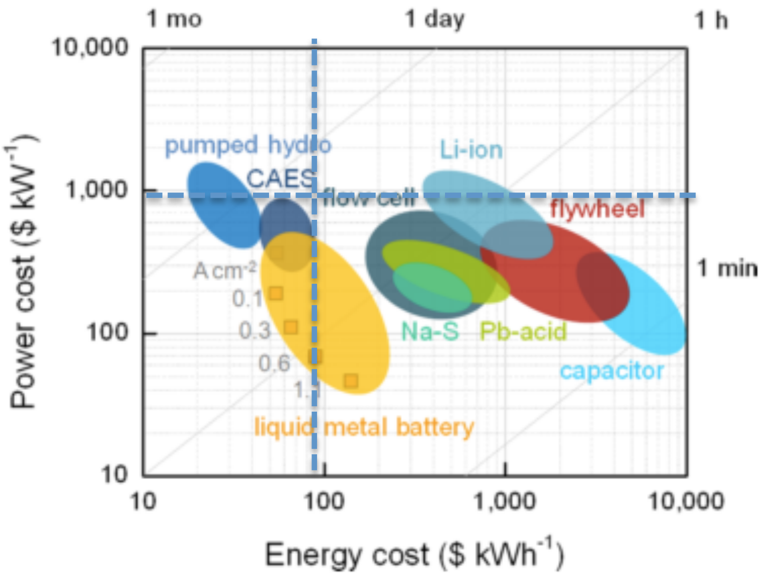

Figure 1. Energy cost vs. power cost of various energy storage technologies. Liquid metal battery cost is calculated for a Lithium lead antimony battery operating at different current densities. Adopted and modified from references [4,5]

To this day, technologies that appear to fall outside the target energy cost such as lithium ion batteries are being commercially deployed on hundreds of Mega watt-hour scale. This however is only made possible through billions of dollars in subsidies by the

US government. In fact, an estimated 27 billion dollars in annual government subsidies is required to drop the energy cost of lithium ion batteries to 300 $/kWh.[6] It's important to note that the price point for lithium ion batteries has already dropped from 600 $/kWh back in 2013 to 273 $/kWh.[7] It is therefore clear that there are tremendous opportunities for technologies that are able to reduce the operating cost to 100 $/kWh.

Besides the initial capital energy cost, another way to measure the feasibility of a technology for grid scale storage is to consider the energy cost per cycle. In this case the initial cost is normalized by the anticipated life cycle. For some technologies such as pumped hydro, it is difficult to estimate the operational life cycle. But, for technologies such as the liquid metal battery, lead acid and lithium ion it is interesting to see how a battery with an extended life cycle can be more appealing. In Table 1, the average energy price is normalized by the average life cycle of each battery. Interestingly, the price per cycle for lithium ion batteries is much less than that of lead acid batteries.

Table 1 Normalized prices of selected battery systems

	Liquid metal battery	Lead acid	Sodium sulfur	Lithium ion
Price $/kWh	150	250	450	273
Life cycle	10,000	1000	4500	3000
$/kWh^{-1} cycle^{-1}	0.015	0.25	0.1	0.091

From table 1.1, one might see that there are two possible approaches that existing technologies can improve on to become viable for grid scale storage. One is reducing the overall capital cost of the system or by enabling a longer life cycle.

1.2 Electrochemical energy storage

1.2.1 Electrochemistry notations and terms

The term electrochemical energy storage covers the technological field that uses electrochemical reactions to produce electricity. This can include batteries and fuel cells. Even though the performance of the aforementioned electrochemical devices might seem drastically different, they all follow the same thermodynamic principles and are essentially made of the same components. In principle, an electrochemical device consists of two half cells separated by an ionic conductor (electrolyte). The term half-cell stems from the fact that it takes two simultaneous reactions to make an electrochemical device. In one half cell, a reaction involving the release of electrons is called an *oxidation reaction*. Similarly, the other half-cell reaction involves the acceptance of electrons and is given the term *reduction reaction*. The term *electrolyte* is given to the medium that separates the two half-cell reactions and allows ions to be channeled through. In the absence of this ionic conductor, half-cell reactions occur in direct contact and electrons are exchanged between chemical species instead of being released into an external circuit and the end result is a chemical reaction.

The origin of electrochemistry terms dates back to the 1830's when Michael Faraday was experimenting with the first electrochemical cell. [8] In his book titled "The fundamental laws of electrolytic conduction: memoirs" [9] he proposed the term electrode as any body of matter, whether of liquid gas or solid that decomposes in the direction of electric current. The term electrode combines two Greek words, namely (elektron) meaning amber and (hodos) meaning away. Other terms such as anode and cathode were development by William Whewell who also used a Greek word (anodos) meaning up and away to describe the location from which electrons are released.[10] Later, the term anode became a standard term for describing the location where oxidation reaction happens. Similarly, the term cathode describes the location where electrons are accepted or where a reduction reaction occurs.

An electrochemical reaction involves transfer of charge across a known phase boundary, normally an electrode electrolyte interface. A standard electrochemical convention to identify the different components in an electrochemical cell is to use a solid vertical line. For example, if a battery is comprised of anode of metal A, a cathode of metal B and an electrolyte E, then the electrochemical notation of this battery is written as:

$$A|\ E\ |B \qquad (1.1)$$

Similarly, multi-elements within a single half-cell are separated by comma as:

$$A, D|\ E\ |B \qquad (1.2)$$

1.2.2 Overview of existing technologies

Lead-Acid batteries

The first commercial application of lead acid batteries was in the field of automotive engineering during the early 1890's. [11] Since then, a great deal of research and development contributed to the enhancement of the performance of these batteries. However, the basic operating principle remains unchanged. A typical cell consists of a lead (Pb) negative electrode, lead oxide (PbO_2) positive electrode and an electrolyte composed of 30% sulfuric acid (H_2SO_4) in water. In addition to the three main components, a separator is usually used to prevent an electrical short that might result from dendritic growth of lead. During discharge, Pb is oxidized at the anode to form Pb^{+2}, which then recombines with sulfate cations to form $PbSO_4$. At the cathode, reduction of PbO_2 occurs to form $PbSO_4$. The anodic and cathodic side reactions are shown in (1.1) and (1.2) respectively.

$$Pb + H_2SO_4 \rightarrow PbSO_4 + 2H^+ + 2e^- \quad (1.3)$$

$$PbO_2 + 2e^- + H_2SO_4 + 2H^+ \rightarrow PbSO_4 + 2H_2O \quad (1.4)$$

The open circuit voltage of this battery is 2 volts and is usually discharged to a shallow depth of discharge (less than 50%) to avoid irreversible volume changes that can cause premature failure. The main advantage of lead acid batteries lies in the low cost of lead and high rate capability. In addition, manufacturing is considered relatively inexpensive when compared to technologies such lithium ion. However, even with shallow discharge, the best performing lead acid batteries are expected to last up to 1000 cycles, making them less than ideal for grid scale storage.

Lithium ion batteries

Lithium ion batteries are energy dense devices and pack more than 200 Wh kg^{-1}. This makes them ideal from consumer devices as well as transportation applications. The first commercial appearance of lithium ion batteries was in 1991. Since then the global market for lithium ion batteries has grown exponentially. In fact, in 2015, the market size for lithium ion batteries has reached 9 billion $ in the United States alone. [12]

Lithium ion batteries operate through an intercalation mechanism where lithium ions are exchanged between two electrodes with known crystal structure separated by a non-aqueous electrolyte. A common choice for anode material includes graphite (C_6). Similarly, common cathode materials include lithium cobalt oxide ($LiCoO_2$) and lithium iron phosphate ($LiFePO_4$). For lithium battery composed of carbon anode and lithium copper oxide cathode, the battery discharges through the following reaction:

$$Li_xC_6 \rightarrow C_6 + x\,Li^+ + xe^- \qquad (1.5)$$

$$CoO_2 + x\,Li^+ + e^- \rightarrow Li_xCoO_2 \qquad (1.6)$$

Where x represents the number of Li^+ ions removed from the graphite structure. During charge, the reaction is reversed and lithium is inserted back in between the graphite layers. During extended cycling, volume changes in the graphite electrodes can lead structural degradation, which eventually lead to capacity fade and battery failure. Another failure mechanism is through uncontrolled growth of a branching structure of lithium metal between the positive and negative electrode. This branching structure is given the term *dendrite* and is part of the reason why lithium ion batteries are not able to operate at high rates.[13]

Lithium ion batteries exhibit extremely high energy density and high open circuit voltage of 3.8 V. Moreover, some batteries can have an impressive life span of up to 5000 cycles with limited depth of discharge. However, the biggest obstacle holding back lithium ion deployment in grid scale storage is the high capital cost. Recent price projections by Bloomberg new energy finance estimates the price of lithium ion batteries to reach the 100 $/kWh by 2025.[7]

Sodium-Sulfur batteries

During the early 1960's, Ford Motor Company invented the sodium sulfur battery with molten sodium (Na) as a negative electrode and sulfur (S) as a positive electrode. The battery uses a solid ceramic electrolyte called beta alumina (β-Al_2O_3) and operates at a temperature of 300 °C to keep both electrodes in a liquid state. During operation, sodium atoms (Na) oxides on the anode to form Na^+ and electrons are released to an external circuit. Na^+ ions travel through the solid electrolyte to react with sulfur (S) to form sodium poly-sulfide (Na_2S_4). The overall discharge reaction is written as:

$$2Na + 4S \rightarrow Na_2S_4 \qquad (1.7)$$

The patent for sodium sulfur batteries was sold to the Japanese company NGK. Since the year 2000, sodium sulfur batteries have been deployed for grid scale storage in Japan with more than 245 MWh of installed capacity in Japan. However, interest in this technology dropped after the fire incident of Tsukuba, Japan in 2011. [14] The battery has an open circuit voltage of 2 volts and can have an extended life span of 4500 cycles if the depth of discharge is limited to 80%. However, the biggest challenges facing these batteries are the mechanical durability of the solid electrolyte as well as their high cost (>450$/kWh).

1.3 The liquid metal battery

The inspiration for a battery that is 100% liquid comes from an electrochemical process that proved to be extremely successful on an industrial scale. This process is the Hall-Heroult and it's used world wide for aluminum (Al) extraction from alumina (Al_2O_3) dissolved in a bath of molten salt. Before this process, aluminum was considered a precious metal and its price was higher than that of gold.[15] Inspired by the Hall-Heroult process, General Motors investigated the possibility of creating an all-liquid battery that can be thermally charged using the excess heat from nuclear reactors. These cells were given the name *thermally regenerative cells.* The first thermally regenerative cells were built in 1960 and used Na|Sn electrodes with molten halides (NaCl, NaI) to operate at a temperature of 700 ^oC with an open circuit voltage of 0.4 V. In 1967, Argonne national labs produced Na|Bi regenerative cells operating at 580 ^oC with an open circuit voltage of 0.75 V. These cells demonstrated impressive rate capability and were able to discharge at current densities up to 650 mA cm^{-1}. Unfortunately, work in the field got discontinued after β-Al_2O_3 was discovered by Ford and research focused on solid electrolyte.

It was not until 2006 when Donald Sadoway and his group at Massachusetts Institute of Technology (MIT) resurrected the all-liquid design. Sadoway was interested in capturing the economic benefits of the Hall-Heroult process and the rate capabilities of thermally regenerative cells to produce an all-liquid battery that can be electrically charged. The first successful demonstration of the concept employed magnesium (Mg) as a negative electrode and antimony (Sb) as a positive electrode.[16] The battery displayed an open circuit voltage of 0.6 V and was able to operate at current densities up to 200 mA cm^{-1}. Since then several electrode couples were tested including Li|Pb,Sb,[17] Li|Bi [18] and Na|Pb,Bi. [19] Following the successful demonstration of a battery capable of providing energy at a cost less than 150 $/kWh, the start-up company AMBRI was born in 2012 with more than 50 million dollars in equity from investors such as the French energy giant Total and Bill Gates. Since then, the company has been pushing hard on commercializing liquid metal batteries for grid scale storage.

Liquid metal batteries can be made of several elements from the periodic table. However, the simple requirement is to use two molten metals with different electronegativity separated by molten salts. Here, electronegativity refers to the tendency of a material to donate or accept electrons. A simple diagram for a liquid metal battery in a discharge and charge state is shown in figure 2.

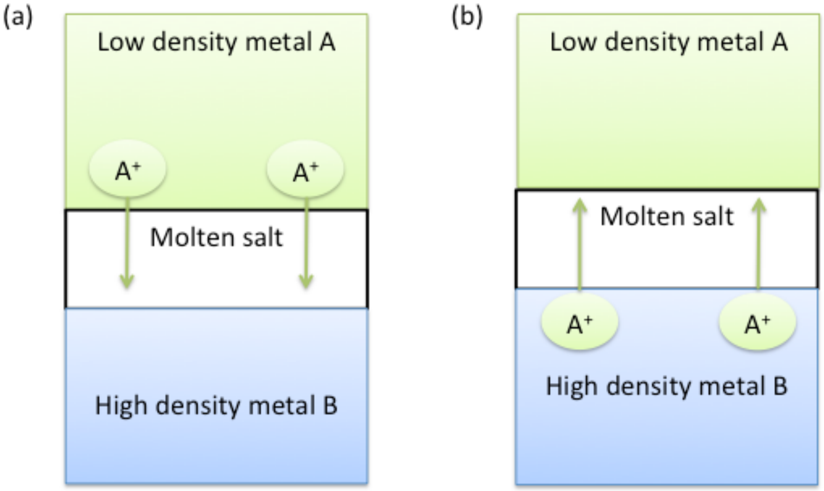

Figure 2 Schematic representation of a liquid metal battery in a state of (a) discharge and (b) charge.

The anode and cathode materials are selected to allow for an all-liquid operation at a temperature less than 1000 ^{o}C. Typically, cathodes are selected from electronegative elements such as bismuth (Bi), lead (Pb), antimony (Sb) and zinc (Zn). On the other hand, anodes are selected from electropositive elements such as alkaline or alkali metals. The two molten metals are separated by a molten salt mixture containing ions of the same type of metal chosen as an anode. The three layers self-segregate based on density, which allows for easy and inexpensive assembly.

The voltage of the battery varies depending on the thermodynamic driving force of the selected materials. During discharge, the anode metal is oxidized and electrons are released to power the grid. The metal ions then travel through the electrolyte and reach the cathode where they form an alloy. The overall discharge reaction is written as:

$$A \rightarrow A \text{ (in B)} \qquad (1.8)$$

Theoretically, liquid metal batteries restore their original state after each discharge – charge cycle due to the absence of any solid surfaces or separators. Hence, they are expected to have an extended life span exceeding 10,000 cycles. However, some batteries did not show any measurable capacity fade over thousands of cycles which makes it hard to forecast the actual life cycle.[18]

1.4 Objectives

The goal of the present work is to overcome key engineering challenges that are pushing back the deployment of liquid metal batteries in grid scale storage. These challenges include both thermodynamics as well as kinetics. Hence, tackling these challenges requires a highly interdisciplinary approach that draws on knowledge from fields such as electrochemistry, materials science, physics and applied mathematics. In the following paragraphs, I shall define each challenge and the approach taken to address each one.

1.4.1 Reducing operating temperature

In September of 2015, the startup company AMBRI was forced to cut staff and push back on the first commercial field deployment of liquid metal batteries.[20] According to the company's CEO, the technology has faced an unanticipated hurdle with thermal insulation. The CEO also pointed out that battery seals failed to minimize heat losses during cycling at high temperatures close 500 ^{o}C. Based on this, it is clear that a liquid metal battery operating at a temperature less than 400 ^{o}C would make use of the already known thermal insulation techniques used in systems as the sodium sulfur batteries. Further reduction in temperature below 300 ^{o}C will enable the use of less expensive polymer seals.

In this part of the dissertation, the main focus is on sodium-based systems that operate at temperatures below 300 ^{o}C. Building on the foundational work by Spatocco et al. on the (Na|NaOH,NaI|Bi,Pb) system [3] and the extensive literature on the sodium Castner process, we shall explore the limitations of this system in more detail, identify parasitic reactions that lead to capacity fade and ultimately battery failure. Afterwards, we shall introduce a novel electrolyte comprised of sodium amide ($NaNH_2$), sodium hydroxide (NaOH) and sodium iodide (NaI) for sodium-based liquid metal batteries. [21] Here, research will focus on electrochemical characterization, compositional effects and rate capabilities of this system. The methods used in this section include cycling voltammetry, battery cycling, scanning electron microscopy and energy dispersive x-ray spectroscopy. The outcome of this part of the dissertation will be to have a comprehensive understanding of low temperature sodium based systems kinetic and thermodynamic limitations and be able to make suggestions that can guide future research in the field.

1.4.2 Understanding transport phenomena across scales

Various liquid metal battery chemistries such as Ca|Bi [22] and Mg|Sb [23] were found to be limited by transport in the positive electrode due to the formation of solid intermetallic compound near the electrode electrolyte interface. To understand this phenomenon, previous work relied on simple models that are often one-dimensional that can only apply to small systems where fluid flow is not expected to occur. [24] However, liquid metal batteries are considered more economical when scaled up as the capital cost is inversely related to storage capacity. As a result, commercial batteries are expected to be large enough for transport to be dominated by fluid flow. Therefore understanding the flow behavior at different operating conditions is of high importance. Here, we shall focus on the magneto-hydrodynamics of cathode models with realistic boundary conditions corresponding to working liquid metal batteries. The main experimental technique employed in this section is ultrasound velocity measurement. Other methods include numerical models, scaling laws and linear regression. The outcome of this work will provide fundamental understanding of the role of thermal convection and electromagnetic forces on the flow structure in liquid metal electrodes and allows for building a model that can predict flow speed and structure from electrode geometry and current density.

1.4.3 Linking electrochemistry and magnetohydrodynamics

Going through the literature on liquid metal batteries, one immediately realizes that the community is divided into two groups. One includes electrochemists working on fundamental battery thermodynamics while ignoring the underlying physics dealing with fluid flow. On the other side, we see physicists working on the fluid dynamics of liquid metal batteries without considering its overall impact on battery kinetics. Hence, there exists a communication gap between the two communities. Here we shall attempt to bridge the gap between the two communities by building a two dimensional reaction advection diffusion model. Research will focus on the Li| KCLl,LiCl |Bi system due to the availability of material properties (diffusivity, conductivity, thermal properties) as well as thermodynamic data for electromotive force of lithium in bismuth at different molar fractions. The outcome of this work will represent the first attempt to link electrochemistry and magneto-hydrodynamics in liquid metal batteries. It will also allow for accurate prediction of voltage losses from mass transport, ohmic resistance as well as charge transfer. Correlation between flow structure and intermetallic growth will also be established.

"Science can amuse and fascinate us all, but it is engineering that changes the world."
Isaac Asimov (1988)

Chapter 2: Low Temperature Sodium Based Liquid Metal Batteries.

2.1 Review of Thermodynamics.

Most of what we know about the world of thermodynamics is based on human experiences. We state that energy cannot be created or destroyed; yet we do not really understand why it should be so. For example, Nobel laureate Richard Feynman said in his lectures: " it is important to realize that in modern physics today, we have no knowledge of what energy is." [25] We accept these fundamental laws because they enable us to describe the world around us. They allow us to generate mathematical models and build a physical intuition. Our goal in this section is not to dwell on the philosophical implications of thermodynamics, but rather to use the fundamental laws to understand how different variables affect the behavior of a specific system; in this case, the liquid metal battery.

2.1.1 From the first law to battery voltage.

The first law of thermodynamics states that energy cannot be created or destroyed or simply that we cannot get energy out of nothing. This is expressed mathematically as

$$dU = dQ - dW \tag{2.1}$$

Where dU is the total change in the internal energy of the system, dQ represent the total heat exchanged with the surrounding, and dW is the work done by the system. An example is mechanical work produced by changes in pressure (p) or volume (V) as

$$dW_{mech} = p\, dV \tag{2.2}$$

The second law introduces the concept of entropy which describes the number of possible states or arrangements that a system can exist in. the law states that the total entropy of a system and its surrounding must always increase or remain unchanged. In other words, no thermodynamic process can lead to a negative change in the total entropy. For a reversible process at constant pressure, the change in the system's entropy is described as

$$dS = \frac{dQ}{T} \qquad (2.3)$$

Where dS is the change in entropy, and T is the temperature of the system. By combining the first and second law, we can re-write the change in internal energy as a function of the change in entropy and volume U(S,V)

$$dU = TdS - pdV \qquad (2.4)$$

In electrochemical systems, we often use the Gibbs free energy to quantify energy changes at a given temperature and pressure G(T,p). However, before we attempt to derive a mathematical expression for the Gibbs free energy, it is important to recall another important thermodynamic quantity, namely, enthalpy H(S,p). The mathematical expression for enthalpy is derived by applying a Legendre transform to the internal energy as

$$H = U - \left(\frac{dU}{dV}\right)_S V \qquad (2.5)$$

Hence, we can express the change in enthalpy as

$$dH = TdS + Vdp \qquad (2.6)$$

Enthalpy represents the total amount of heat exchanged in a process. In chemical reactions, the change in enthalpy (dH) represents the heat consumed or given off by a known chemical reaction. In other words, negative values indicate that a reaction is exothermic. On the other hand, positive values indicate an endothermic reaction.

To arrive at the Gibbs free energy, we need to apply another Legendre transform to the internal energy so that we can use G(T,p) instead of U(S,V). This is described mathematically as:

$$G = U - \left(\frac{dU}{dS}\right)_V S - \left(\frac{dU}{dV}\right)_S V \qquad (2.7)$$

Where G is the Gibbs free energy. For an isothermal process (dT=0), we can combine equations (2.4), (2.5), and (2.6), to express the change in the Gibbs free energy as

$$dG = dH - TdS \qquad (2.8)$$

Equation (2.8) is an important mathematical expression and will be used repeatedly in this chapter. The importance of this equation stems from the fact that we can identify possible reactions in a given system by calculating the change in Gibbs free energy. Negative changes in free energy indicate spontaneous reactions, whereas positive changes indicate that energy is needed to initiate the reaction.

Now that we established the relationship between reaction spontaneity and the Gibbs free energy, let us find how free energy is related to electrical potential. To do this, we will need to modify the expression for the internal energy dU in equation (2.1) to include mechanical and electrical work ($dW_{electric}$). After a quick Legendre transform we arrive at the expression:

$$dG = SdT + Vdp - \mathrm{dW}_{\mathrm{electric}} \qquad (2.9)$$

Since most batteries are tested under constant temperature and constant pressure, the expression for the change in free energy reduces to

$$dG = -\mathrm{dW}_{\mathrm{electric}} \qquad (2.10)$$

Equation (2.10) states that the change in free energy is the negative of the work done by the system. To relate equation 2.10 with battery voltage, we recall that the definition of the "Volt" is the energy transferred in Joule per unit charge in coulomb. Therefore battery voltage (E) is related to the Gibbs free energy via

$$E = -\frac{\Delta G}{n\,F} \qquad (2.11)$$

where ΔG is the molar free energy in units of Joules per mole (J/mole), n is the number of electrons exchanged in the reaction, and F is Faraday's constant (96485 coulomb/mole).

Oftentimes we are interested in calculating equilibrium voltage changes with chemical concentration. To do this, we will first introduce the thermodynamics quantity known as chemical potential (μ). This quantity represents the change in free energy with chemical activity (a). Turns out, that deviation in chemical potential from a reference (standard state) is given by a logarithmic relation as

$$\mu_i = \mu_i^o + RT\ \ln a_i \qquad (2.12)$$

where μ_i^o is the standard state (reference) chemical potential of species i, R is the molar gas constant (R=8.314 J.mol^{-1}K^{-1}), and a_i is the chemical activity of species i. By knowing that for a given chemical reaction, the molar free energy ΔG represent difference in chemical potentials of products and reactants, and after a few steps of simple algebra, we arrive at the Nernst equation

$$E = E_o - \frac{RT}{nF} \ln \frac{a_{products}}{a_{reactants}} \qquad (2.13)$$

where E_o is the reference equilibrium voltage. The Nernst equation represents the backbone of modern electrochemistry and describes how the equilibrium voltage of an electrochemical cell changes with chemical concentration. Let us now examine how this equation applies to liquid metal batteries. To do this, let us consider a battery composed of hypothetical elements A|B. The half-cell reactions are given by

$$A \rightarrow A^{+} + e^{-} \qquad (2.14)$$

$$A^{+} + e^{-} \rightarrow A_{in\ B} \qquad (2.15)$$

and the overall reaction is given by

$$A \rightarrow A_{in\ B} \qquad (2.16)$$

Since the same electrochemical reaction occurs on both sides, the equilibrium potential is only due to the difference between the chemical activity of metal A in its elemental form A and its activity in metal B as $A_{in\ B}$. Therefore, from the Nernst equation, the equilibrium voltage for this battery is written as

$$E = -\frac{RT}{nF} \ln a_{A\ (in\ B)} \qquad (2.17)$$

Here we have used the fact the activity of any pure element in itself is always equal to unity. However, if the anode is made of multiple elements (alloys), then the expression above is no longer valid. Thermodynamic mixing rules and extensive modeling would be required to accurately predict equilibrium voltage of multi-element anode materials. Examples of equilibrium cell voltage of multiple electrodes couples are shown in table 2-1.

Table 2 Equilibrium Cell voltage of fully charged liquid metal electrode couples. Values are found in [4] and references therein.

Cathode	Voltage vs. $Na_{(L)}$	Voltage vs. $Li_{(L)}$
Bi	0.74	0.86
Pb	0.47	0.68
Ga	0.2	0.2

2.2 Previous work on sodium based liquid metal batteries.

There's an anti-correlation between abundance of elements and their cost. For example, oxygen is the most abundant element on Earth, and luckily, it costs us nothing to consume. Similarly, aluminum is third most abundant element, right after silicon. It is due to this fact and its low extraction cost that we use aluminum in everyday products such as canned beverages and thin foils. Sodium comes after aluminum on the scale of abundant elements. Consequently, it is one of the cheapest elements per mole basis with a cost of (0.057 \$/mole).[4] Work on molten sodium based batteries dates back to 1958. During that year, Yeager had proposed the concept of *thermally regenerative cells*. The idea was to develop a technology that would use the heat wasted in nuclear reactors to de-alloy two molten metals of different negativities. During discharge the devices would operate like a modern liquid metal battery. However, the major drawback of this concept is that it's subject to thermodynamic limitations during evaporation/condensation. [26] The first scientific publication on thermally regenerative cells appeared in the book that was published by the American Chemical Society back in 1967.[27] Back then, Na|Sn electrode couple were used at a temperature of 700°C. The electrolyte was composed of molten halides (NaCl, NaI). Interest in regenerative cells slowly began to decline in favor of electrically rechargeable batteries. Most notable is the Na|Bi bimetallic cells that were developed by Cairns et al. at Argonne National Labs. The cells used an electrolyte composed of (NaCl,NaF,NaI) to operate at a temperature of 580°C. [28] They had capacities up to 15 Ah and were able to operate at current densities up to 1.1 A/cm^2. However, the cells suffered from severe voltage losses at high discharge rates due to the slow transport of sodium in molten bismuth. In addition, the cells suffered from low coulombic efficiencies (defined as the ratio of discharge to charge capacity) due to the high solubility of liquid sodium in molten halide based electrolytes, which resulted in an increase in the electrical conductivity, and eventually lead to an increase in self-discharge. [4] At this point, the focus began to shift toward the solid-state ionic conductor (β”-alumina), which was invented by Ford Motor Company in 1966.

It was not until 2006 when interest in all liquid batteries resurfaced at Donald Sadoway’s group at MIT. After many years of research and development, Brian Spatocco and colleagues in the Sadoway group attempted to solve the problem of high solubility of liquid sodium in molten halides by using a eutectic salt mixture comprised of sodium hydroxide (NaOH) and sodium iodide (NaI). [19] Using a three electrode setup, Spatocco measured the electrochemical window of the electrolyte to be >2.4 Volt vs. Na, which is substantially higher than the operating voltage of most sodium based LMBs. Furthermore, the same work tested the performance of a Na|PbBi LMB employing this electrolyte and operating at a temperature of 280^{o}C. The cell demonstrated high coulombic efficiency in excess of 90%. However, high capacity fade and low energy efficiency (<40%) was observed during the first 100 cycles. Spatocco argued that the observed capacity loss was due to the formation of a passivation layer of Na_2O. To further reduce the operating temperature, Lalau et al. used the same electrode couple (Na|PbBi) with an ionic liquid composed of 20% Na[TFSI] in [TEA][TFSI] electrolyte. [29] The cell only lasted three cycles and displayed very poor energy efficiency due to the extremely low ionic conductivity of the electrolyte.

2.3 Experimental methods

In this chapter, our experiments focuses on intermediate (250-350 C) and low temperature (<200 C) sodium based liquid metal batteries. Two molten salt electrolytes are tested. Namely, the binary NaOH,NaI , and the ternary $NaNH_2$, NaOH, NaI molten salts for intermediate and low temperature LMBs. In the Binary NaOH,NaI system, our experiments focused on cycling capability of a Na|NaOH,NaI|Bi cells at 280 C, and identifying possible side reactions. In the ternary $NaNH_2$, NaOH,NaI experiments focused on the investigating the electrochemical feasibility of this electrolyte, and identifying optimal operating conditions.

2.3.1 Salt Preparation

A crucial step that comes prior to our electrochemical experiments is drying the salts.

This process ensures the removal of absorbed moisture, which can react chemically with the active material (Na or Li).

In the case of NaOH, drying involves two steps. First, the removal of absorbed moisture through:

$$NaOH.H_2O \rightarrow NaOH + H_2O_{(g)} \qquad (2.18)$$

Simultaneously, another undesirable process occurs where NaOH thermally decomposes to Na_2O through

$$2NaOH \rightarrow Na_2O + H_2O_{(g)} \qquad (2.19)$$

In the study of Yurkinskii et al., [30] the optimal dehydration time ($\tau_{optimal}$) for NaOH was experimentally measured in units of hours, and is found to follow the following equation

$$\tau_{optimal} = 24.416\ \pm 0.937 - (0.0232 \pm 0.0011)\times T \qquad (2.20)$$

where T is the dehydration temperature measured in Kelvin (K). The temperature at which NaOH is dried is chosen to be 550°C or 823K. Hence, the total time required to reach optimal dehydration is >4.5 hours. These conditions are identical to those described by Spatocco et.al, as well as Yurkinskii et al. [3,19,30] Omission of this drying step has been reported to result in strong water reduction signal during cyclic voltammetry of molten NaOH. [19] Similarly, NaI was dried under vacuum at a temperature of 250°C for 12 hours. All salts were dried in a custom made vacuum vessel shown in figure 3. Following the drying process, the salts were crushed and combined according to the desired eutectic composition.

It is important to note that amide based salts ($NaNH_2$) were not dried. Extreme care must be taken when handling $NaNH_2$ as it can violently react with moisture according to

$$NaNH_2 + H_2O \rightarrow NH_3 + NaOH \qquad (2.21)$$

Moreover, $NaNH_2$ can also react with oxygen to form sodium oxide, nitrogen dioxide and water according to

$$4NaNH_2 + 7O_2 \rightarrow 2Na_2O + 4NO_2 + 4H_2O \qquad (2.22)$$

Therefore all amide salts were handled in an argon atmosphere with ultralow O_2 levels.

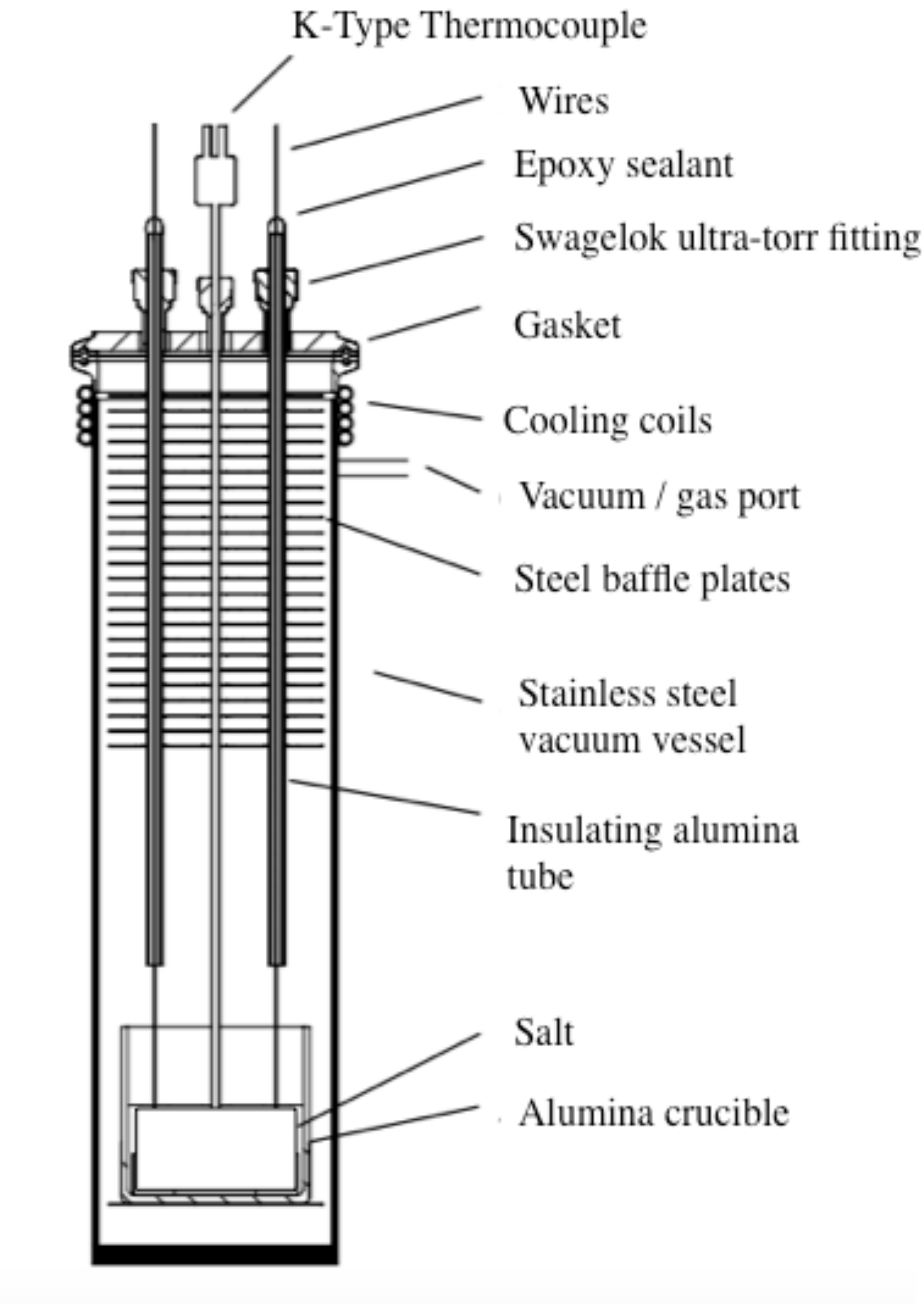

Figure 3 Schematic of the vacuum vessel used for drying salts. Adapted and modified from reference [36]

2.3.2 Electrode Preparation

Similar to the process of handling dried salts, all electrode materials were prepared in a well-controlled argon atmosphere with O_2 levels below 0.5 ppm. Low carbon steel crucibles were used as containers and current collectors due to their corrosion resistant characteristics, as well as their good electrical conductivity. Induction melting was used to prepare the desired alloy composition.

All alumina crucibles, tungsten, low carbon steel, and Monel-400 wires were rinsed thoroughly with acetone and dried under vacuum before going into the argon filled glove box.

2.4 Results and Discussion

2.4.1 The Binary NaOH,NaI system

Our focus in this section is on intermediate temperature sodium based liquid metal batteries. We shall start where others have ended, that is, we will attempt to investigate the limitations of the binary NaOH, NaI electrolyte before we embark on the journey of developing a ternary system. In the work of Spatocco et al., [3,19] the authors suggest that the low energy efficiency observed in their Na|Pb,Bi LMB was due to the slow diffusion of Na^+ ions in the positive electrode. They argue that Pb ions act as a diffusion barrier, which ultimately leads to high transport over-potentials. Furthermore, they attribute the observed capacity fade to unknown side reactions in the negative electrode.

To test these hypotheses, we built and cycled a Na|NaOH,NaI|Bi electrochemical cell. This eliminates the added complexity of Pb spectator ions. Unlike the Na|Pb,Bi ternary system, our experiments can now be better guided by existing an existing binary phase diagram (figure 4).

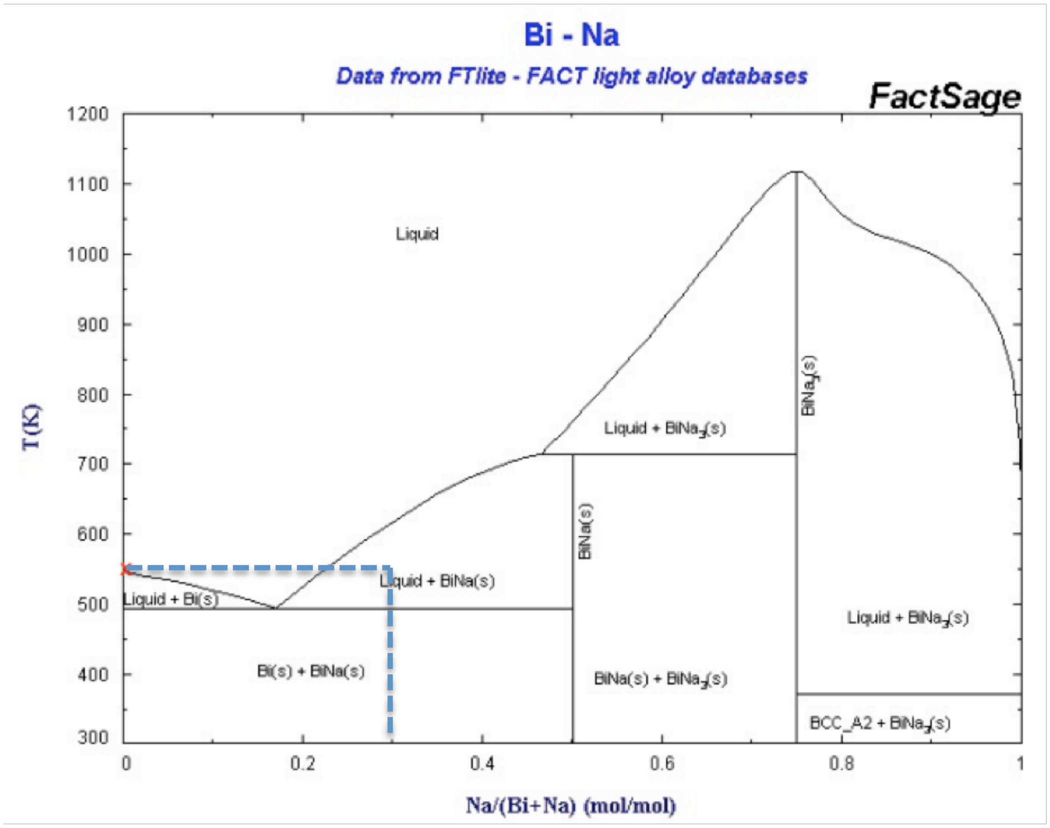

Figure 4 Sodium (Na), Bismuth (Bi) phase diagram generated from open source version of FactSage,[31] Horizontal axis represents molar fraction of Na in Bi. Dashed line shows the starting temperature and range of composition of the tested Na|Bi LMB.

To estimate the mass of Bi, we assumed a layer of height 5 mm that is perfectly wetting the walls of a 2 cm diameter container. Using the geometry of the cell as well as the density of Bi we calculated a mass of 8.9 grams. Now to calculate the mass of Na, we chose a composition of 30% $Na_{in\ Bi}$ as the fully discharged cathode composition. Therefore, knowing we have 0.042 moles of Bi, the total number of moles of Na anode is 0.012, and its mass is 0.295 grams. This gives a total theoretical capacity of 0.3 Ah.

The amount of salt needed is calculated in a similar manner. First, we assume a layer height of 20 mm in the same container. Knowing the approximated volume and density, we calculate the required mass to be 15 grams. Since the eutectic composition of the electrolyte is 80% mole of NaOH, we can calculate the total molarity of the mixture from

$$N = \frac{total\ mass}{0.8\left(\frac{mole}{mole}\right)\times M_{NaOH}\left(\frac{g}{mole}\right) + 0.2\left(\frac{mole}{mole}\right)\times M_{NaI}\left(\frac{g}{mole}\right)} \qquad (2.23)$$

where N is the total number of moles, M_{NaOH} =39.997 (g/mole), and M_{NaI} = 149.89 (g/mole) are the molar masses of NaOH and NaI respectively. Now that we have calculated the total number of moles of the salt mixture, the total mass of each component is simply the product of molar percentage, molar mass (M), and total molarity (N). In our case, the total mass of NaOH is 7.78 grams and the mass of NaI is 7.2 grams.

All active materials and salts are combined in a 2 cm diameter stainless steel crucible (figure 5-a). an insulating alumina (Al_2O_3) tube is used to prevent sodium from contacting the sides of the crucible. Galvanostatic cycling (constant current) is performed at a rate of 60 mA/cm^2.

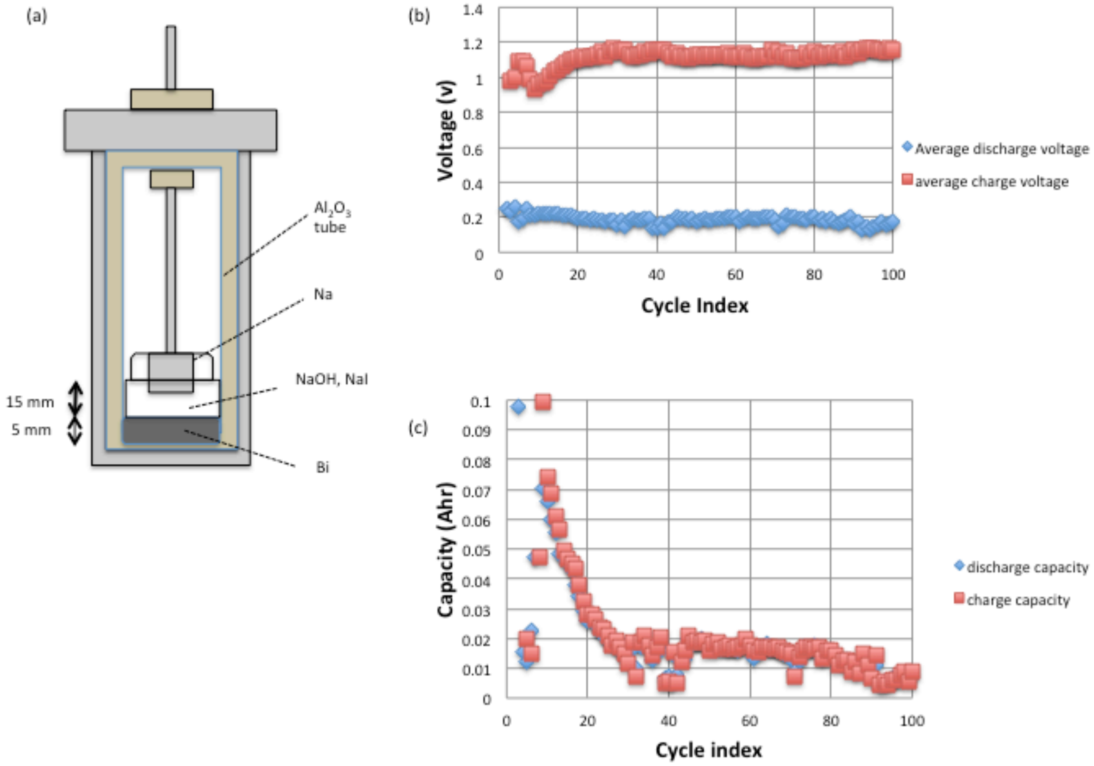

Figure 5 a) Na|NaOH,NaI|Bi battery operating at 280 °C with a rate of 60mA/cm^2. (b) Average discharge/charge voltage vs. cycle index. (c) Capacity vs. cycle index.

Figure 5-b shows the average charge (red) and discharge voltage during each cycle. This cell displayed low energy efficiency < 30%. In fact, this energy efficiency is similar to that reported by Spatocco et al. [19] This is a clear indication that the resulting low energy efficiency is not a result of Pb ions as hypothesized by Spatocco. On the other hand, the rapid capacity fade and high coulombic efficiency (97%) in figure 5-c supports the hypothesis that sodium undergoes self-passivation through side reactions with the electrolyte. Therefore, we propose the following reaction mechanism as the mechanism responsible for capacity fade

$$NaOH + 2Na \rightarrow NaH + Na_2O \tag{2.24}$$

In equation 2.24, Na anode reacts with NaOH to form sodium hydride (NaH) and sodium oxide (Na_2O). To investigate whether this reaction is spontaneous, that is, the associated change in free energy is negative, we used HSC thermodynamic database to calculate the change in free energy different operating temperatures. The results of the calculations are shown in table 3.

Table 3 Calculated changes in enthalpy (dH), entropy (dS) and free energy (dG) for reaction 2.24

T (°C)	dH (kcal)	dS (cal/K)	dG (kcal)
250	-13.96	-20.32	-3.33
275	-14.025	-20.43	-2.82
300	-15.59	-23.19	-2.30

Since the calculated free energy of the reaction in equation 2.22 is negative, we can safely state that the observed capacity fade in figure 5-c is due to the formation of Na_2O. Moreover, we can also state that the observed high over-potentials are likely due to the combined effect of ohmic resistance and slow diffusion of Na through Na_2O in the negative electrode.

2.4.1 The Ternary $NaNH_2$,NaOH,NaI system

In the previous section, we showed that NaOH reacts chemically with Na at moderate temperatures of 250-300°C. Even though this reaction was thought to form a passivating layer that reduces sodium solubility, the fact that we have observed rapid capacity fade suggests that this layer is not stable. In other words, the Na_2O layer is breaking and reforming during cycling. To overcome the problem of solubility and reactivity towards the electrolyte, we looked back at the work that was done to mitigate these problems in the Castner process for sodium electrolytic production.

The issue of sodium solubility and reactivity in molten salts is not unique to liquid metal batteries. Attempts to solve these issues date back to the late 1950's. As an example, Eidensohn filed for a patent on a sodium based fuel cell system with a ternary electrolyte composed of a eutectic NaOH, NaI, NaBr operating at 230^{o}C. [32] A similar approach is found in the 1963 patent of Watanabe et al. which describes electrolytic production of sodium from sodium-mercury amalgams by replacing NaBr in the previously described patent with sodium cyanide NaCN. [33] This allowed their electrochemical cell to operate at a temperature of 210^{o}C. In the patent of Heredy et al., $NaNH_2$ was used to replace NaCN, and this allowed the temperature to be reduced drastically to 130^{o}C. The ternary system of $NaNH_2$, NaOH, NaI reported by Heredey et al. has the one of the lowest reported melting point of 127^{o}C among inorganic alkali molten salt systems. Surprisingly, with the exception of our own published study of this system, [21] no prior studies have attempted to investigate the feasibility of using this electrolyte in electrochemical devices. Hence, our work in this section will focus on the feasibility of using the ternary eutectic mixture of 52% $NaNH_2$, 38% NaOH and 10% NaI as a low melting temperature electrolyte in liquid metal batteries.

Our first step in determining the feasibility of this electrolyte involves measuring its electrochemical window. A three-electrode setup shown in figure 6 is assembled inside an argon filled glove box. Tungsten wires are used for their corrosion resistance, and sodium is placed in β-Al_2O_3 tube to prevent any unknown reactions of sodium with the electrolyte from influencing our measurements. The temperature of the eutectic melt was initially set to 200^{o}C to allow homogenization before reducing the temperature to 180^{o}C.

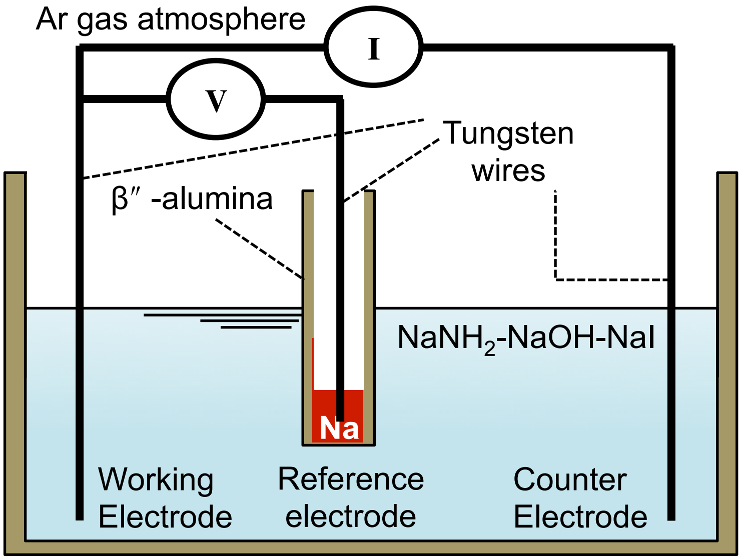

Figure 6 Three-electrode setup that employs tungsten wires as both working and counter electrodes. Sodium in β"-Al_2O_3 is used as a reference electrode and the temperature is 180°C.

Cyclic voltammetry is performed by changing the voltage of the working electrode (W wire) with respect to a fixed reference electrode (Na in β-Al_2O_3), and current is then measured between the counter and working electrodes. Figure 7 shows the result of a cyclic voltammogram obtained by sweeping the voltage of the working electrode at a rate of 100 mV/s. Since Na in β-Al_2O_3 is used as a reference electrode, we expect the peaks around (V= 0 vs. Na/Na^+) to be generated from reduction and dissolution of sodium on the surface of the working electrode. By simply looking at the magnitude of the measured electrical current during reduction (negative current) and oxidation (positive current), we can directly tell that the efficiency of sodium reduction/stripping is low. However, to get a quantitative measure, we integrated the total measured charge during reduction and oxidation and found the efficiency of sodium stripping to be less than 70%. This indicates that side reactions are occurring during negative voltage sweeps, perhaps an intermetallic of sodium and tungsten.

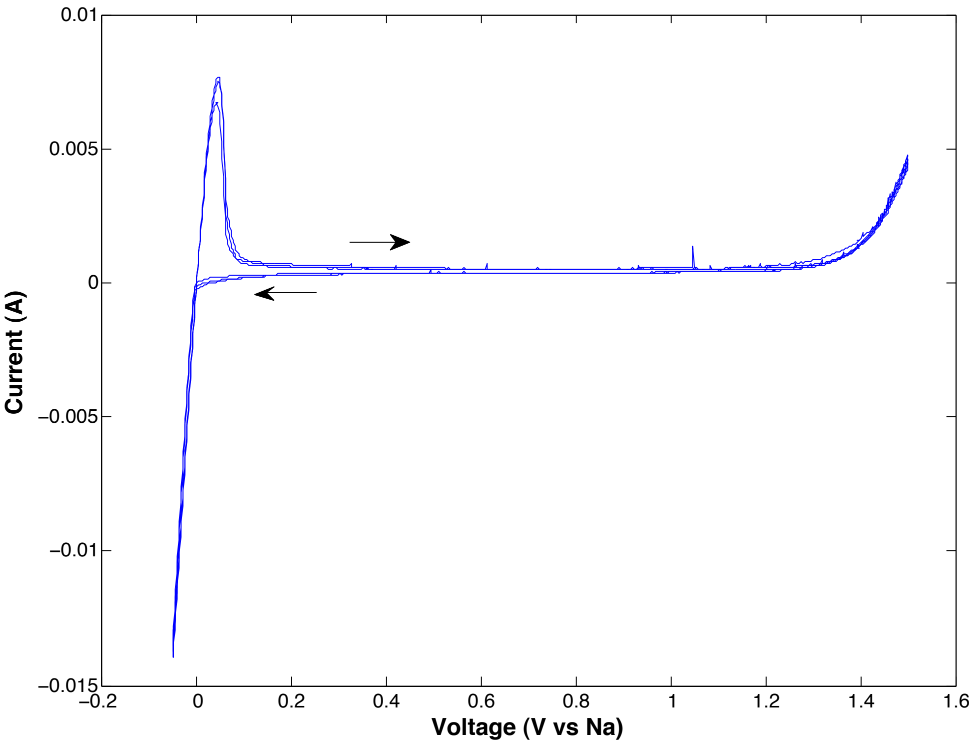

Figure 7 cyclic voltammogram of the ternary eutectic electrolyte at 100 mV/s and 180°C. Sodium in β-Al_2O_3 is used as a reference electrode. Work of the Author, as published in reference [21]

The measured electrochemical window of this ternary electrolyte is set by the strong oxidation signal (positive current) around 1.3 V vs. Na (figure 7). Possible limiting reactions along with their associated free energy and oxidation voltage are listed in table 4.

Table 4 Possible limiting oxidation reactions of the ternary eutectic melt at 180°C.

Reaction	Free energy of reaction, Δ G ($kJ.mol^{-1}$)	Reaction potential, E (V) vs. Na(*l*)
$NaOH \rightarrow Na + 1/2\ H_2O(g) + 1/4\ O_2(g)$	245	2.54
$NaNH_2 + NaOH \rightarrow 2Na + NH_3(g) + 1/2O_2(g)$	388	2.01
$NaNH_2 \rightarrow Na + 1/2N_2H_4(g)$	129	1.33

From table 4, it is clear that the limiting oxidation reaction is due to the oxidation of amide species NH_2 to hydrazine gas (N_2H_4) since it shows the lowest reaction potential, which also agrees the experimentally measured value of 1.3 V. To further confirm that the observed oxidation signal is due to the amide not hydroxide, we performed the same set of cyclic voltammetry experiments but with pure $NaNH_2$ at 250^{o}C. The observed behavior in figure 8 is similar to that of the eutectic melt but with few minor differences due to the elevated temperature.

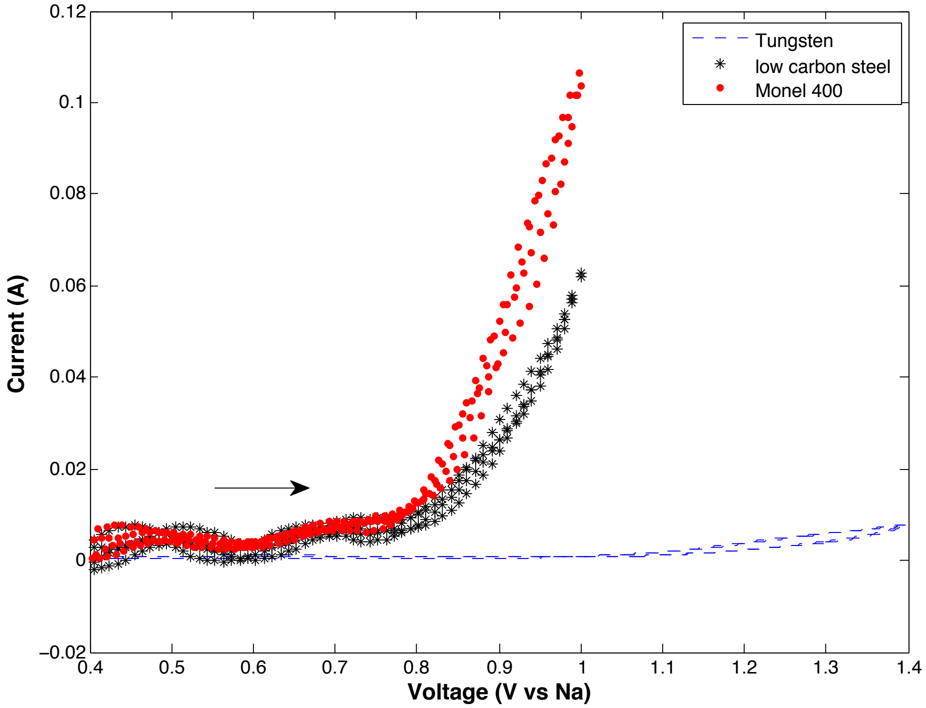

Figure 8 Anodic scan of pure $NaNH_2$ at a temperature of 250^{o}C and a scan rate of 100 mV/s. Sodium in β-Al_2O_3 is used as a reference electrode. Work of the Author, as published in reference [21]

Changing the working electrode material seemed to have a catalytic effect on the oxidation reaction. The observed oxidation signals are now shifted towards lower voltage values. This suggests that Tungsten is a good positive current collector material since it does not cause a rapid, and early gas evolution. Figure 9 shows a cyclic voltammogram of ternary molten salt at 180°C. The same catalytic effect is again observed in the ternary electrolyte when low carbon steel is used as a working electrode. However, now we observe an increase in sodium reduction/ deposition efficiency. In fact, the total efficiency increased from 70 to 90%. This means that low carbon steel represents a good candidate for negative current collectors. The overall reduction/stripping efficiency was found to depend on scan rate. Faster scan rates were found to yield lower efficiencies. This observation is similar to that made by Spatocco et al. in the study of the binary system of NaOH,NaI. This dependence on scan rate is attributed to a self-inhibiting reaction of deposited sodium with the electrolyte, which makes it more difficult to strip away sodium at higher scan rates.[19]

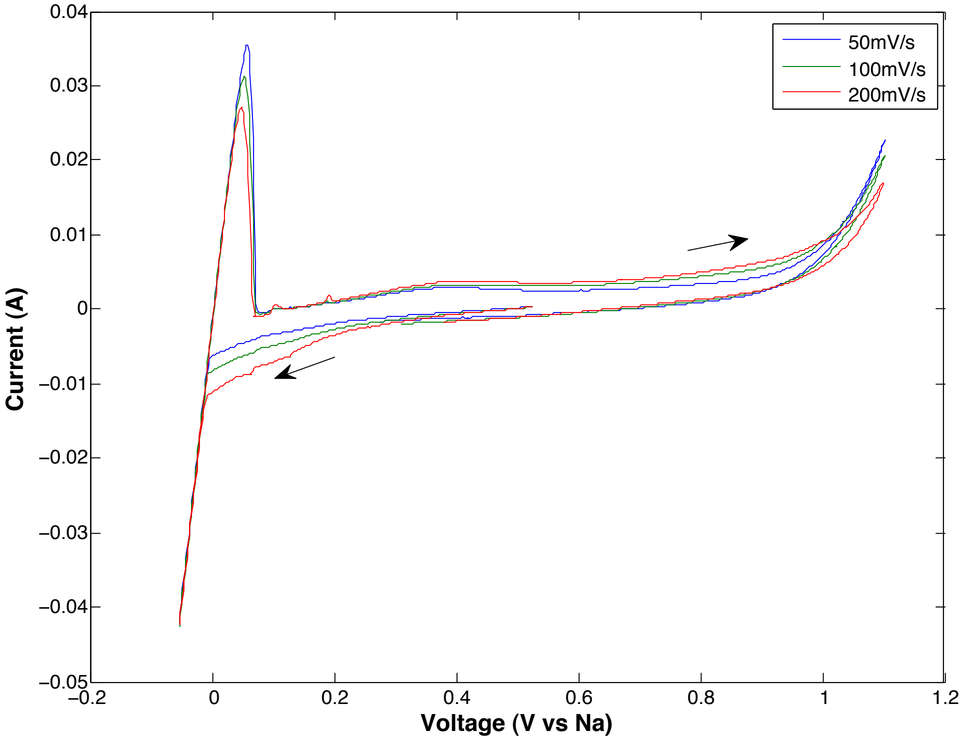

Figure 9 Cyclic voltammogram of ternary electrolyte at 180°C. Scanning rate is 100 mV/s. Low carbon steel is used as a working electrode and Sodium in β-Al_2O_3 is used as a reference electrode. Work of the Author, as published in reference [21]

The evolution of the flammable hydrazine gas (N_2H_4) presents a major safety concern, since it is known to be volatile enough to be used as a rocket fuel. Voltage of a full LMB employing this electrolyte should be limited to less than 1 V. This is of course still within the typical operating voltage of most liquid metal batteries.

Now that we have measured the electrochemical window, identified the limiting reactions, and named potential current collector materials, let us switch our attention to identifying the optimal operating conditions for a full LMB composed of Na|$NaNH_2$|PbBi. We chose to work with eutectic PbBi alloys for their low melting point <130^{o}C, and well-documented physical properties. [34] Of concern to us is the lack of ternary phase diagrams for the Na-Pb-Bi system. Hence, it is not possible to predict the phases that might form during cycling, or even the atomic percentages at which a phase change will occur. An uncontrolled growth of solid intermetallic can direct electrical contact between the two electrodes, which allows electrons to be exchanged locally through a highly exothermic reaction. Therefore, it is extremely important to investigate the optimal depth of discharge, that is, we are asking: Does Na in PbBi form dendritic intermetallic? And at what %at of Na does it start to occur? Furthermore, we ask: does the growth of intermetallic depend on the discharge/charge rate?

To answer these questions and to avoid the long process of trial and error, we developed a three electrode setup that uses several identical PbBi working electrodes, 20% Na in PbBi as a counter electrode, and Na in β-Al_2O_3 as a reference electrode. A schematic of the setup is shown in figure 10. By looking at the cross section of discharged electrodes, we were able to relate Na% in PbBi to intermetallic growth, and investigate the role of discharge rate. The set of experiments performed using this setup are summarized in table 5.

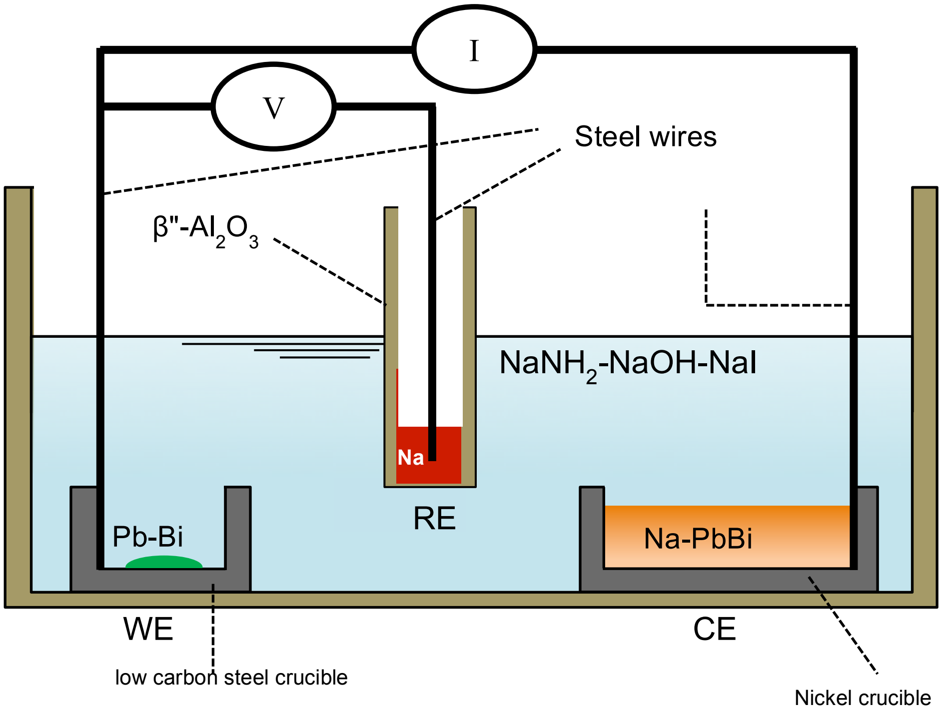

Figure 10 Three-electrode setup that employs eutectic PbBi alloys as the working electrodes, Na-PbBi as a counter electrode and sodium in β"-Al_2O_3 as a reference electrode. The temperature of the setup is 180°C. all electrodes are placed in a large Al_2O_3 crucible.

Table 5 Summary of experiments performed using the three-electrode setup shown in figure 10.

Fixed rate J=20 mA/cm^2 experiments	Fixed depth of discharge 5% Na in PbBi experiments
5% Na in PbBi	J=20 mA/cm^2
10% Na in PbBi	J=100 mA/cm^2
15% Na in PbBi	J=200 mA/cm^2

To investigate the effect of Na% in PbBi, three identical working electrodes were discharged to 5, 10, and 15% Na In PbBi. The electrode-electrolyte interface was imaged using a scanning electron microscope (SEM). The resulting images are shown in figure 11.

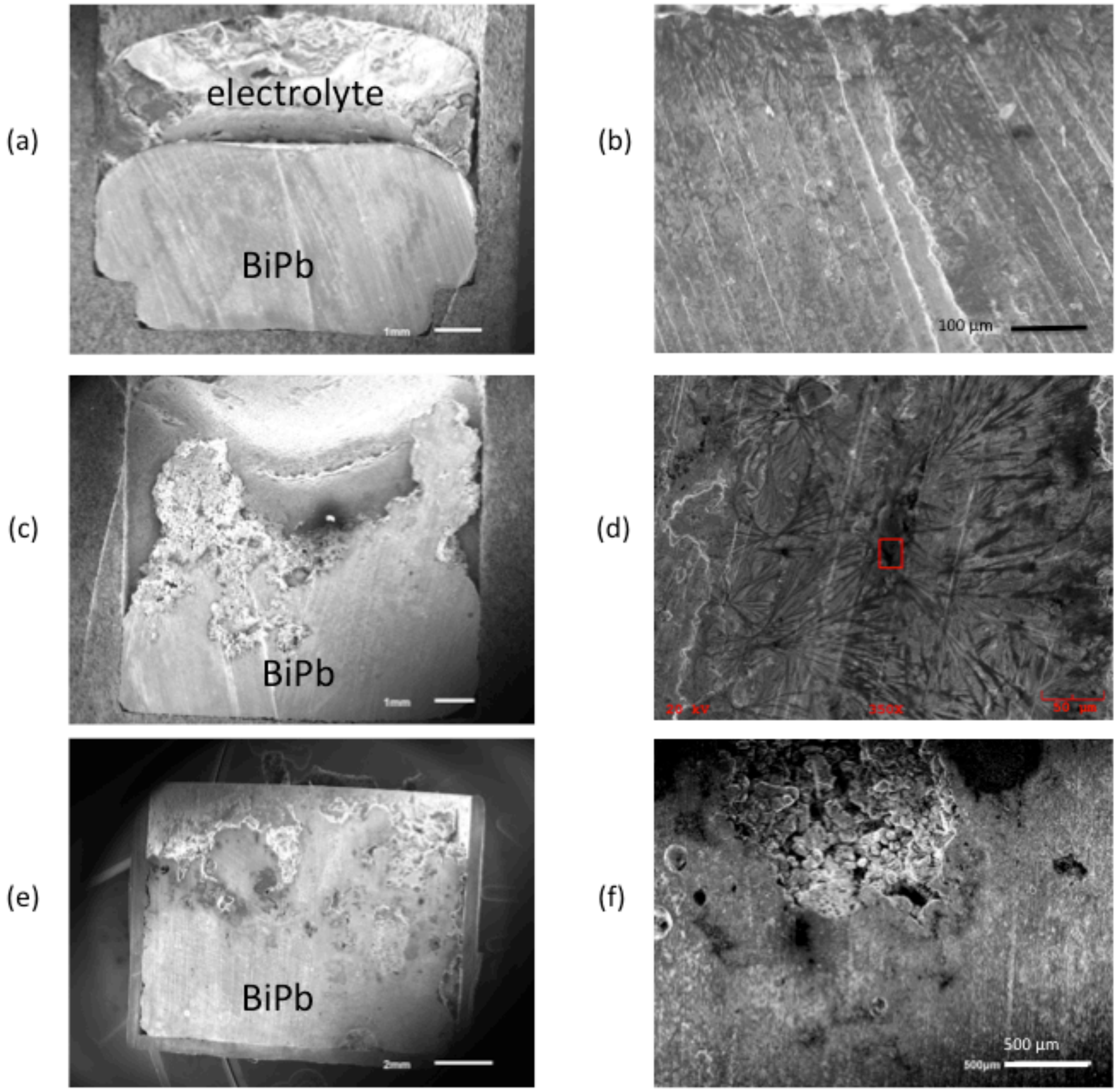

Figure 11 SEM images of PbBi working electrodes discharged at 180^{o}C to depths of (a) 5, 10 and 15%Na (a,c, and e respectively). (b),(d)and(f) are magnified images of (a,c, and e) respectively. Images taken at 20 keV using secondary electron imaging.

From figure 11, it is clear that drastic volume changes occur when the percentage of Na in PbBi is increased from 5 to 15%. Furthermore, we observed dendritic growth of intermetallic even when the depth of discharge is kept at less than 10%. It is also interesting to note that nucleation of intermetallic occurs homogeneously at the electrode/electrolyte interface, and growth occurs towards the bottom of the PbBi electrode. However, at higher percentage of Na, the intermetallic form granular particles that floats on the surface of the PbBi. The observation is similar to previous results by Kim et al. with the Ca-Bi system. [22] Kim et al showed that large particles of $Ca_{11}Bi_{10}$ formed on top of fully discharged Bi electrodes. Similar to the observation of Kim et al, the result obtained here are ex-situ and do not necessarily reflect the exact conditions that occur at higher temperatures. Yet, they can give insights to how the kinetics of our Na|BiPb battery might be affected by the growth of intermetallic. To determine whether Bi or Pb preferentially bind with Na, we took energy dispersive x-ray spectroscopy scans on the intermetallic particle in figure 11-d. The resulting spectrum is shown in figure 12.

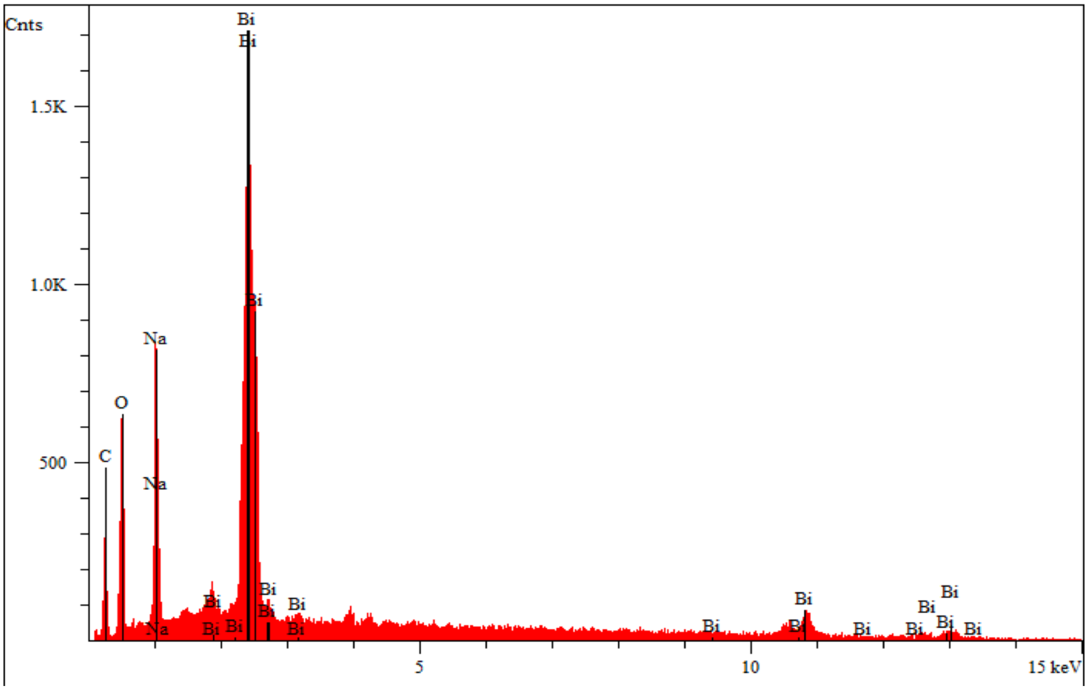

Figure 12 Energy dispersive x-ray spectrum on intermetallic shown in figure 10-d. The spectrum shows no detectable Pb signal within the scanned region. Horizontal axis represent energy of emitted x-rays and vertical axis represents photon counts.

The obtained spectrum in figure 12 shows no detectable signal from Pb atoms. The carbon signal is attributed to hydrocarbon contamination due to the exposure of the sample to air, while the oxygen signal is attributed to the (NaOH) particles in the salt. The lack of Pb suggests that Na binds preferentially with Bi to form NaBi intermetallic. This is consistent with the fact that the reaction potential associated NaBi is higher than that of NaPb. [4]

To test the effect of discharge rate on intermetallic growth, following the experiments outlined in table 5, we discharged identical working electrodes to 5% Na in PbBi at rates of 20, 100, and 200 mA/cm^2. The resulting electrode/electrolyte interfaces are then imaged using the SEM (figure 13).

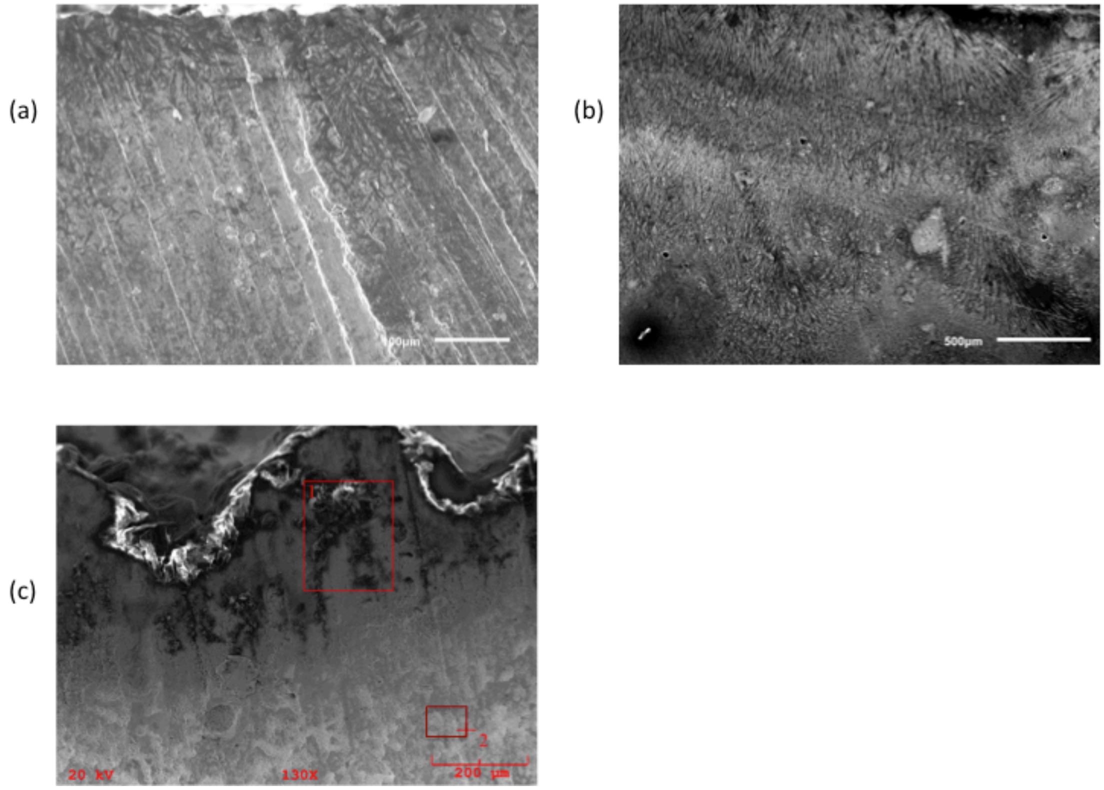

Figure 13 Dendritic growth of intermetallic on the electrode/electrolyte interface at a rate of (a) 20mA/cm^2, (b) 100 mA/cm^2 and (c) 200 mA/cm^2. Red squares in (c) indicate regions where x-ray spectra were taken.

Clearly, dendritic growth becomes more severe as the rate of discharge increases. At the point where a rate of 200 mA/cm^2 is used, the interface becomes covered with a cloud of intermetallic particles. This is likely due to the rapid depletion of Bi near the interface, the slow diffusion of Na$^+$ in the Na-Bi intermetallic, and the impedance of Na$^+$ transport by the less active Pb. To further confirm that the observed intermetallic is the result of preferential alloying of Na and Bi, we took two energy dispersive x-ray spectra of two regions marked on the image shown in figure 13-c. The resulting spectrum in figure 14-a again shows a lack of Pb signals near the interface where the intermetallic cloud has formed. Moreover, the second spectrum in figure 14-b shows a drastic increase in Pb signals as we move away from the interface. This further supports our hypothesis that Na preferentially alloys with Bi and is also consistent with the fact that their free energy is lower than that of Na-Pb.

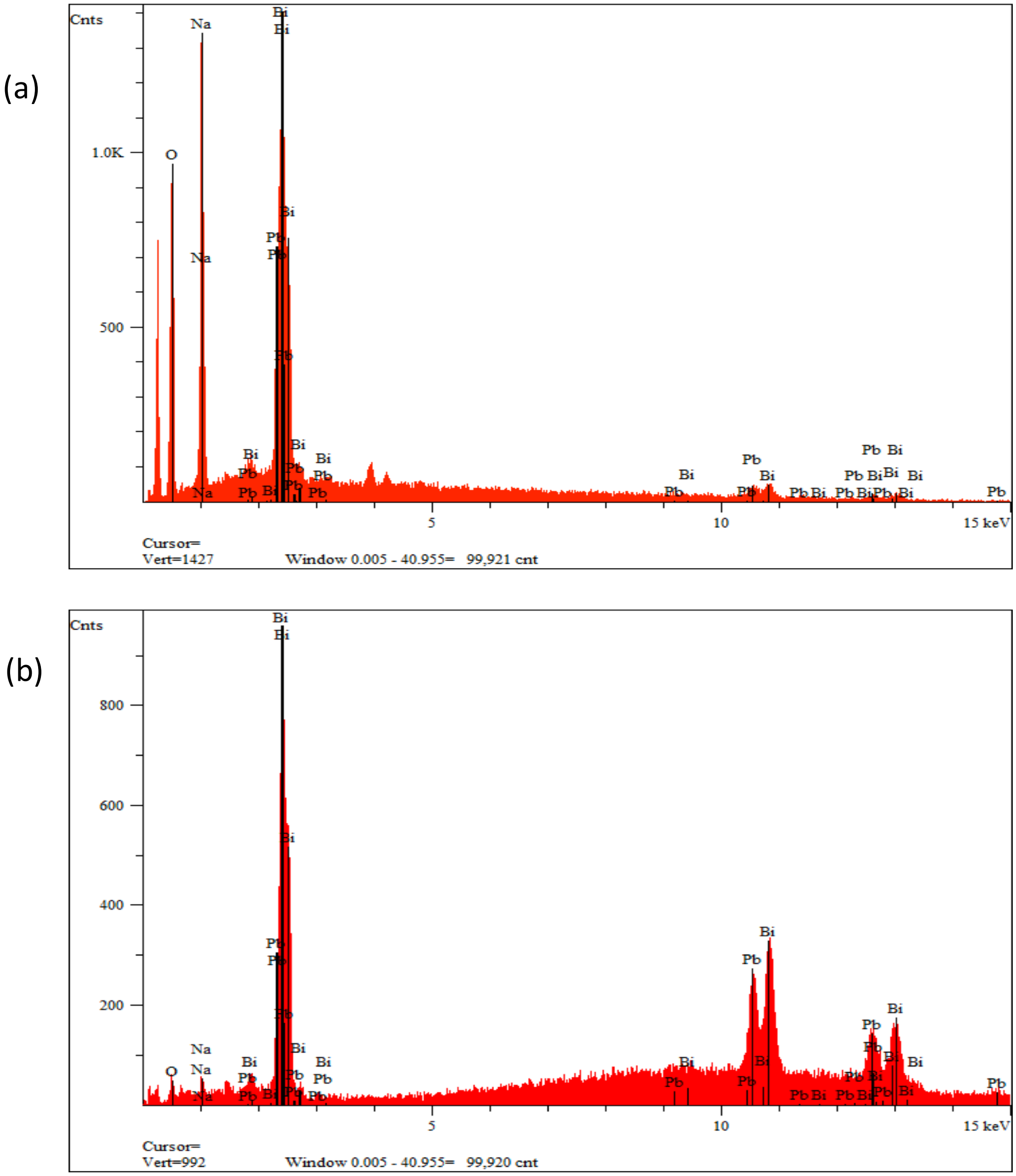

Figure 14 Energy dispersive x-ray spectra of figure 13-c. Signals are collected from (a) near the interface, (b) away from the interface.

So far we have measured electrochemical window of the ternary electrolyte, identified the safe voltage limits, and determined operating conditions that reduce the risk of volume expansion and electrical short. With all of this taken into consideration, we have built and tested the first low temperature, inorganic, and all-liquid sodium based liquid metal battery composed of Na|$NaNH_2$,NaOH,NaI,|Pb,Bi. An example of the resulting charge/discharge profile is shown in figure 15.

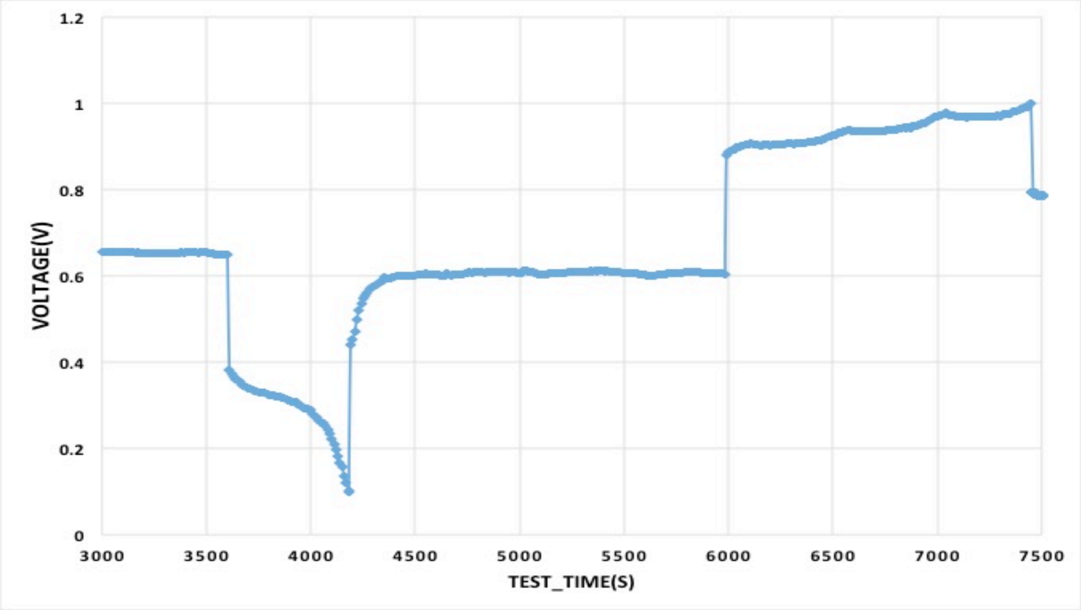

Figure 15 a discharge/charge profile of a full cell Na|$NaNH_2$,NaOH,NaI,|Pb,Bi cycling at a rate of 38 mA/cm^2.

The cell in figure 15 is assembled with a thick layer of molten salt (approximately 15 mm thick). Hence, we observed a high voltage drop due to ohmic losses in the electrolyte when the cell was cycled at 38 mA/cm^2. Even when the charge cut-off voltage was limited to <1 V, long term cycling has not shown promising results. Moreover, post discharge cells displayed severe side reactions between the negative electrode (Na) and electrolyte. This is deduced from the visual observation of black dispersed powder in the electrolyte and the anode (see figure 16).

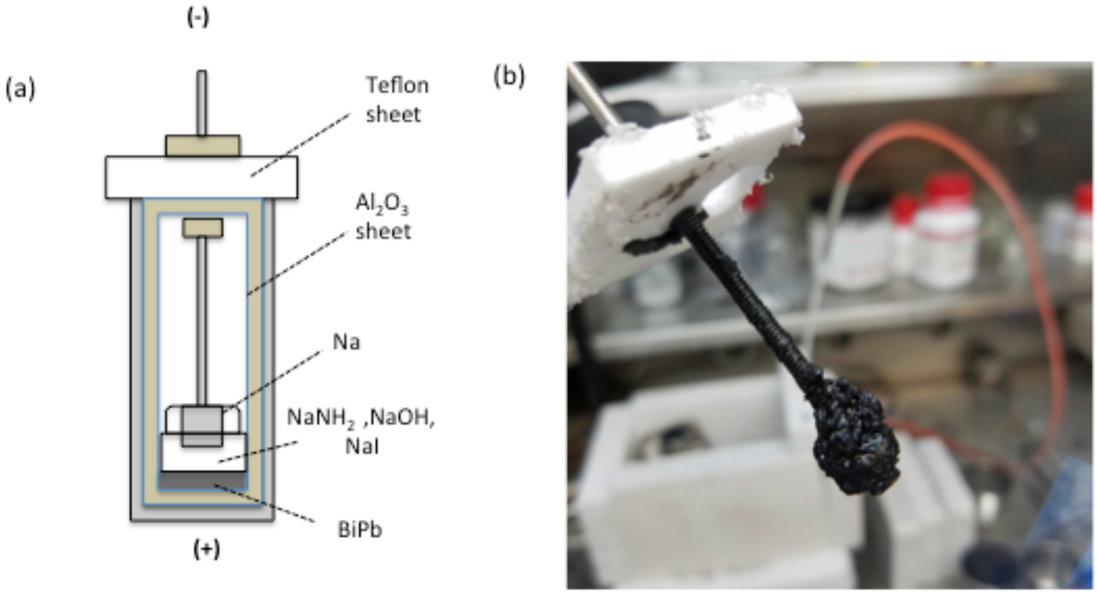

Figure 16 (a) Sketch of Na based LMBs assembled in Ar glove box at 180^{o}C. (b) Post cycling Na anode covered with black powder.

To the best of our knowledge, there have been no reported peer reviewed studies on the reactivity of Na towards molten $NaNH_2$. However, back in the early 1980's, a patent by Breda et al. [35] described a potential reaction of Na with $NaNH_2$ as

$$Na + NaNH_2 \rightarrow 2NaH + N_2 \qquad (2.25)$$

To test this hypothesis, we calculated the corresponding change in the Gibbs free energy in table 6.

Table 6 Calculated changes in enthalpy (dH), entropy (dS) and free energy (dG) for reaction 2.24.

T (^{o}C)	dH (kcal)	dS (cal/K)	dG (kcal)
150	1.97	9.51	-2.05
200	2.05	9.69	-2.53
250	2.19	9.98	-3.02

The fact that there's a negative change in the free energy indicates that the reaction described by equation 2.25 is indeed spontaneous. Increasing the temperature leads to an increase in the overall change in free energy (dG). Therefore, we attribute the poor long term cycling capabilities of the Na|$NaNH_2$,NaOH,NaI,|Pb,Bi cell to the irreversible reaction of Na with $NaNH_2$ as described by equation 2.25. Strategies to reduce Na reactivity are also found in the patent of Breda et al. [35]. The inventors suggest adding 2 to 20% by weight of NaH to the slurry electrolyte mixture in order to push the equilibrium of reaction 2.25 to the left.

2.5 Summary

In this chapter we performed extensive electrochemical studies of intermediate to low temperature liquid metal batteries. First, we showed that the gas forming reaction of Na molten NaOH is responsible for the rapid capacity decay in intermediate temperature NaOH,NaI binary systems. A full cell displayed high coulombic efficiency in excess of 90%, but the overall capacity decayed over 100 cycles. In addition, the round-trip energy efficiency was 30%.

We also studied the feasibility of the ternary mixture of 52% $NaNH_2$, 38% NaOH and 10% NaI as a low temperature inorganic molten salt electrolyte for low temperature liquid metal batteries. Using a three-electrode setup, a 1.3 V vs. Na electrochemical window was measured. The limiting reaction was determined to be the oxidation of $NaNH_2$ to form hydrazine gas N_2H_4. Using a second three-electrode setup, we identified the optimal operating conditions: (1) depth of discharge should be kept to 5% in PbBi, (2) operating current density should be less than 100 mA/cm^2. Long term cycling of full low temperature LMBs is a topic that needs further investigation. Finally, we have shown that

Na reacts with $NaNH_2$ to form NaH and N_2. Future work might focus on adding NaH to the electrolyte mixture, and perhaps replace NaOH with NaCl, or NaBr.

“The efforts of a child trying to dam a small stream flowing in the street, and his surprise at the strange way water works its way out, has its analog in our attempts over the years to understand the flow of fluids. We have tried to dam the water by getting the laws and equations, but the water has broken through the dam and escaped our attempts to understand it.”

Richard Feynman (1964)

Chapter 3: Fluid Dynamics of Liquid Metal Batteries

The scope of chapter three covers fundamental aspects related to the physics of momentum and mass transfer in electrically conductive fluids, a field of study called *magnetohydrodynamics,* commonly abbreviated as MHD. In short, work in this chapter focuses on forces driving fluid motion in liquid metal electrodes and batteries. First, a brief introduction of the role MHD in liquid metal batteries is presented. The second part will introduce governing equations and relevant dimensionless quantities. The final section will present experimental work on in-situ measurements of fluid flow in liquid metal electrodes.

3.1 MHD of liquid metal batteries

The unique all liquid design allows liquid metal batteries (LMB) to operate at unprecedented discharge/charge rates with negligible charge transfer over-potentials. When the battery is operated at low/moderate current densities, ohmic (IR) drop becomes the dominant form of voltage losses. However, when the battery is operated at high current densities, mass transport (concentration polarization) becomes the dominant loss mechanism. As an example, the fundamental study of electrochemical cycling in calcium antimony batteries have shown that 59% of voltage drop was attributed to mass transport. Similar studies by Newhouse et al. suggest that transport related losses in the positive electrode are expected to be higher than those that arise from polarization in the electrolyte.[36] For this reason, our focus in this chapter will be on flow in the positive electrode.

Early work on fluid dynamics of liquid metal batteries has focused on the narrow topic of Tayler Instability. [37–40] The Tayler instability is an MHD phenomenon that occurs when the applied current density exceeds a critical value. Beyond that critical value, surface deformation starts to appear. Work on Tayler instability has so far focused on numerical simulations of single electrodes. There is a consensus of results among different articles about geometrical limitation of LMBs due to the Tayler instability. However, it is important to note that the critical current at which Tayler instability occurs depends on the geometrical aspect ratio of height/diameter. The taller the battery is, the more susceptible it is to the Tayler instability. However, basic knowledge of electrochemistry suggests that electrochemical cells should maximize their surface area to facilitate more reactions, not their height. As an example, a modern aluminum reduction cell can have an area of 10m x 4m, yet its depth is only a few centimeters.[41] Therefore, It is highly unlikely that Tayler instability would ever be a real danger, even in larger cells.

Another MHD instability that has more practical implications is the sloshing or metal pad instability. This instability occurs when a vertical stray magnetic field interacts with the current passing through the cell. Minimal deformations in electrolyte layer can lead to drastic variations in the path of electrical current and consequently to the nature of the applied electromagnetic forces. Such instability is known to occur in large aluminum reduction cells. The mathematical description of this phenomenon uses a rigid metal pad on a pendulum to understand the physics of the instability (hence the name metal pad). [41] Later, Zikanov applied Davdison's approach to a three-layer liquid metal battery cell. [42]

Another well-studied instability is the thermal convection instability, and when the geometry involves heating from the bottom, the instability is referred to as Rayleigh-Bénard. Considering that liquid metal batteries are typically heated from below, temperature gradients are expected to arise through the depth of the fluid. The hot less dense fluid plume rises to the surface, while colder more dense plumes sink. Such instability has been shown to occur even in small laboratory scale models of LMBs. [43–45] Understanding how thermal convection is influenced by a LMB's operating conditions presents important engineering and design implications. Hence, it will be discussed in further details in the following sections. Another similar instability, which is still unexplored, is compositional convection. Just like thermal convection, compositional convection is triggered by spatial variations in chemical concentration, which in turn give rise to density variation.

Thermal Marangoni convection is yet another instability that is caused by spatial variations in surface tension of the fluid. Regions of high surface tension would pull on those with lower surface tension resulting in fluid flow. A flow in the bulk of the fluid is then induced through viscous coupling. Such instability was investigated in the numerical simulations of Thomas et al. [46] Marangoni flow generates flow with small velocity magnitudes that are not likely to affect the overall mass transport. However, it has been shown to interact and alter the structure of thermal convection rolls. It is important to note that surface tension variation can also be cause by local variations in chemical composition. Just like compositional convection, this area remains unexplored and deserves further investigation in the future. [46,47]

Another mechanism that can drive flow in liquid metal batteries is electro-vortex flow. During battery operation, an applied current density **J** produces a magnetic field **B**. The cross product between them gives a Lorentz force **F**. An illustration of electro-vortex flow is shown in figure 17.

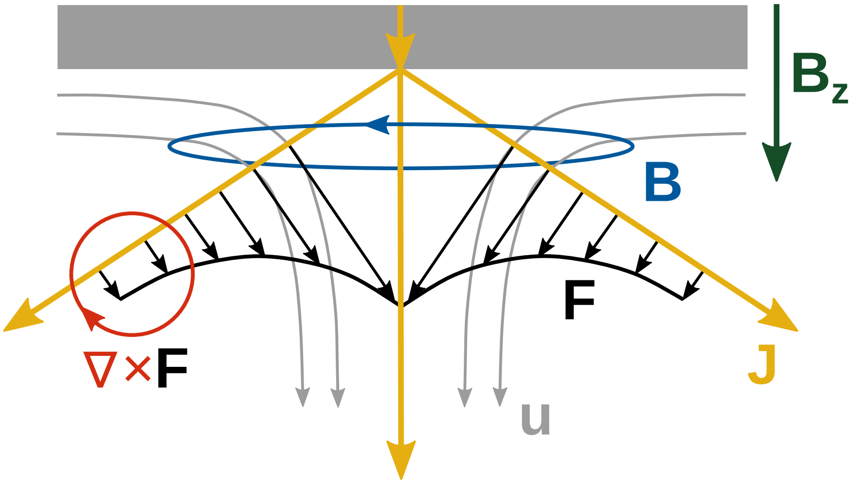

Figure 17 An illustration of electro-vortex flow velcotity **u** produced by electromagnetic force **F**. Figure adapted from [43]

It is important to note that if the force is conservative, that is its curl ($\nabla\times\boldsymbol{F}$) vanishes to zero, then it will not be able to drive any flow. The force **F** becomes conservative when the current passing in the battery is purely axial, and the induced magnetic field is purely azimuthal. In a typical LMB, the negative electrode material is discharged from a foam current collector that is smaller in diameter than the positive electrode. Hence, the resulting electromagnetic force is non-conservative, and electro-vortex flow is expected to play a role. The extent by which the electromagnetic force can influence the flow is a subject that we will discuss in more detail in the following sections of this chapter.

3.2 Governing Equations

Since previous experimental work has already shown that transport related losses are expected to be higher in the positive electrode, our experiments in this chapter will focus on fluid flow in the positive electrode. Our work is not concerned with dynamical instabilities that may or may not be relevant to liquid metal electrodes, such as the Tayler instability; instead, our focus is on fluid phenomena that are already happening inside each electrode. Before we embark on listing all the relevant equations, let us first establish a physical intuition of fluid flow in liquid metal electrodes.

A typical battery setup requires heating a crucible from the bottom. This will generate a temperature gradient along the depth of the electrode, and with the use of less than ideal thermal insulation from the sides, we expect the central region to be slightly hotter than the sides. Therefore, gravity will pull the more dense fluid plumes near the edges towards the bottom. Conservation of mass requires an inward flow near the bottom the crucible. When looking at the flow from a cross section, the flow will appear as two counter-rotating vortices that rise near the center and sink near the edges. Intuitively, we should expect the resulting flow speed to depend on the imposed temperature gradient, the depth of the fluid layer, as well as the properties of the molten metal (thermal conductivity, expansion, etc).

Another force that can initiate flow results from the interaction of electrical current passing through the electrode with its own magnetic field. A simple right hand rule will show that the interaction of an axial current with its azimuthal magnetic field will generate a force that points towards the central axis. As the current density and its magnetic field are more concentrated near the top of the electrode, the resulting force is stronger near the top of the electrode. Therefore, if electromagnetic forces drive the flow, then we expect a flow that will sink near the central axis and rise near the edges. Since that this flow is expected to act in the opposite to that generated by thermal convection, some natural questions to ask would be: will they compete? Which one will dominate?

To answer these questions let us imagine two separate systems, one in which the flow is driven by buoyant forces, and another that is driven by electromagnetic forces. Following an approach similar to that of Davidson et al. we will write the governing equations for the two systems separately. [41]

3.2.1 Thermal Convection: The Rayleigh- Bénard Instability

During the early 1900's a French physicist named Henri Bénard noticed the formation of regular flow patterns of graphite powder in molten paraffin wax, which he described as "tourbillons cellulaires" meaning cellular vortices.[48] At first, the goal of Bénard's experiments was to create solid dielectrics for coherers (an early form radio signal receivers). In 1901 Bénard defended his PhD dissertation on thermally driven convective flows. More than a decade later, Lord John William Strut, 3rd Baron Rayleigh, derived a rigorous mathematical description of the convective motion of fluids heated from below. [49] Rayleigh used a dimensionless ratio to describe the onset of convective motion,

$$Ra = \frac{g\,\beta\,\Delta T\,L^3}{\nu\alpha} \tag{3.1}$$

where β is the coefficient of thermal expansion, g is the gravitational acceleration, ΔT is the temperature difference, L is the thickness of the electrode, ν is the kinematic viscosity and α is the thermal diffusivity. The dimensionless number is named after Rayleigh and it describes the ratio of viscous to buoyant forces.

Here we shall not attempt to derive the equations of the Rayleigh- Bénard instability, as this is a long and tedious process that involves a 6th order differential equation. For a full derivation of the problem see Kundu et al. [49] However, we are interested in deriving a simple expression for the velocity of the flow from Navier-Stokes equation. Before we do that, let us introduce the ***Boussinesq approximation***. In simple words, the Bousssinesq approximation assumes that density variation is negligible and that the flow may still be treated as incompressible. The density terms ρ is described in terms of a reference density ρ_o and temperature T_o as $\rho = \rho_o[1 - \beta(T(z) - T_o)]$. The variables in the momentum equations are assumed to be the results of a stable background and an added perturbation such as

$$\tilde{\mathbf{u}} = 0 + \mathbf{u}, \quad \tilde{\mathrm{T}} = \mathrm{T(z)} + \Delta\mathrm{T}, \quad \tilde{\mathrm{p}} = \mathrm{p_o} + \mathrm{p} \qquad (3.2)$$

where $\boldsymbol{u}$ is the velocity vector, p is the pressure, and ΔT is the temperature difference between the top and bottom surfaces. The full Navier-Stokes equation is

$$\frac{\partial \tilde{\mathbf{u}}}{\partial \mathrm{t}} + (\tilde{\mathbf{u}} \cdot \nabla)\tilde{\mathbf{u}} = \nu \nabla^2 \tilde{\mathbf{u}} - \frac{1}{\rho \mathrm{o}} \nabla \tilde{\mathrm{p}} - \mathrm{g}[1 - \beta(\tilde{\mathrm{T}} - \mathrm{To})]\,\hat{\mathbf{z}} \qquad (3.3)$$

The case of a stable fluid layer, when no flow is observed ($\tilde{\boldsymbol{u}} = 0$), yields

$$0 = \frac{1}{\rho \mathrm{o}} \nabla \mathrm{p_o} - \mathrm{g}[1 - \beta(\mathrm{T(z)} - \mathrm{To})]\,\hat{\mathbf{z}} \qquad (3.4)$$

Subtracting equation (3.4) from (3.3) gives the full equation for the convective state,

$$\frac{\partial \mathbf{u}}{\partial \mathrm{t}} + (\mathbf{u} \cdot \nabla)\,\mathbf{u} = \nu \nabla^2 \mathbf{u} - \frac{1}{\rho} \nabla \mathrm{p} - \mathrm{g}\beta\Delta\mathrm{T}\,\hat{\mathbf{z}} \qquad (3.5)$$

To get an estimate of the velocity of a steady convective flow in the core (away from the boundaries), we follow the approach of Davidson et al. [41] by considering the vertical component ($\hat{\boldsymbol{z}}$) and equating the non-linear term in equation (3.5) with the buoyancy term we get

$$u_b \sim \sqrt{g\, \beta\, \boldsymbol{\Delta} T\, L} \qquad (3.6)$$

where u_b is the characteristic free fall velocity due to buoyant forces. In equation 3.6, we used the approximation $\nabla \sim 1/L$, where L is the depth of the fluid layer.

Going back to Navier-Stokes (3.6), we can assume a linearized sinusoidal solution of the form $u(\mathbf{x},t) \sim u(\mathbf{x}) \exp\{i\sigma t\}$, where σ is the complex growth rate, $i = \sqrt{-1}$, and t is time. After dropping quadratic terms, applying boundary conditions, and if one has the will power to go through a 6th order differential equation, then we would be able to get the point beyond which the complex growth rate σ becomes positive ($\sigma > 0$). Turns out, for an infinite system with a lower solid boundary (i.e. no slip) and a free upper surface, the onset of instability occurs at a critical Rayleigh number of Ra=1100.

3.2.2 Electromagnetically Driven Flows

Since 1886 when the first Hall-Heroult cell was introduced, metallurgists have been passing currents in large electrochemical cells. However, it was not until the early 1900's when scientists began to question the role of electrical current on fluid motion. In 1907, Northrup was investigating the role of electrical current on fluid motion in mercury. Northrup and his colleagues observed a sudden contraction in the surface of the mercury as current is injected. He argued that contraction was due to the action of "magnetic force". In his original paper he argued that this contraction was due to the elastic action of what he called the magnetic force. This force he argued, encircle the conductive fluid and act like stretched rubber bands. Because of this rubber band action, Northrup and his colleague Hering named their observation the "pinch phenomenon" [50] As time went on, the term pinch phenomenon was replaced by electro-vortex flow. [51] Of course we know that both Northrup's pinch phenomenon and electro-vortex flow are nothing but fluid motion driven by the action of electromagnetic (Lorentz) forces.

Before we list the governing equations, it is important to mention that our work will focus on the influence of prescribed magnetic field on a velocity profile, but not the other way around. That is, we assume that the magnetic field **B** can influence the velocity **u** profile, but **u** cannot influence **B**. This assumption is called the low *magnetic Reynolds number* approximation. One might recall the definition of the Reynolds number (Re) as ratio of inertial over viscous forces. The magnetic Reynolds number, which we will denote as Re_m is the ratio of advection over diffusion of a magnetic field **B**,

$$Re_m = \frac{u\,l}{\lambda_m} \tag{3.7}$$

where λ_m is magnetic diffusivity. It is only when Re_m becomes exceedingly large that the influence of **u** on **B** becomes important. One example is the case of flow in Earth's core where typical length scales are extremely large. In such case the magnetic Reynolds number can be as large as $\mathrm{Re}_\mathrm{m} > 100$. [41] In our case, a typical LMB electrode will have a length scale of $l \sim 10^{-2}$ m and characteristic velocity of $u \sim 10^{-3}$ m/s and if we take $\lambda_m \sim 1$ m^2/s then $\mathrm{Re}_\mathrm{m} \sim 10^{-5}$.

For a fluid driven by electromagnetic forces alone, the full Navier-Stokes equation is

$$\frac{\partial \boldsymbol{u}}{\partial t} + (\boldsymbol{u} \cdot \nabla)\, \boldsymbol{u} = \nu\, \nabla^2 \boldsymbol{u} - \frac{1}{\rho} \nabla p + \frac{1}{\rho} \boldsymbol{J} \times \boldsymbol{B} \tag{3.8}$$

where $\boldsymbol{J}$ is the current density in units of ampere/m^2, and $\boldsymbol{B}$ is magnetic field in units of Tesla. The cross product of $\boldsymbol{J}$ and $\boldsymbol{B}$ gives the electromagnetic force per unit volume. Diving by density ρ gives the force per unit mass (acceleration).

We have already explained how this force will push on the fluid more strongly near the top causing the fluid to sink near the center. Conservation of mass causes the flow to recirculate, and in our electrode geometry this will lead to a symmetric poloidal motion in the cross-sectional plane. To understand the physics of this poloidal flow, Shercliff applied a self-similar solution to an infinite layer fluid domain with an infinitesimally small current source. [52] Sherclif's solution had inherent problems since it assumes an infinite and inviscid flow. One such problem is the lack of closed streamlines and a mechanism for energy dissipation. This suggests that the fluid can gain infinite kinetic energy. Nevertheless, many physicists and mathematicians at that time focused on the infinite domain, simply because of the discovery of Sherclif's analytical solution.

Before we estimate how the velocity scales with current, it's helpful to re-write equation 3.8 as

$$\frac{\partial \boldsymbol{u}}{\partial t} = \boldsymbol{u}\times\boldsymbol{\omega} + \nu\nabla^2 \boldsymbol{u} - \nabla[\frac{P}{\rho}+\frac{u^2}{2}] + \frac{1}{\rho}\boldsymbol{J}\times\boldsymbol{B} \tag{3.9}$$

where $\boldsymbol{\omega}$ is the vorticity ($\boldsymbol{\omega} = \boldsymbol{\nabla}\times\boldsymbol{u}$). To get to equation 3.9, we used the following vector identity

$$\boldsymbol{\nabla}(\mathbf{A}\cdot\mathbf{B}) = \mathbf{A}\times\boldsymbol{\nabla}\times\mathbf{B} + \mathbf{B}\times\boldsymbol{\nabla}\times\mathbf{A} + (\mathbf{A}\cdot\boldsymbol{\nabla})\mathbf{B} + (\mathbf{B}\cdot\boldsymbol{\nabla})\mathbf{A} \tag{3.10}$$

where $\mathbf{A}$ and $\mathbf{B}$ are simply replaced by our velocity vector $\boldsymbol{u}$. Now to get an estimate of our velocity, we shall follow Davidson's approach and integrate equation 3.9 around a closed streamline to get:

$$\frac{1}{\rho}\oint \boldsymbol{J}\times\boldsymbol{B}\cdot d\boldsymbol{l} = \upsilon\oint \nabla^2\boldsymbol{u}\cdot d\boldsymbol{l} \tag{3.11}$$

where $\boldsymbol{u}\times\boldsymbol{\omega}\cdot d\boldsymbol{l} = 0$, and the integration of the gradient of the Bernoulli term $\nabla\,[\frac{P}{\rho}+\frac{u^2}{2}]$ vanishes to zero. [41] Equation 3.11 represents a balance between the work done on the fluid by electromagnetic forces and viscous dissipation in the boundary layer. It is not possible to solve 3.11 for our electrode geometry. However, we can get an order of magnitude estimate by letting $\nabla \sim 1/\delta$, where δ is the thickness of the boundary layer. Using $\delta \sim \frac{R}{\sqrt{Re}}$, where R is the radius of our crucible and Re is the Reynolds number gives:

$$u \sim \sqrt{\frac{J\,B\,R}{\rho}} \tag{3.12}$$

It is important to note that different estimates can also be obtained by letting $\nabla \sim 1/l$. This will lead to a different scaling for our velocity! Does this mean that we have two different scaling laws? This mathematical paradox is explained in more detail in Davidson et al. [41] Similar scaling analysis can also be found in the work of Bojarevics et al. [51,53] Applying Ampere's law to equation 3.12 leads to the following velocity scaling

$$u \sim \frac{(\frac{\mu_o}{\rho})^{1/2} I}{2\,\pi\,R} \tag{3.13}$$

where I is the total current and μ_o is the permeability of free space.

3.2.3 Flows Driven by Electromagnetic and Buoyant Forces

In a flow in which both buoyant and electromagnetic forces are present, we expect the flow speed to be predicted by equation 3.6 when buoyancy dominates and predicted by equation 3.13 when electromagnetic forces dominate. We can moreover predict which of the two effects dominates by comparing the predicted flow speeds. Taking the ratio of the two equations gives the dimensionless parameter

$$A = \frac{I}{2\,\pi\,R}\sqrt{\frac{\mu_o}{\rho\,g\,\beta\,\Delta T\,L}} \tag{3.14}$$

Equation 3.14 is a newly derived dimensionless that represents the ratio of momentum gained by current injection to that gained by buoyant forces. [43] Other dimensionless ratios for flows in different geometries are also available in Flood and Davidson. [41,54]

3.3 Experimental Methods

The experimental methods described in this section are taken directly from our previously published work in the *Journal of Power Sources*. [43] Our test vessel is a cylindrical 304 stainless steel container with an inner diameter of 88 mm and an outer diameter of 100 mm. An 8 mm in diameter ultrasound probe fits in a Swagelok fitting, which is welded directly to the side of the container. The center of the probe is located at a distance of 6 mm from the bottom. The stainless steel cup sits on a larger aluminum block in order to allow uniform supply of heat and electrical current. The aluminum block has a 180x180 mm^2 surface area and a thickness of 30 mm, and is heated by two heating elements (McMaster Carr). Temperature is monitored via two k-type thermocouples (Omega). The thermocouples are connected to a 5V digital to analog converter (DAC), which is then controlled using LabView on an external laptop. A third thermocouple is connected to a proportional integral derivative controller (PID), which allows the temperature to be controlled using a mechanical relay. The entire setup is then placed in a fiberglass wrapped silica sheets. This allows the setup to maintain elevated temperatures for extended periods. A picture of the setup is shown in figure 18 below.

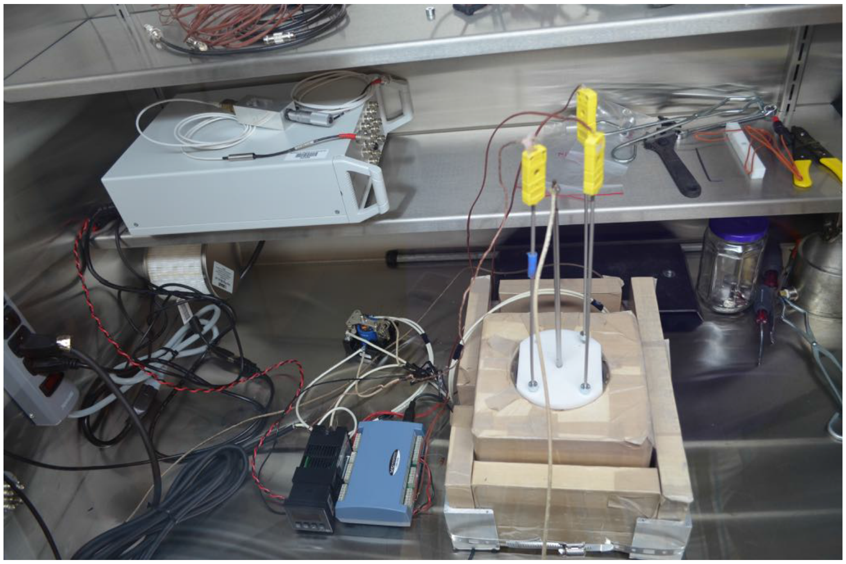

Figure 18 Experimental setup used for in-situ measurements of fluid flow in liquid metal electrodes.

Note that in the setup shown in figure 18, current is supplied to the aluminum plate from the side. As we shall show later in this chapter, this will have a strong effect on the overall flow structure. The setup was then modified to allow symmetric connection.

Our experiments in this chapter will focus on the eutectic alloy composed of 44.5% Pb and 55.5% Bi. The experiments are performed at a melt temperature of 160^{o}C in order to model flow in the cathode of the batteries described previously in chapter 1. Velocity is measured with an 8 MHz transducer connected to a DOP-3010 (Signal Processing). During operation, the ultrasound operates by sending a pulse and then switching off to listen for echo. Knowing the speed of sound in the PbBi melt (c=1780 m/s), the distance from which echo is produced is calculated from the time of flight (time delay) and the speed of sound. The speed of a moving particle is calculated from the Doppler shift in the echo. Negative velocities indicate objects moving toward the transducer, while positive values imply objects moving away from it. The exact mechanism by which echo is produced in high purity alloys is a topic that is still being investigated. However, for the purpose of our research, it suffices to say that metal inclusions and dissolved gas are responsible for producing echo in high purity metal and alloy melts.

For future researchers attempting to recreate or expand upon this work, it is important to avoid large thermal gradients between the ultrasound transducer and the molten metal. Such gradients will cause the molten metal to be super cooled. Moreover, the surface of the transducer will alloy dissolved oxides to nucleate and grow heterogeneously on the face of the probe. Maintaining the transducer at the same temperature of the melt before making any measurement can minimize this problem.

3.4 Results & Discussion

All ultrasound measurements in this chapter are done at a temperature range 160-180°C. Before each measurement, the flow was given sufficient time to reach a steady state (if there exists one). A thin layer of 700g of molten PbBi was melted in the stainless steel crucible. This gives a realistic electrode thickness of ~11 mm. Going back to our results in chapter 1, If we were to assemble a full cell with a 10% Na in PbBi as the full depth of discharge, and knowing that we have 3.38 moles of PbBi, then our model would resemble flow in a 9 Ahr Na|PbBi LMB.

Our initial experiments focused on the extreme case when current is discharged from a point-like current collector. Using a 4 mm diameter Ni plated Cu wire as a negative current collector resembled the case of high electromagnetic forces $|\boldsymbol{J}\times\boldsymbol{B}|$. Figure 19 shows an ultrasound measurement of flow in PbBi electrode driven by thermal convection alone (I=0A).

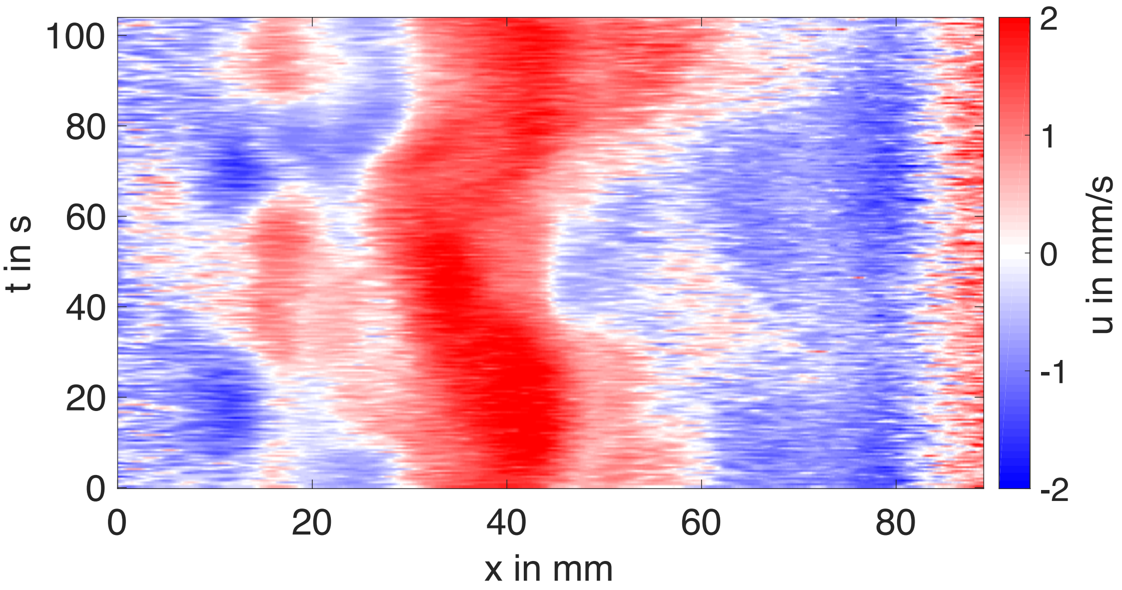

Figure 19 Radial velocity of a liquid metal electrode driven by thermal convection alone (I=0A). Work of the Author, as published in reference [43]

In figure 19, positive (red) values indicate flow away from the probe, and negative values (blue) indicate flow toward the probe. Distance from the probe is indicated on the horizontal axis, and the center of the plotted range corresponds to the center of the vessel. Time progresses up the vertical axis. Consistent with our description in section 3.2, the measured flow resembles two large counter-rotating vortices that are rising in the center and sinking near the edges. The flow in figure 19 shows some degree of time dependence. This is consistent with previous experimental measurements by Kelley and Sadoway. [45]

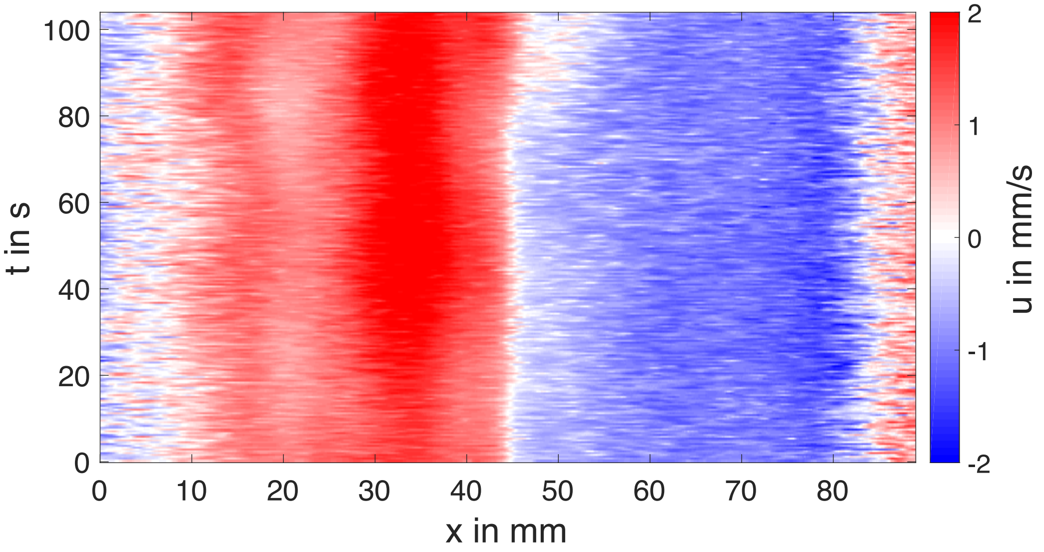

Figure 20 Radial velocity of a liquid metal electrode driven by thermal convection and an electrical current of I=2A or J = 32 mA/cm^2. Work of the Author, as published in reference [43]

In figure 20, a current of 2A (J=32 mA/cm^2) is introduced into the PbBi electrode. By comparison with figure 19, the flow shows more order. The flow is axisymmetric with respect to the central axis and is dominated by two convection rolls that are rising near the center and sinking near the edges. The increase in order might be explained by the alignment of convection rolls with the magnetic field lines. [55] This alignment results from the effect of magnetic damping that arise from the interaction of the induced current $\boldsymbol{J_o} = \boldsymbol{u}\times\boldsymbol{B}$, with the imposed magnetic field in the electrode. Since $\boldsymbol{u}\times\boldsymbol{B}=0$ for all velocity components that are parallel to the imposed field, magnetic damping is only limited to velocity components that are perpendicular to the imposed field. Hence, fluid plumes that are crossing the field lines will slow down and their kinetic energy is dissipated as heat. The fact that the overall flow speed did not increase upon introducing an additional forcing parameter agrees with our description in section 2.3. Both thermal convection and electro-vortex flows are competing. But, in this parameter regime, the value of our dimensionless parameter A << 1, hence we expect thermal convection to dominate. To make a prediction of the point beyond which electro-vortex flow becomes dominant, let us substitute the material properties of PbBi in the dimensionless quantity A (equation 3.14). Using $\nu=2.7\times10^{-7}$ m^2/s, $\beta=1.3\times10^{-4}$ K^{-1}, $\rho=9.8$ m/s^2, $\alpha=6\times10^{-6}$ m^2/s, and $\mu_o=4\pi\times10^{-7}$, the resulting value of A at different currents is shown in figure 21.

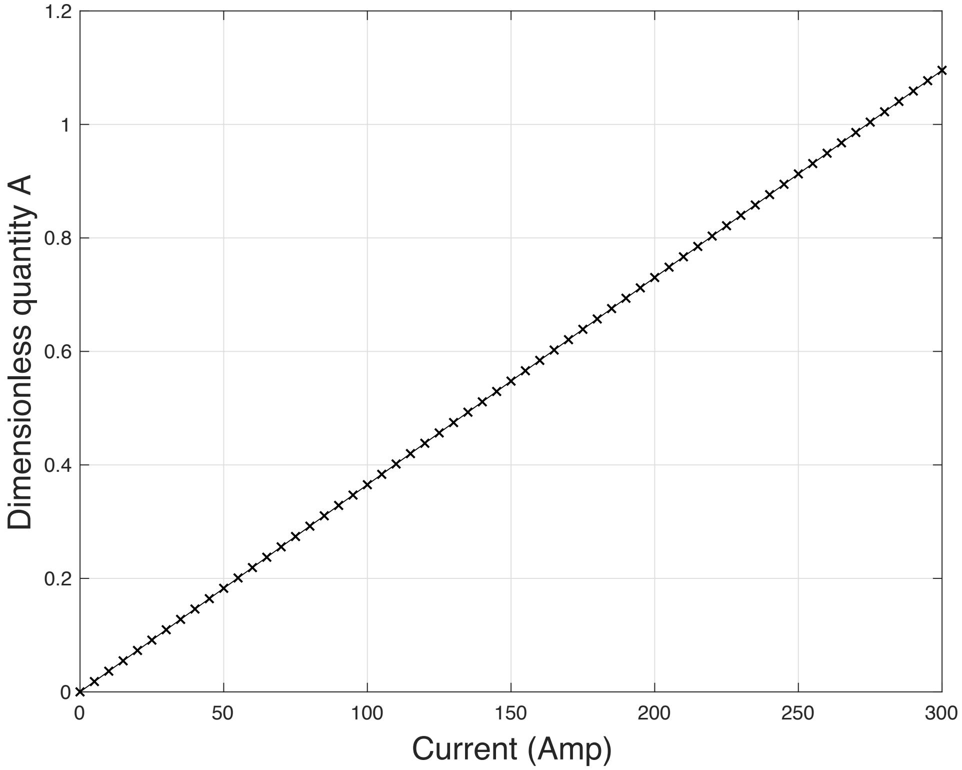

Figure 21 Current Vs. Dimensionless quantity A calculated using equation 3.14.

If our analysis are correct, then we would expect electro-vortex flow to dominate when the total current exceeds I > 250A. In our 88 cm diameter cell, this represents a current density higher than 4000 mA/cm^2. Such high current densities are not typically used in LMBs. Moreover, at such high current densities, it is likely internal (Joule) heating will become more important than electro-vortex flow. To learn more about internal heat convection and its effect on the flow, see our *Journal of Power Sources* article.[43]

Upon increasing the current to I=10 A (figure 22), we no longer observe this poloidal circulation in the plane of symmetry. Instead, a fast, swirling, tornado-like flow emerges.

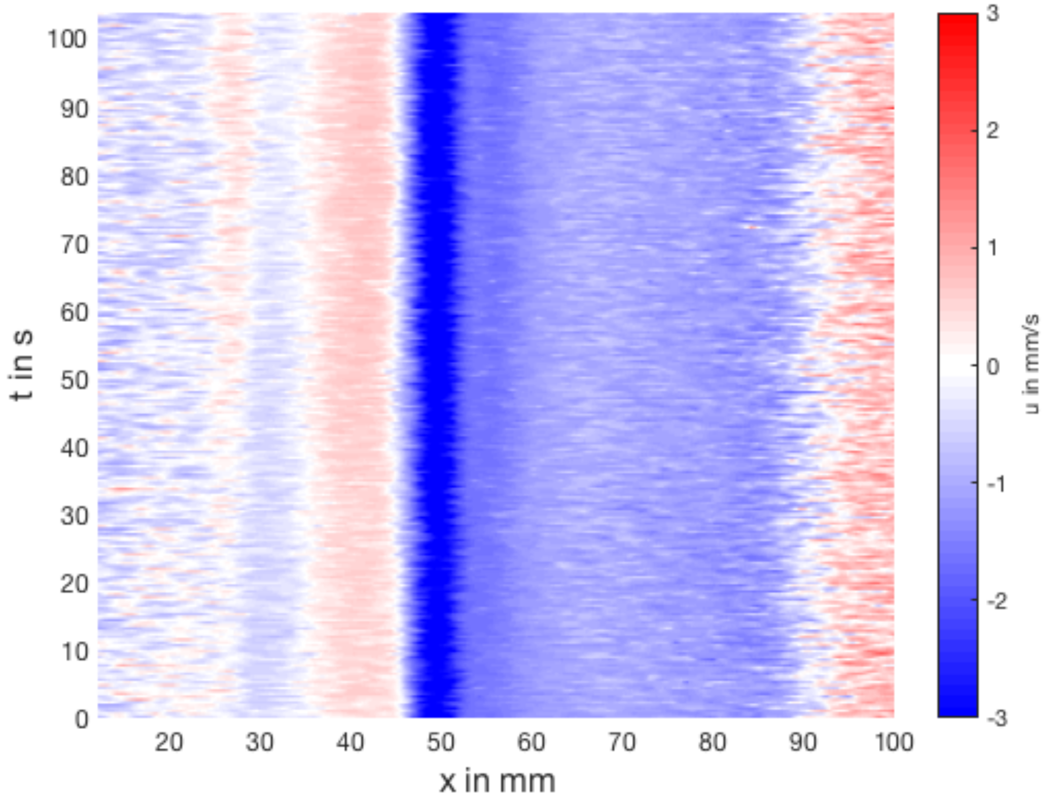

Figure 22 Radial velocity of a liquid metal electrode driven by thermal convection and an electrical current of I=10A or J = 164 mA/cm^2.

The narrow region in the center of figure 22 represents a fast flow moving in the direction of the ultrasound transducer. Since mass is conserved, the fast moving region in the center must resemble flow moving in and out of the ultrasound's volume of measurement. Hence, this region is interpreted as a swirling flow that is moving around a vertical axis a slight offset in the line of measurement of the ultrasound beam allows for the measurement of azimuthal flow.

The swirling flow remained steady for as long as current is supplied. The fact that both electromagnetic and buoyant forces inside the electrode are purely poliodal suggests that the force driving this azimuthal flow must come from an external perturbation. After a long process of elimination, we are left with two possible mechanisms by which this flow can arise. First, and most likely the dominant effect in this situation, is the interaction of the axial magnetic field component B_z from the side wire that supplies current to the aluminum plate with the radial current density component J_r. This will result in the emergence of an azimuthal force F_θ. Such force is able to transform the poliodal flow structure into a swirling azimuthal flow. Another similar mechanism is through the interaction of Earth's magnetic field with the radial current passing within the electrode. Both will have the same effect and perhaps can even be affecting the flow simultaneously in our case.

Outside of the central vortex in figure 22 we see a poliodal flow that is moving toward the center. To understand how this flow develops, we can make an analogy to stirring a cup of tea. In a time when tea bags were not common, stirring a cup of tea resulted in a poliodal motion of tea leaves and eventually their accumulation near the bottom center of the cup. So the question here is why do tea leaves accumulate at center as opposed to the edges? Here's what is happening: fluid elements that are spinning in a curved path experience a balance between centrifugal forces that wants to push the fluid outward and pressure gradients that wants to push the fluid inward. Because the fluid near the bottom is moving slower, the centrifugal force is not able to balance pressure gradients. Consequently, the fluid moves inward by pressure and recirculates upward. Note that this circulating flow is a byproduct of the primary swirling flow. Hence, it is given the name secondary flow. The mechanism by which this flow emerges is named after the Swedish oceanographer Vagan Walfrid Ekman, and is now called Ekman pumping.

So far our experiments have focused on the case when current is supplied from a side wire. We have not examined whether this swirling phenomenon will still occur when current is supplied to the electrode from symmetric wiring that mitigates the effect of axial fields. To do that, we replaced the side wire with a 1m long aluminum rod, which we mounted at the center of the bottom plate. Figure 23 shows the root mean square of flow velocity at different currents and different wiring topology.

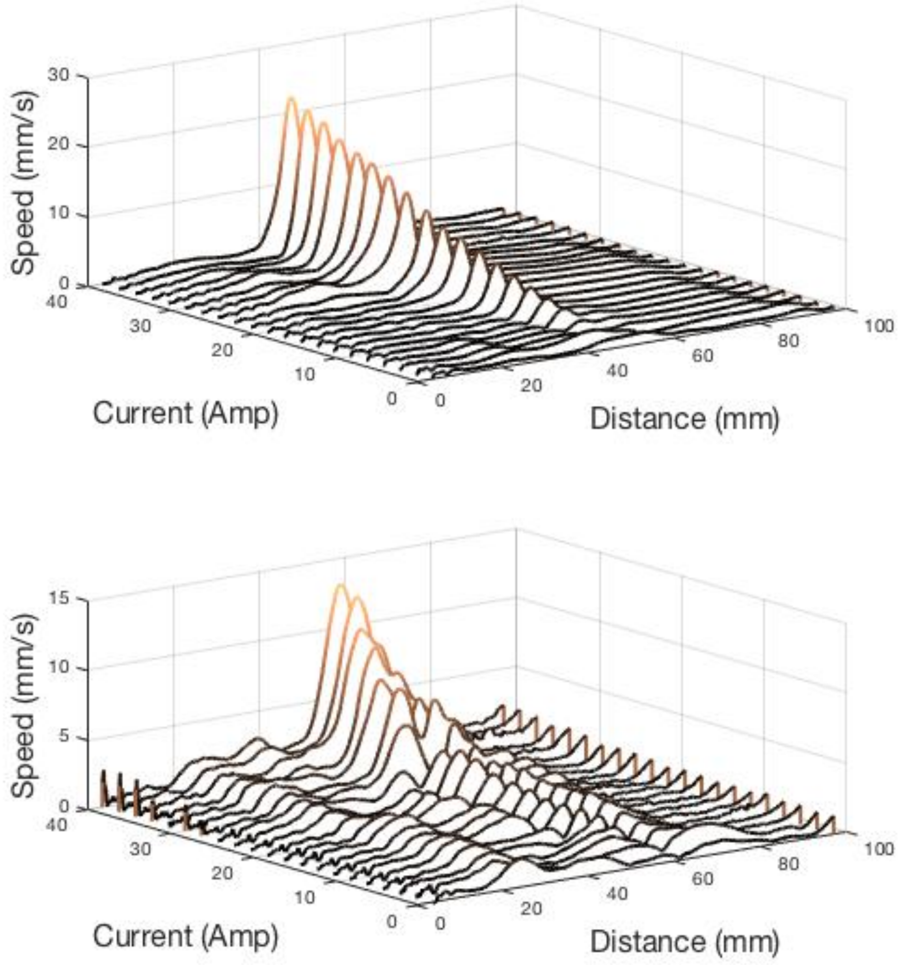

Figure 23 Root mean square of velocity at different currents for (top) wire connected from the side, and (bottom) wire connected from the bottom.

Figure 23 is the result of 42 ultrasound experiments in PbBi. Changing the wiring topology has a significant impact on both the onset of swirl, as well as the maximum flow speed. This is not surprising, since that the magnitude of the axial field from the side wire increases with increasing current density, whereas the magnitude of earth's field is constant. In the case where current topology was symmetric (figure 23 bottom), the onset of swirl occurred at 20 Amps instead of 10. To justify the delayed onset of swirl, we will look back to the numerical experiments of Davidson et al. [56] Turns out that the onset of transition a poliodal flow to swirl occurs when the ratio of azimuthal to poloidal force F_θ/F_p is on the order of 0.01. When the wiring around the electrode is symmetric, the azimuthal force comes from the interaction of earth's magnetic field with the radial current density passing within the electrode. Therefore, we attribute the delayed onset in symmetric wiring to the smaller azimuthal force magnitude F_θ compared to the case of side wiring. Numerical simulations done by our colleagues confirm the fact that Earth's field is able to excite swirling flow. [43] It is important to note that poliodal forcing comes from the combined action of thermal buoyant forces as well as electromagnetic forces. To the best of our knowledge, our experiments represent the first demonstration of the emergence of swirl in a thin layer of liquid metal where both buoyant and electromagnetic forces compete. Future work can perhaps explore the interaction of thermal convection, electro-vortex and swirl in a more quantitative manner. This would require computationally expensive simulations and large computing power.

Since that azimuthal swirl can emerge from external fields such as those from nearby wire or that of the earth, one would ask: is there a difference in the resulting flow speed? How does flow speed scale with increasing electrode current? To address these questions, we must determine how the velocity scales in each case. Following Davidson et al., [41,56] we employ the balance of torque. For a swirling flow in a steady state, the work done by the azimuthal force F_θ must be offset by viscous dissipation in the boundary layer:

$$\rho \iiint \mathrm{r}\, \mathrm{F}_\theta dV = \oint 2\, \pi r^2 \tau \, dl \qquad (3.15)$$

where $\tau = c_f \frac{1}{2} \rho u_\theta^2$ is the shear stress along the surface of the container, c_f is the skin friction coefficient, u_θ is the azimuthal flow velocity scale, and the volume integral is taken over the entire fluid. We can approximate the order of magnitude of the integrals by choosing a horizontal circle of radius R as the integral path. Then, by asserting that the left hand side scales as ~ ρ R F_θ, and the right hand side scales as ~ $\pi c_f \rho R^2 u_\theta^2$, we obtain

$$u_\theta \sim \sqrt{\frac{F_\theta}{\pi R c_f}} \qquad (3.16)$$

Here F_θ is the force per unit volume and is the result of the cross product of the internal current density **J** with an external field $\mathbf{B_z}$. In the case where the external field is that of the Earth, such that B_z = constant, then the resulting velocity would scale as

$$u_\theta \sim constant \times \sqrt{I} \qquad (3.17)$$

on the other hand, of the external field B_z is produced by the same current passing within the electrode, then the resulting velocity would scale as

$$u_\theta \sim constant \times I \qquad (3.18)$$

Taking the velocity at the center in figure 23 for both cases of symmetric and lateral wiring, we can plot the azimuthal velocity projection at different electrode current.

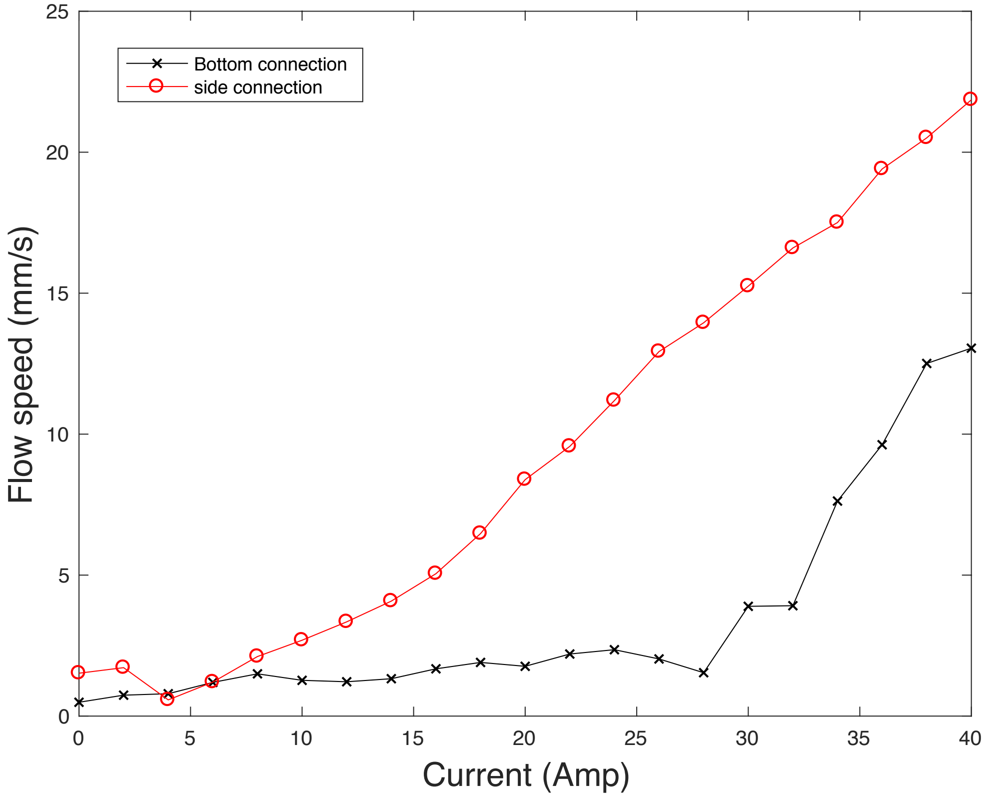

Figure 24 Azimuthal flow speed Vs. Electrode current for symmetric wiring (Black), and lateral wiring (Red).

In the case of lateral wiring (B_z depends on J), the resulting flow speed increases linearly with electrode current. However, the dependence is not as clear for the case of symmetric wiring (B_z is constant). In this case, we have to avoid falling for confirmation bias. Our mathematical analysis suggests square root dependence of flow speed on current, but our experimental results do not clearly reflect this. Hence, more data are required in order to make a more conclusive dependence of speed on current.

3.5 Summary & Engineering Implications

We started this chapter by looking at the forces that can initiate flow in a thin liquid metal electrode. We showed how electro-vortex and thermal convection compete, and developed a simple non-dimensional number to estimate their relative strength. Using ultrasound Doppler velocimetry in PbBi electrodes, we have shown that an intense azimuthal swirl can emerge in a shallow layer where both electromagnetic and buoyant forces are present. Azimuthal rotation emerges from the interaction of external axial fields with the internal radial current. The axial field can either be from nearby wire or even that of the earth. Our experiments used a very thin negative current collector. This allowed us to model the flow near the top surface as free-slip.

Just like any other battery system, the LMB pack is expected to have multiple cells that are connected in series to increase the voltage, and in parallel to increase the overall capacity. Since that we have shown that wiring topology can strongly influence the flow in individual cells, pack designers must carefully design internal wires to maintain uniform current and magnetic fields among individual cells. As an example, If a few cells have side wires that allows axial fields to develop, they would experience a different flow field, which in turn will cause variation in battery kinetics, and the direction of intermetallic growth (more on this subject in the next chapter).

Our model in this chapter focused on two competing phenomena. Namely, Rayleigh-Bénard convection and electro-vortex flow. However, there are other forces that can drastically influence the flow in LMB. Perhaps one of the most interesting is compositional convection. Since that the discharge anode material is much less dense than the cathode, the alloying reaction product is of intermediate density. This will probably lead to density stratification where the less dense products accumulate at the interface. Even more interesting would be to test the effect of our observed flows on the kinetics of LMBs.

“Science is nothing without generalizations. Detached and ill-assorted facts are only raw material, and in the absence of a theoretical solvent, have little nutritive value. At the present time and in some departments, the accumulation of material is so rapid that there is a danger of indigestion.”

Rayleigh (1884)

Chapter 4: Linking Electrochemistry and Fluid Dynamics

Indeed lord Rayleigh was right when he warned of the real danger of indigestion. In today's world, the accumulation of knowledge in the form of research papers has become the primary goal of many academic researchers and institutions. Scientists are valued based on the number research articles they produce and the prestigious journals they publish in. Because of this, many young researchers turn their backs on high-risk projects that might not result in handful of articles. To remove ourselves from this vicious cycle, we need to create more engineering "solvents", in which we can put our fundamental science into practical use. This is exactly the main purpose of this chapter. In the previous chapter we performed fundamental studies to understand how different flows compete and emerge. Here, our goal is to investigate the practical implications of flow on battery performance. The first section will give a brief overview of existing literature. The second section will give the governing equations followed by results and discussion.

4.1 Kinetics of mass transport in liquid metal batteries.

Oftentimes we hear the terms mass transport and fluid flow being used interchangeably. However, their meanings are different and are definitely not synonyms. Fluid flow can represent one mechanism by which mass can be transported. Other mechanisms include diffusion and migration.

Migration represents the motion of electrically charged species in the presence of an electric field. Not to be confused with electro-vortex flow described in chapter 3, migration describes motion on an atomic length scale. Such motion might be present in liquids containing charged (ionic) species such as the electrolyte, where positive and negatively charged ions can move under the influence of an applied electric field. On the other hand, diffusion refers to the motion and spreading of atoms and molecule in the presence of a concentration gradient.

Previous studies have often focused on diffusion. [24,36] The results of predicted transport losses from these numerical and analytic studies were in good agreement with experimentally observed profiles. However, these studies have often focused on small laboratory scale models where diffusion is surely the dominant form of transport. However, it is also worth mentioning that Barriga et al. have shown preliminary results of full 2D simulation of Navier-Stokes in Ca|Bi. [24] The simulations attempted to understand the effect of thermal convection on the concentration of Ca in Bi. A strong correlation between fluid flow and Ca concentration profile was observed, but the effect of flow on battery performance remained unclear. Hence, our work in this chapter will focus on how fluid flow affects the kinetics of LMBs. We will focus on the binary Li|Bi system mainly due to the availability of thermodynamic (EMF) measurements, and the well-documented material properties for the both the lithium, bismuth, as well as the molten salts. A schematic of the Li|Bi LMB is shown in figure 25 below.

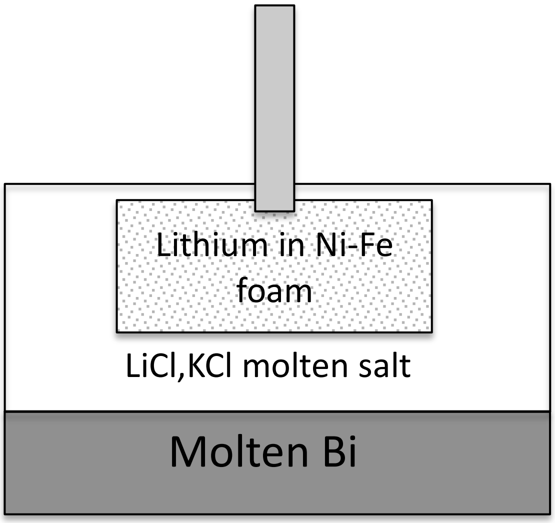

Figure 25 Schematic of Li|Bi cell at 400°C. Lithium is discharged from a Ni-Fe foam current collector.

Mass transport can affect the performance of the Li|Bi cell through the depletion of reactant concentration near the electrode-electrolyte interface. During discharge, Lithium ions that are near the bismuth layer are consumed in the alloying reaction to form $Li_{in\ Bi}$ or LiBi intermetallic. Knowing that each electron comes from the oxidation of one Li atom, we can use Faraday's law to determine the total amount of oxidized Li during a time period dt from passing a battery current I as

$$M = \frac{I\,dt}{n\,F} \tag{4.1}$$

Where M represents the total number of moles consumed during the reaction, n is the number of electrons exchanged in the reaction, and F is Faraday's constant (96485 coulombs/mole). As the reaction proceeds, more and more lithium is consumed near the electrode and large concentration gradient is formed. In the simple case where transport is driven by diffusion alone, the concentration near the electrode/electrolyte interface can be mathematically described by

$$c_{int} = c_b - \frac{J\,\delta}{n\,F\,D} \qquad (4.2)$$

where c_{int} is the reactant concentration at the interface, c_b is the bulk reactant concentration, δ is the thickness of the diffusion boundary layer, and J is the current density. [57]

Let us now consider the extreme case where the battery's current density is very large to the point where the interface concentration is completely depleted (c_{in}=0). The current density at which this situation occurs J_L is called the *limiting current density* and is calculated from

$$J_L = \frac{nFD\,c_b}{\delta} \qquad (4.3)$$

J_L represents the maximum current that the battery can operate at. Even though equation 4.3 represents the simple case where transport is driven by diffusion alone, there are two important things that that this equation can teach us. First, the simplest way to increase the limiting current density is to increase the concentration of reactants in the bulk c_b. Second, the higher the diffusivity and spreading of our active material, the higher J_L becomes.

To determine how the depletion of reactants or buildup of products affects the voltage of our battery, we have to go back to the Nernst equation, which when applied to our Li|Bi LMBs gives

$$E = -\frac{RT}{nF} \ln a_{Li\ (in\ Bi)} \qquad (4.4)$$

where R is the molar gas constant (R=8.314 J.mol^{-1}K^{-1}), T is the absolute temperature, and $a_{Li\ (in\ Bi)}$ is the chemical activity of lithium in bismuth. The accumulation of products near the interface causes a change in the chemical activity near the interface. This in turn gives rise to mass transport over-potential, which can be calculated by subtracting the surface potential from that of the bulk as

$$\eta_{mt} = E^{+} - E = \frac{-RT}{nF} \ln \frac{a_{Li\ (in\ Bi)}}{a^{+}_{Li\ (in\ Bi)}} \qquad (4.5)$$

where $a^{+}_{Li\ (in\ Bi)}$ is the chemical activity of lithium in bismuth near the electrode/electrolyte interface. From equation 4.5 we can see that the best way to eliminate transport over-potential altogether is by keeping the ratio $\frac{a_{Li\ (in\ Bi)}}{a^{+}_{Li\ (in\ Bi)}}$ as close as possible to unity. Physically, this means that we have make sure that concentration of Li is homogeneous within the electrode. To get a more quantitative measure of how a concentration gradient can affect our battery, we plotted the $\frac{a_{Li\ (in\ Bi)}}{a^{+}_{Li\ (in\ Bi)}}$ against the result transport over voltage in figure 26.

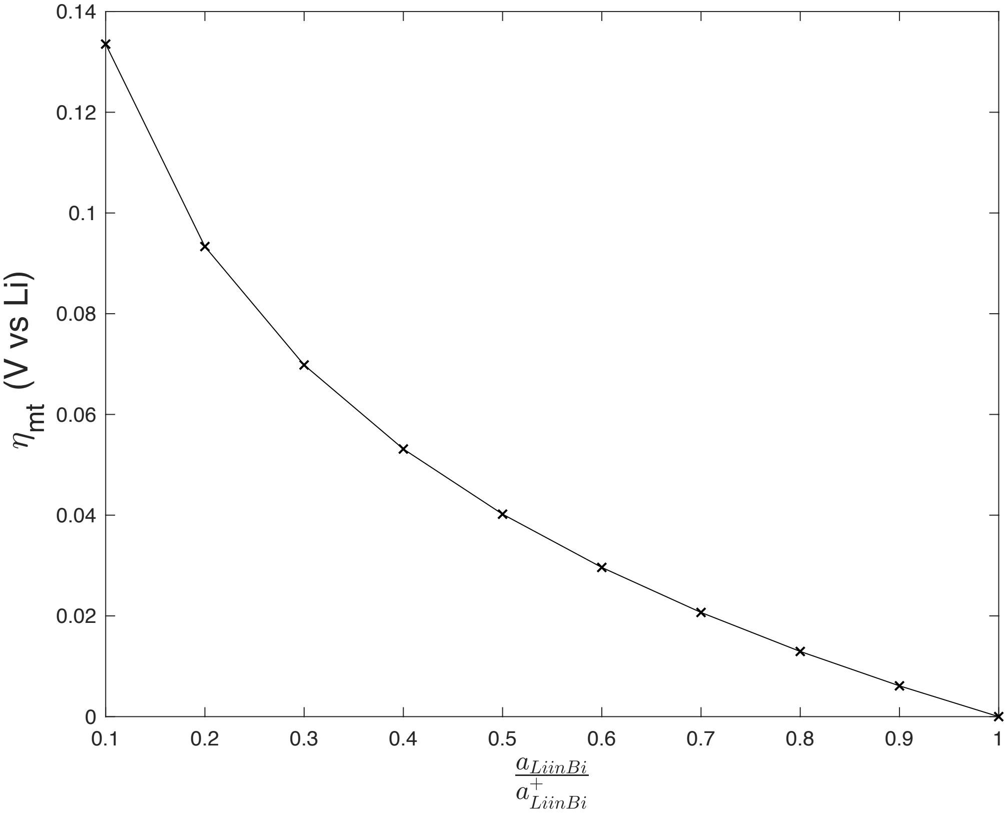

Figure 26 Transport over voltage η_{mt} vs. activity ratio $\frac{a_{Li\,(in\,Bi)}}{a^{+}_{Li\,(in\,Bi)}}$ at a temperature of 400^{o} C.

From figure 26, it is clear that the higher the activity near the interface relative to the bulk, the higher the overall transport over-voltage. This plot is simply the effect of varying the ratio of activity; it applies to both cases where transport is driven by diffusion or convection.

4.2 Convection-Diffusion in Li|Bi batteries

Our discussion so far has revolved around the kinetics of mass transport and how it affects the performance of LMBs in general. Let us now consider the Li|Bi system as a convection diffusion system where transport is driven by both convection and diffusion.

In this case, temporal changes in chemical concentration are governed by the convection-diffusion equation

$$\frac{\partial c}{\partial t} = \boldsymbol{\nabla} \cdot (D\boldsymbol{\nabla} c) - \boldsymbol{\nabla} \cdot (\boldsymbol{u}c) \qquad (4.6)$$

where c is the chemical concentration profile, D is the material diffusivity, and $\boldsymbol{u}$ is the velocity vector. It is a common practice among materials scientists to neglect flow altogether. This will lead to the well-known Fick’s law of diffusion. However, we know that it would be an unreasonable assumption to say that there’s no flow in liquid metal batteries. So the question here is: how do we get the velocity vector $\boldsymbol{u}$ in order to solve the convection-diffusion equation? In the previous chapter, we studied the effect of two competing forces, namely, buoyant forces that drive Rayleigh-Bénard convection and electromagnetic forces that drive electro-vortex flow. Combining all of these terms in the momentum equation gives

$$\frac{\partial \mathbf{u}}{\partial t} + (\mathbf{u} \cdot \nabla)\mathbf{u} = \nu \nabla^2\mathbf{u} - \frac{1}{\rho}\nabla \mathrm{p} + \frac{1}{\rho}(\boldsymbol{J} \times \boldsymbol{B}) - \mathrm{g}\beta \boldsymbol{\Delta T}\, \hat{\boldsymbol{z}} \quad (4.7)$$

One possible way to determine the velocity vector $\boldsymbol{u}$ is by coupling equations 4.7 and 4.6 and solving them sequentially. However, this is a very challenging task and requires high level of computing power. Fortunately, this is not what we are going to do in this chapter. Instead, we will follow a more simple approach where the flow is represented by a stream function (Ψ) as

$$\Psi = \sin\frac{n\,\pi x}{d}\sin\frac{m\,\pi y}{L} \qquad (4.8)$$

where n and m are integers that dictate the stream function, L and d are the diameter of the electrode its depth respectively, x and y are special coordinates. Our stream function (equation 4.8) is simply a mathematical expression that is used to represent flow field where the velocity vactor can be expressed as $\boldsymbol{u} = U\,(\boldsymbol{\nabla}\times\Psi)$ where U is a characteristic flow speed. Examples of stream functions generated by different values of n and m are shown in figure 27.

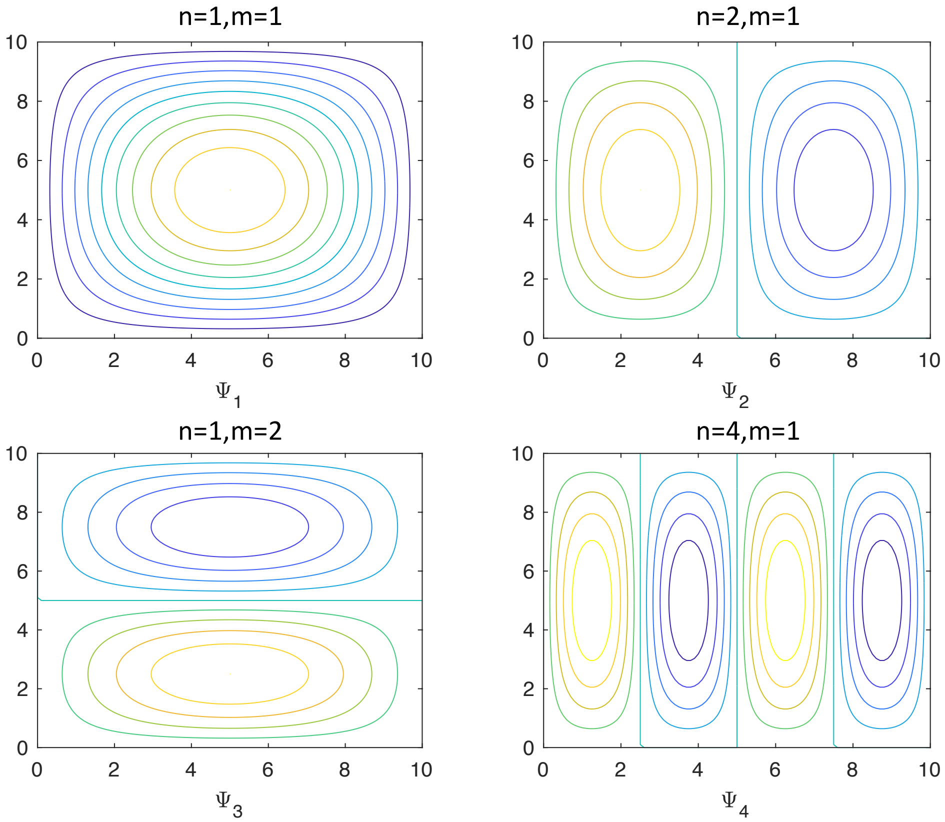

Figure 27 Examples of stream functions generated at different values of n and m.

From figure 27, we can clearly see that Ψ_2 with n=2 and m=1 represents two counter rotating rolls. This is very similar to our previous ultrasound experimental observed in figure 20. It is important to note that these stream functions are not solutions to the Navier-Stokes equation but we can use them approximate the flow in the positive electrode and generate a velocity vector $\boldsymbol{u} = U(\nabla \times \Psi)$.

4.3 Model Parameters

4.3.1 Geometry & Materials

Our model uses Li as a negative electrode and Bi as a positive electrode. We shall assume that the density of our Bi electrode remains constant during operation. That is, we will treat the flow as being incompressible ($\boldsymbol{\nabla} \cdot \boldsymbol{u} = 0$). The temperature is chosen to be 400°C in order to compare the outcome of this model with that of Newhouse et al. [36] Our Bi electrode has a thermal diffusivity $\alpha= 6.15 \times 10^{-6}$ m^2/s, a kinematic viscosity $\nu= 1.4 \times 10^{-7}$ m^2/s, and a thermal expansion coefficient $\beta=13.4 \times 10^{-6}$ K^{-1}. [34] To determine the thickness of our Bi electrode, we shall use the simple case where the Rayleigh number Ra is greater than 1100. Recall from chapter 3 that this value represents the onset of convection for a fluid in an infinite domain with one solid (no-slip) surface. Using the aforementioned parameters for Bi, we can calculate the Rayleigh number at different values of temperature gradients dT and electrode thicknesses.

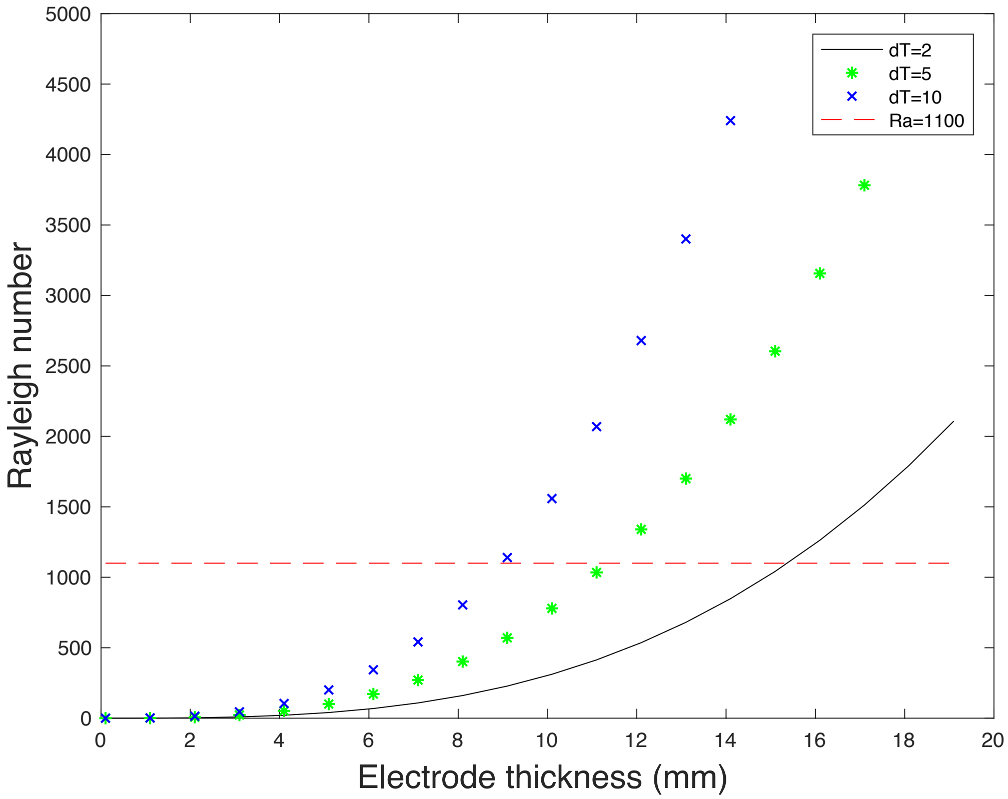

Figure 28 Calculated Rayleigh number for different values of temperature gradients (dT) specified in degrees C, and electrode thicknesses in mm. The red line represent the critical value of Ra=1100.

From figure 28, we can conclude that our electrode thickness should be at least 15 mm for an imposed temperature gradient of dT= 2^o C, or 9 mm for an imposed temperature gradient of 10^oC. In our mode we shall use the thickness L=15 mm since that it is also similar to the height used in some of our experiments while using a diameter of 100 mm.

The diffusivity of Li in Bi can be measured by Galvanostatic intermittent titration technique (GITT). For a recent study on diffusivity in liquid metals see Barriga et al., [24] and for a good introductory article on the theory behind GITT see Dibden et al. [58] Here, we shall use Newhouse's GITT results on Li-Bi inter-diffusivity at 400^oC. [36]

The diffusivity of Li is found to follow an exponential dependence on the molar fraction X_{Li}, which is mathematically described by

$$D = e^{\frac{(-36.57X_{Li}-4.27)}{(X_{Li}{}^{2}+3.07X_{Li}+0.5)}} \qquad (4.9)$$

and the molar concentration X_{Li} is calculated from

$$X_{Li} = \frac{[Li]}{[Li]+[Bi]} \qquad (4.10)$$

Where [Li] and [Bi] represent the molar concentration of Li and Bi respectively. Our electrolyte is composed of a eutectic mixture of 59.2% (mol) LiCl and 40.8% (mol) KCl which has a melting point of 340°C. The electrolyte has an ionic conductivity of $\sigma_e = 1.27$ S/cm and the bulk concentration of Li^+ is reported to be c_b= 0.015 mol/cm^3. [36,59,60] The diffusivity of lithium in the molten salt is D_e = 2.4x10^{-5} cm^2/s. [61] The thickness of the electrolyte is chosen to be 0.78 cm similar to that of Newhouse et al. [36]

4.3.2 Open Circuit Voltage

We have already stated that the main reason we chose this chemistry (Li|Bi) is because of the widely available electro-motive force (EMF) measurements. Weppner et al. have extensively studied this electrode couple back in 1976. [62] The authors used pulse coulometric titration in order to determine the open circuit voltage at different concentrations of Lithium in molten Bismuth. The measurement technique relies on a series of constant current pulses followed by along relaxation step. The observed shift in the voltage of the working electrode with respect to a known reference can be used to measure the diffusion constant D. The voltage after the relaxation step represents the EMF at a known concentration. This techniques was used to measure EMF of various electrode couples including Na|Bi, Li|Sb, Li|Bi-Sb and Li|Bi. [63–66] In our model, we shall use the EMF data from Weppner et al. [62] which was curve fitted by to give the following [36]:

$$E(X_{Li}) = \begin{cases} 0.67\, X_{Li}^{-0.1} & for\ X_{Li} < 0.35 \\ 0.75 & for\ 0.35 < X_{Li} < 0.74 \\ 0.05 & for\ X_{Li} \geq 0.74 \end{cases} \tag{4.11}$$

where E(X_{Li}) is the open circuit voltage in units of (Volts vs. Li) for a given molar concentration of X_{Li}.

4.3.3 Ohmic losses

According to Ohm's law, the resistance of the electrolyte produces a voltage drop equivalent to the product of total current I multiplied by the resistance R. In terms of current density, the ohmic drop can be written as

$$\eta_{IR} = \frac{L_e}{\sigma_e} J \tag{4.12}$$

where L_e is the thickness of the electrolyte and σ_e is its ionic conductivity. Our geometry in figure 4.1 shows Li being discharged from a foam current collector with smaller diameter. Since current density J is defined as total current per unit area, a natural question here is: which area should we use to represent the current density J? The work of Newhouse uses a somewhat strange expression where the total current density is written as $J=0.75\ J^{+} + 0.25\ J^{-}$, where J^{+} and J^{-} are the current densities defined with respect to the area of the positive and negative electrodes respectively. Clearly, this is non-physical and implies that current density lines spread drastically in the electrolyte layer. Since we know that electrons travel through the path of least resistance, we do not expect current density lines to spread in the electrolyte layer. Hence, a more realistic approximation is to simply use the area of the negative electrode to define the current density J.

4.3.4 Charge transfer over-potential

Charge transfer over-potential (η_{ct}) can be thought of as the voltage needed to increase the forward reaction rate by J. At thermodynamic equilibrium, the rate of forward and backward reactions is identical giving a net current density of J=0. This equilibrium rate is called the exchange current density (J_0). Charge transfer over-potential depends strongly on the exchange current density J_0. The higher the value of J_0, the faster the rate of electron transfer and the lower η_{ct} becomes. The mathematical expression for η_{ct} is given by

$$\eta_{ct} = \frac{RT}{nF}\frac{J}{J_0} \qquad (4.13)$$

In our Li-Bi system, the exchange current density J_0=60 A/cm^2. [67] The extremely high value of the exchange current density implies that η_{ct} is expected to be negligible. As an example, if the operating current density is 2A/cm^2 and the working temperature is 400^{o}C, the value of η_{ct} is 0.0019 V.

4.3.5 Volume Change

In this work we shall neglect any volume changes in the cathode that might influence the inter-electrode separation. To justify this assumption, let us try to estimate the change in the volume of Bi after alloying with Li. One possible method involves the calculation of the density of the new alloy from

$$\frac{1}{\rho_{alloy}} = \frac{1}{\rho_{Bi}}\,\frac{m_{Bi}}{m_{Bi}+\frac{MJt}{AnF}} + \frac{1}{\rho_{Li}}\,\frac{\frac{MJt}{AnF}}{m_{Bi}+\frac{MJt}{AnF}} \qquad (4.14)$$

where ρ_{Bi}, ρ_{Li} and ρ_{alloy} are the densities of the bismuth, lithium and their alloy respectively. m_{Bi} is the mass of Bi, M is the atomic weight of Li, A is the area of the electrode and t is discharge time. Note that we have used Faraday's law in equation 4.14

to determine the total mass of Li in Bi. The new volume is simply the total mass divided by the calculated density. Let us consider the example of J=0.2 A/cm^2 and a discharge time of 10 hours (t=10x3600 s), ρ_{Li} =0.5 g/cm^3, ρ_{Bi}= 10.05 g/cm^3. The mass of Bi required to fill a 1.5 cm layer of Bi in a 5 cm radius crucible is approximately m_{Bi} =1.1 kg. The density of the new alloy is ρ_{alloy}= 9.92 g/cm^3. Therefore the change in electrode height ΔL is

$$\Delta L = \frac{\frac{MJt}{AnF} + m_{Bi}}{\rho_{alloy} \times A} - 1.5\ cm = 0.014 \text{ cm} \qquad (4.15)$$

Here we used 1.5 cm as the original height of our electrode. Our approach is simple and does not take into account phase changes, surface tension, concentration gradients and other factors that are known to influence the volume of liquid metal alloys. However, our estimate shows that the increase in height is less than 0.9% and is therefore insignificant.

4.4 Results and Discussion

Our numerical solution employs an explicit, single step forward Euler numerical scheme for special derivatives and a multi-step (Adams-Bashforth) scheme for time derivatives. [69] The numerical solution has shown to be stable in the parameters used in this chapter. The spatial grid consists of 1000x10000 points in the vertical and horizontal directions respectively. The spatial grid spacing is Δx=Δy=0.01 mm and the time step in the numerical solver is set to Δt=5 ms. The first step after defining all the required material properties such as density, viscosity, etc. is to determine the flow field using $\boldsymbol{u} = U(\nabla \times \Psi)$. Where U is a characteristic flow speed (constant). The resulting flow field is shown below.

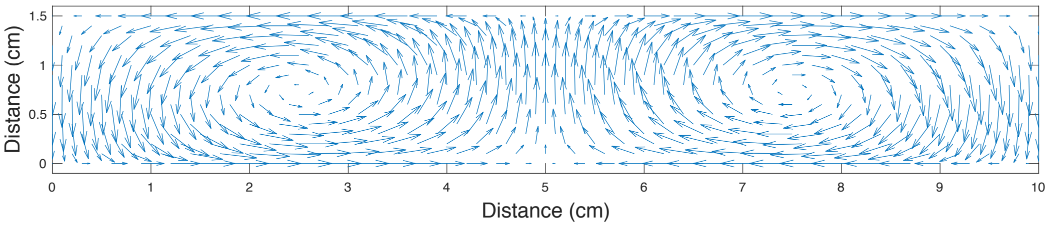

Figure 29 an axisymmetric vector flow field inside Bi electrode. Work of the Author, as published in reference [69]

The flow in figure 29 represents two counter rotating convection rolls similar to those observed in our ultrasound experiments in chapter 3. The flow speed is determined by the constant speed U. The stability condition of our convection-diffusion solver is set by the Courant number (C), which represents the ratio of the time step Δt to the numerical advection time as

$$C = \frac{U\,\Delta t}{\Delta x} \qquad (4.16)$$

Numerical stability is obtained when the Courant number C<1. This is known as the Courant-Friedrichs-Lewy (CFL) stability condition. [70] Note that increasing flow speed U would typically require a smaller time step in order to maintain numerical stability.

Let us now consider how this flow field affects the concentration gradient of Li in Bi. In figure 30, we solved the convection-diffusion equation for flow speeds of U=0, 0.5 and 1 mm/s. The current density is set to 200 mA/cm^2 and the total discharge time is 10^4 seconds. In absence of flow (U=0) the highest concentration of Li appears near the interface and is smoothly transported toward the bottom of the positive electrode. On the other hand, in the presence of thermal convection, Li$^+$ is advected by the flow along the top surface and toward the edges. Our convection-diffusion results show qualitative agreement with previous 2D simulations in Ca|Bi by Barriga et al. [24]

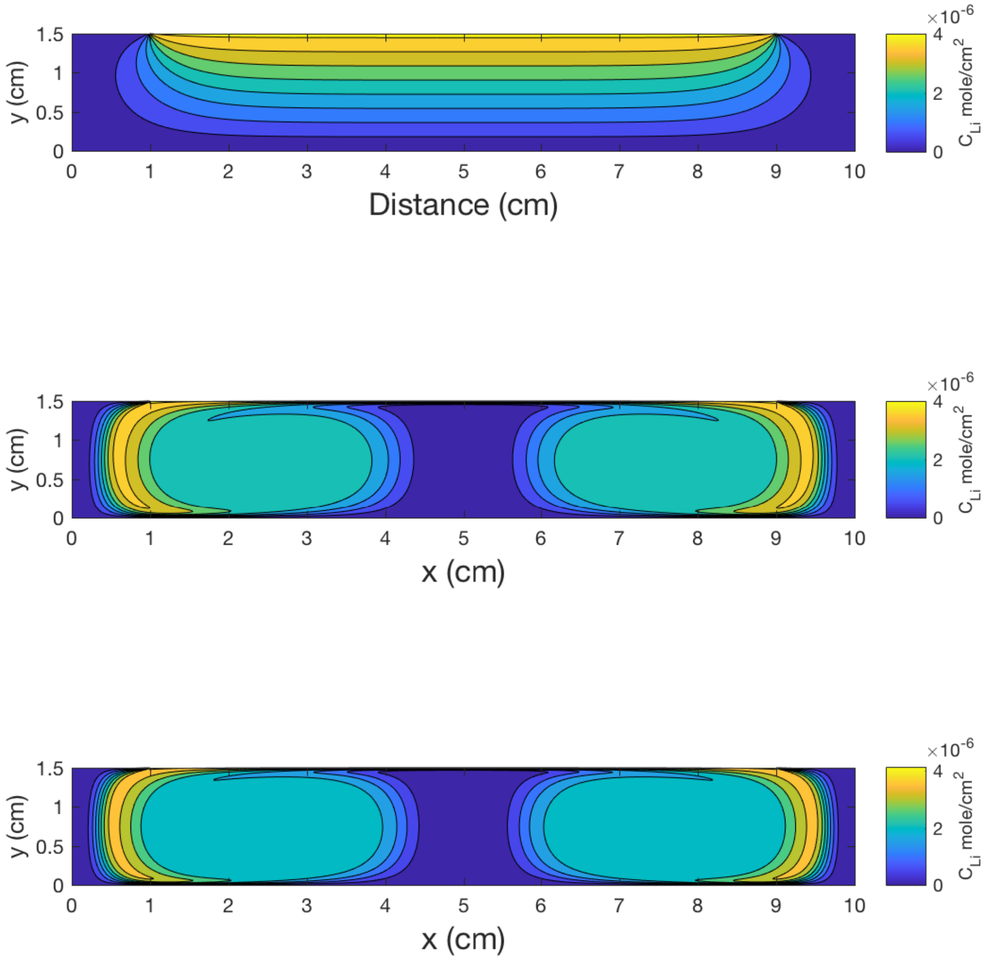

Figure 30 concentration of Li in Bi electrode where the characteristic flow speed U=0 (top), U=0.5 mm/s flow (middle) and U=1 mm/s flow (bottom). Work of the Author, as published in reference [69]

Doubling the flow speed from 0.5 to 1 mm/s did not seem to affect the overall concentration profile. In both cases the highest concentration appears along the interface and along the edges. As a result of the axisymmetric nature of the flow we observe a Li deprived region near the central axis. This depletion region is analogous to the centerline segregation that occurs during continuous casting. [71,72] Both phenomena are strongly influenced by the flow structure in metal melt. Another consequence of the flow structure is the slow filling of the center of vortices. The fast transport of Li along the edges is due to the action of advection, whereas motion toward the center is mainly driven by diffusion.

Since we have determined the concentration profile of Li in Bi, we can now calculate the time averaged transport over-voltage for different flow speeds. In figure 31, η_{mt} is calculated by subtracting the surface potential E^+ from that of the bulk E using equations 4.5 and 4.11.

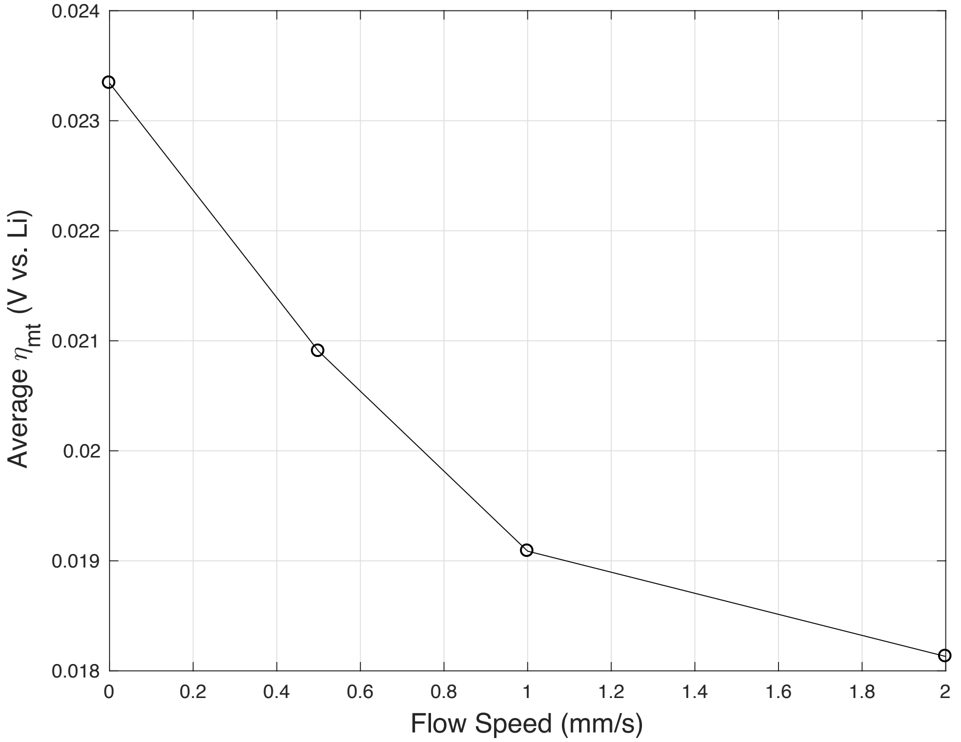

Figure 31 time averaged transport over-voltage vs. flow speed. η_{mt} is calculated from 4 separate simulation experiments, each having a total run time of $t=10^4$. Discharge current is kept at $J=200mA/cm^2$.

For an open circuit voltage of 0.75 V, the values in figure 31 represent a voltage drop on the order of 3%. On the other hand, for a negative current collector diameter of 6 cm and a current density of 200 mA/cm^2, the ohmic drop is expected to be 0.122 V, which represents a voltage drop of approximately 16%. We surely expect the average value of transport over-potential η_{mt} to increase with current density J, but so will the value of the ohmic drop η_{IR}. It is important to note that η_{mt} is not a constant value. That is, the values in figure 32 are the average of 10^4 seconds. To track its value with time, we plotted the instantaneous value of η_{mt} during the first 100 seconds.

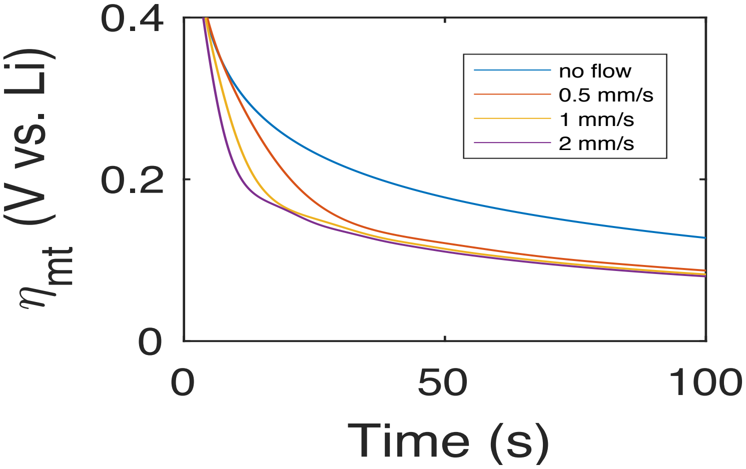

Figure 32 Transport over-voltage η_{mt} vs time for different characteristic flow speeds. Discharge rate is J=200mA/cm^2. Work of the Author, as published in reference [69]

Clearly, there is a significant difference between the instantaneous values of η_{mt} in figure 32 compared to the time averaged values in figure 31. During discharge, Li accumulates near the Bi/electrolyte interface, giving rise to high voltage drop (η_{mt}). Convection or diffusion then quickly drives discharge products away from the interface and into the bulk leading to a drop in the value of η_{mt}. [69] The faster the flow in the electrode, the faster discharge products can be removed from the interface and the lower the value of η_{mt} becomes.

4.4 Summary and Engineering Implications

A two-dimensional convection-diffusion model was developed. The model takes a velocity field as an input in the form of a stream function. Using first order finite difference for spatial derivatives and second order for time derivatives, we are able to obtain a numerically stable solution. The model was used to study the development of Li concentration under different flow speeds. Introducing flow changes the location where maximum Li concentration is observed. This would play an important role when predicting the location at which intermetallic LiBi or Li_3Bi nucleation starts. As an example, in the case where transport is driven by diffusion, nuclei are expected to form near the interface and grow uniformly into the positive electrode. On the other hand, when transport is driven by convection, growth is expected to occur more rapidly along the edges where the highest concentration of Li exists. This could lead to undesirable localized growth, which could ultimately lead to an electrical short.

The model was also used to investigate the effect fluid flow on the Li|Bi battery kinetics. Increasing flow speed seemed to decrease the overall transport over-voltage. However, due to the ability of Li to diffuse quickly through the Bi electrode as well as the Li_3Bi intermetallic, the overall mass transport over-voltage is not expected to be the dominant form of kinetic loss. For this particular system (Li|Bi), battery designers should focus more on methods to reduce the electrolyte thickness in order to reduce ohmic losses.

Chapter 5: Summary and Future Directions

The overarching goal of this work was to tackle engineering obstacles that are holding back the commercial development of liquid metal batteries. More specifically, this thesis explored possible ways to reduce the operating temperature through the use of low melting point eutectic salts. In chapter 2, we investigated the electrochemical feasibility of a novel amide ($NaNH_2$), hydroxide (NaOH), iodide (NaI) salt as low melting point electrolyte for sodium based liquid metal batteries. Using a three-electrode setup we measured the electrochemical window to be 1.3 V vs. Na. The limiting oxidation reaction was set by the formation of hydrazine gas (N_2H_4). Since N_2H_4 has a global market size of $350 million, it would be interesting to look at the economics of its electrolytic production from molten $NaNH_2$. [73] Using a second three-electrode setup, we showed that optimal operating conditions for a Na|PbBi battery employing this electrolyte are: 1) depth of discharge should be kept below 10% Na in PbBi to avoid severe volume changes and dendritic growth that could lead to electrical shorts. 2) Operating current density J should be kept below 100 mA/cm^2 for the same reason. Even though Na is one of the cheapest elements on the periodic table, the fact that we can only use 10% Na in PbBi means that our batteries must employ very large amounts of PbBi, which will drastically increases the total cost per kWh. Long term electrochemical cycling using amide based electrolytes has proved to be extremely challenging. This is due to the reaction of metallic sodium with the electrolyte to form sodium hydride (NaH) and nitrogen gas (N_2). This reaction can potentially be slowed down by the introduction of NaH powder into the electrolyte. However, careful temperature control is required since NaH can thermally decompose around 300^oC to release H_2 gas.

Besides the ternary amide based electrolyte, we also revisited the binary NaOH, NaI electrolyte. Using this electrolyte we built and cycled a Na|Bi LMB at a temperature of 280°C and a rate of 60 mA/cm^2. The binary electrolyte appears to be more compatible with molten Na. This stability is attributed to the self-inhibiting reaction of Na with NaOH to form a thin layer of Na_2O. This reaction was shown to be spontaneous and is responsible for the rapid capacity fade observed in our batteries. Here, future research might look into methods to mitigate the growth of the passive Na_2O layer.

In chapter 3, we focused on fluid flow in the positive electrode of a Na|PbBi LMB. Our experiments were performed at a temperature range between 160-180 °C. The main objective was to understand how fluid flow is affected by operating conditions such as: current density, which drives electro-vortex flow, and temperature gradients, which drive thermal convection. Both thermal convection and electro-vortex flow were found to compete. Using the characteristic speed of both phenomena, we derived a simple dimensionless ratio that predicts the range at which one will dominate over the other. Based on our experimental results, dimensionless analysis and the recent numerical simulations by our collaborators, we expect thermal convection to be the dominant flow phenomenon.[43] Of course this statement is only valid when no chemical reactions, surface tension or phase changes occur in the positive electrode. Future models will definitely have to be more complicated in order to identify the effect of each of the aforementioned phenomena. Perhaps this is another area where numerical simulations are more powerful.

In the same chapter, we also showed that the topology and feeding lines of electrical current could drastically influence the flow structure within the electrode. The axial magnetic field (B_z) that results from side wires can interact with the small radial current density component (J_r). The result is an azimuthal force that can drive a swirling, tornado-like flow in the positive electrode. Our experimental model showed that this axial field might either come from nearby wires, or even from that of the earth. Furthermore, our results indicate a transition from poloidal to swirling flow occurs at a total current of 10A from the case of asymmetric wiring (B_z from side wire + earth), and 20A for symmetric (B_z from earth). Even though we have not observed any surface deformation in PbBi electrode with diameters less than 100 mm, larger commercial cells and larger operating current densities might be in danger of surface deformations as a result of intense swirling flow. Hence, it is important to maintain consistent current topology when connecting multiple cells to form a pack.

In chapter 4, we built a two-dimensional convection-diffusion model that links electrochemical kinetics to fluid dynamics. The poloidal flow that was experimentally observed in chapter 3 is represented by a stream function. Using this flow field along with other material properties as inputs, we numerically solved the convection diffusion equation for Li^+ in Bi electrodes. When transport is driven by convection, the maximum concentration appeared near the interface and along the edges. Our results show qualitative agreement with the simulations of Barriga et al. even though their model uses the full Navier-Stokes for Ca^+ in Bi. In addition to studying the effect of flow in concentration profiles, we also looked at how fluid flow affect the kinetics of Li|Bi batteries. Increased flow speed was found to reduce the overall transport over-voltage. Nonetheless, the overall transport over-voltage was very low and at a rate of $200 mA/cm^2$ it represented a voltage drop on the order of 3%. On the other hand, ohmic losses and charge transfer over-voltage represented a voltage drop of 16% and 0.03% respectively. Our results indicate that the dominant mechanism for voltage losses is the high ohmic resistance of the electrolyte. The high resistance is mainly due to the use of a thick electrolyte layer in order to prevent the two electrodes from coming in contact. For this chemistry (Li|Bi), research should focus on identifying possible methods to reduce the electrolyte thickness and reduce the overall ohmic losses.

References

[1] Electricity in the united states, (n.d.). https://www.eia.gov/energyexplained/index.cfm?page=electricity_in_the_united_states (accessed January 5, 2017).

[2] U.S. Department of Energy, Grid Energy Storage, 2013. http://energy.gov/sites/prod/files/2014/09/f18/Grid Energy Storage December 2013.pdf.

[3] B.L. Spatocco, Investigation of Molten Salt Electrolytes for Low-Temperature Liquid Metal Batteries by, (2015).

[4] H. Kim, D.A. Boysen, J.M. Newhouse, B.L. Spatocco, B. Chung, P.J. Burke, et al., Liquid Metal Batteries : Past , Present , and Future, Chem. Rev. (2013) 2075–2099.

[5] K. Wang, K. Jiang, B. Chung, T. Ouchi, P.J. Burke, D. a. Boysen, et al., Lithium–antimony–lead liquid metal battery for grid-level energy storage, Nature. 514 (2014) 348–350. doi:10.1038/nature13700.

[6] S. Matteson, E. Williams, Learning dependent subsidies for lithium-ion electric vehicle batteries, Technol. Forecast. Soc. Change. 92 (2015) 322–331. doi:10.1016/j.techfore.2014.12.007.

[7] C. Curry, Lithium-Ion battery Costs and Market, 2017. https://data.bloomberglp.com/bnef/sites/14/2017/07/BNEF-Lithium-ion-battery-costs-and-market.pdf.

[8] M. Faraday, Experimental Researches in Electricity, Philos. Trans. R. Soc. London. 122 (1832) 125–162. doi:10.1098/rstl.1832.0006.

[9] M. Faraday, The fundamental laws of electrolytic conduction: memoirs, University of California Libraries, 1899.

[10] S. Ross, Faraday Consults the Scholars: The Origin of the Terms of Electrochemistry, in: Ninet. Attitudes Men Sci., 1991: pp. 126–172.

[11] M. Root, The TAB Battery Book, 2010. doi:10.1036/9780071739917.

[12] Global Market Insight, Lithium Ion Battery Market Size By Technology, 2017. https://www.gminsights.com/industry-analysis/lithium-ion-battery-market.

[13] J.M. Tarascon, M. Armand, Issues and challenges facing rechargeable lithium batteries., Nature. 414 (2001) 359–367. http://www.ncbi.nlm.nih.gov/pubmed/11713543.

[14] NGK Insulators, (n.d.). http://www.ngk.co.jp/english/announce/111031_nas.html (accessed July 6, 2017).

[15] D.J. Bradwell, Liquid Metal Batteries: Ambipolar Electrolysis and Alkaline Earth Electroalloying Cells by, (2011) 1–206.

[16] D.J. Bradwell, H. Kim, A.H.C. Sirk, D.R. Sadoway, Magnesium–Antimony Liquid Metal Battery for Stationary Energy Storage, J. Am. Chem. Soc. 134 (2012) 1895–1897. doi:10.1021/ja209759s.

[17] K. Wang, K. Jiang, B. Chung, T. Ouchi, P.J. Burke, D. a. Boysen, et al., Lithium–antimony–lead liquid metal battery for grid-level energy storage, Nature. 514 (2014) 348–350. doi:10.1038/nature13700.

[18] X. Ning, S. Phadke, B. Chung, H. Yin, P. Burke, D.R. Sadoway, Self-healing Li–Bi liquid metal battery for grid-scale energy storage, J. Power Sources. 275 (2015) 370–376. doi:10.1016/j.jpowsour.2014.10.173.

[19] B.L. Spatocco, T. Ouchi, G. Lambotte, P.J. Burke, D.R. Sadoway, Low-Temperature Molten Salt Electrolytes for Membrane-Free Sodium Metal Batteries, J. Electrochem. Soc. 162 (2015) A2729–A2736. doi:10.1149/2.0441514jes.

[20] Battery startup Ambri cuts staff, pushes back first sales | Fortune.com, (n.d.). http://fortune.com/2015/09/11/liquid-metal-battery-layoffs/ (accessed June 10, 2017).

[21] R.F. Ashour, H. Yin, T. Ouchi, D.H. Kelley, D.R. Sadoway, Molten Amide-Hydroxide-Iodide Electrolyte for a Low-Temperature Sodium-Based Liquid Metal Battery, J. Electrochem. Soc. 164 (2017) A535–A537. doi:10.1149/2.1451702jes.

[22] H. Kim, D. a. Boysen, T. Ouchi, D.R. Sadoway, Calcium-bismuth electrodes for

large-scale energy storage (liquid metal batteries), J. Power Sources. 241 (2013) 239–248. doi:10.1016/j.jpowsour.2013.04.052.

[23] D.J. Bradwell, H. Kim, A.H.C. Sirk, D.R. Sadoway, Magnesium-antimony liquid metal battery for stationary energy storage, J. Am. Chem. Soc. 134 (2012) 1895–1897. doi:10.1021/ja209759s.

[24] S.A. Barriga, An Electrochemical Investigation of the Chemical Diffusivity in Liquid Metal Alloys, massachusetts institute of technology, 2013.

[25] R.P. Feynman, R.. Leighton, M. Sands, The Feynamn Lectures on Physics, Addison-Wesley, Reading, MA, 1963.

[26] E. Yeager, Fuel Cells: Basic Considerations, in Power Sources Division, in: Proc. 12th Annu. Batter. Res. Dev., Fort Monmouth, NJ, 1958.

[27] C.E. Crouthamel, H.L. Recht, Regenerative EMF Cells, 1967. doi:10.1021/ba-1967-0064.

[28] A.D. Cairns, E.J. , Crouthamel, C.E. , Fischer, A.K. , Foster, M.S. , Hesson, J.C. , Johnson, C.E. , Shimotake, H. , Tevebaugh, Galvanic cells with fused electrolytes, Chicago, 1967. doi:ANL-7316.

[29] C.-C. Lalau, A. Ispas, A. Bund, Sodium-bismuth-lead low temperature liquid metal battery, J. Electrochem. Plat. Technol. (2015). doi:10.1007/s13228-014-0037-9.

[30] V.P. Yurkinskii, E.G. Firsova, S.A. Proskura, Thermal dissociation of sodium hydroxide upon evacuation, Russ. J. Appl. Chem. 78 (2005) 360–362. doi:10.1007/s11167-005-0296-x.

[31] C.W. Bale, E. Bélisle, Fact-Web suite of interactive programs, (n.d.). http://www.crct.polymtl.ca/factweb.php (accessed November 2, 2018).

[32] S. Eidensohn, Fuel cell system, US3057946, 1959. https://www.google.com.na/patents/US3057946 (accessed February 13, 2018).

[33] N. Watanabe, S. Yoshizawa, T. Morimoto, M. Miura, Y. Yamada, Production of alkali metals from alkali amalgam, U.S. 3,265,490, 1966.

[34] J. Pacio, Eutectic Alloy and Lead Properties , Materials Compatibility , Thermal-hydraulics and Technologies 2015 Edition H andbook on Lead-bismuth, 2015.

[35] F. Breda, P. Jonville, A. Bonomi, J. Ambert, Salt composition usable as a fused electrolyte in accumulators, US-4287270, 1980.

[36] J.M. Newhouse, Modeling the Operating Voltage of Liquid Metal Battery Cells by, massachusetts institute of technology, 2014.

[37] N. Weber, V. Galindo, J. Priede, F. Stefani, T. Weier, The influence of current collectors on Tayler instability and electro-vortex flows in liquid metal batteries, Phys. Fluids. 27 (2015) 014103. doi:10.1063/1.4905325.

[38] F. Stefani, T. Weier, T. Gundrum, G. Gerbeth, How to circumvent the size limitation of liquid metal batteries due to the Tayler instability, Energy Convers. Manag. 52 (2011) 2982–2986. doi:10.1016/j.enconman.2011.03.003.

[39] W. Herreman, C. Nore, L. Cappanera, J.-L. Guermond, Tayler instability in liquid metal columns and liquid metal batteries, J. Fluid Mech. 771 (2015) 79–114. doi:10.1017/jfm.2015.159.

[40] N. Weber, V. Galindo, F. Stefani, T. Weier, Current-driven flow instabilities in large-scale liquid metal batteries, and how to tame them, J. Power Sources. 265 (2014) 166–173. doi:10.1016/j.jpowsour.2014.03.055.

[41] P.A. Davidson, An Introduction to Magnetohydrodynamics, Cambridge University Press, 2001.

[42] O. Zikanov, Metal pad instabilities in liquid metal batteries, (2015) 1–19. http://arxiv.org/abs/1508.04474.

[43] R.F. Ashour, D.H. Kelley, A. Salas, M. Starace, N. Weber, T. Weier, Competing forces in liquid metal electrodes and batteries, J. Power Sources. 378 (2018) 301–310. doi:10.1016/j.jpowsour.2017.12.042.

[44] Y. Shen, O. Zikanov, Thermal convection in a liquid metal battery, Theor. Comput. Fluid Dyn. 30 (2016) 275–294. doi:10.1007/s00162-015-0378-1.

[45] D.H. Kelley, D.R. Sadoway, Mixing in a liquid metal electrode, Phys. Fluids. 26 (2014). doi:10.1063/1.4875815.

[46] K. Thomas, T. Boeck, Thermal Rayleigh-Marangoni convection in a three-layer liquid-metal-battery model, (2016) 1–26.

[47] D.H. Kelley, T. Weier, Fluid Mechanics of Liquid Metal Batteries, 70 (2017). doi:10.1115/1.4038699.

[48] J.E. Wesfreid, Henri Bénard: Thermal convection and vortex shedding, Comptes Rendus Mécanique. 345 (2017) 446–466. doi:10.1016/J.CRME.2017.06.006.

[49] P. Kundu, I. Cohen, D. Dowling, Fluid Mechanics, 5th ed., Elsevier, 2012. http://store.elsevier.com/Fluid-Mechanics/Pijush-Kundu/isbn-9780124059351/.

[50] B.F. Edwin Northrup, SOME NEWLY OBSERVED MANIFESTATIONS OF FORCES IN THE INTERIOR OF AN ELECTRIC CONDUCTOR., Phys. Rev. (Series I). 24 (1907). https://journals.aps.org/pri/pdf/10.1103/PhysRevSeriesI.24.474 (accessed March 7, 2018).

[51] E. Induced, V. Flows, Electrically Induced Vortical Flows . By V . BOJAREVICS , 208 (1989) 657–659.

[52] J.A. Shercliff, Fluid motions due to an electric current source, J. Fluid Mech. 40 (1970) 241. doi:10.1017/S0022112070000150.

[53] V. Bojarevics, E. V. Shcherbinin, Azimuthal rotation in the axisymmetric meridional flow due to an electric-current source, J. Fluid Mech. 126 (1983) 413. doi:10.1017/S0022112083000245.

[54] S.C. Flood, P.A. Davidson, Natural convection in aluminium direct chill cast ingot, Mater. Sci. Technol. 10 (1994) 741–751. doi:10.1179/mst.1994.10.8.741.

[55] U. Burr, U. Müller, Rayleigh–Bénard convection in liquid metal layers under the influence of a horizontal magnetic field, J. Fluid Mech. 453 (2002) 345–369. doi:10.1017/S002211200100698X.

[56] P. a. Davidson, D. Kinnear, R.J. Lingwood, D.J. Short, X. He, The role of Ekman pumping and the dominance of swirl in confined flows driven by Lorentz forces, Eur. J. Mech. - B/Fluids. 18 (1999) 693–711. doi:10.1016/S0997-7546(99)00106-5.

[57] W.G.C. Ryan O'hayre, Suk-Won Cha, Fuel Cell Fundamentals, 2016. doi:10.1017/CBO9781107415324.004.

[58] J.W. Dibden, N. Meddings, J.R. Owen, N. Garcia-Araez, Quantitative Galvanostatic Intermittent Titration Technique for the Analysis of a Model System with Applications in Lithium–Sulfur Batteries, ChemElectroChem. 5 (2018) 445–454. doi:10.1002/celc.201701004.

[59] P. Masset, R.A. Guidotti, Thermal activated (thermal) battery technology, J. Power Sources. 164 (2007) 397–414. doi:10.1016/j.jpowsour.2006.10.080.

[60] P. Masset, R.A. Guidotti, Thermal activated (thermal) battery technology. Part II. Molten salt electrolytes, J. Power Sources. 164 (2007) 397–414. doi:10.1016/j.jpowsour.2006.10.080.

[61] I. Okada, F. Lantelme, A new interpretation of the original data of Chemla's group on the mobilities of binary molten system (Li, K)Br, J. New Mater. Electrochem. Syst. 9 (2006) 165–174.

[62] W. Weppner, R.A. Huggins, Thermodynamic Properties of the Intermetallic Systems Lithium‐Antimony and Lithium‐Bismuth, J. Electrochem. Soc. 125 (1978) 7–14. doi:10.1149/1.2131401.

[63] T. Dai, Y. Zhao, X.-H. Ning, R. Lakshmi Narayan, J. Li, Z. Shan, Capacity extended bismuth-antimony cathode for high-performance liquid metal battery, J. Power Sources. 381 (2018) 38–45. doi:10.1016/J.JPOWSOUR.2018.01.048.

[64] A. Petric, A.D. Pelton, M.L. Saboungi, W.F. Calaway, P.J. Tumidajski, A. Petric, et al., Dilute solutions of sodium in molten bismuth and tin : EMF measurements and interpretation, J. Phys. F Met. Phys. (1983).

[65] M.-L. Saboungi, T.P. Corbin, N.A.J. and C.P. Bartlett H E, N.A.J. and C.P. Bartlett H E, B.A.B. and T.D. E, de B.F.R. and M.A.R. Boom R, et al., Dilute solutions of sodium in molten bismuth and tin: EMF measurements and interpretation, J. Phys. F Met. Phys. 14 (1984) 13–21. doi:10.1088/0305-4608/14/1/004.

[66] W. Weppner, R.A. Huggins, Thermodynamic Properties of the Intermetallic

Systems Lithium-Antimony and Lithium-Bismuth, 125 (1976).

[67] J.M. Newhouse, D.R. Sadoway, Charge-Transfer Kinetics of Alloying in Mg-Sb and Li-Bi Liquid Metal Electrodes, J. Electrochem. Soc. 164 (2017) A2665–A2669. doi:10.1149/2.1571712jes.

[68] Y.A. Chen, I.N. Bandeira, D.M. Rowe, An exact density formula for substitutional solid solution alloys, J. Mater. Sci. Lett. 13 (1994) 1051–1053. https://link.springer.com/content/pdf/10.1007/BF00277036.pdf (accessed April 5, 2018).

[69] R.F. Ashour, D.H. Kelley, Convection-Diffusion Model of Lithium-Bismuth Liquid Metal Batteries, Mater. Process. Fundam. (2018) 41–52.

[70] R. Courant, K. Friedrichs, H. Lewy, �ber die partiellen Differenzengleichungen der mathematischen Physik, Math. Ann. 100 (1928) 32–74. doi:10.1007/BF01448839.

[71] I. Jin, L.R. Morris, J.D. Hunt, Centerline Segregation in Twin-Roll-Cast Aluminum Alloy Slab, JOM. 34 (1982) 70–75. doi:10.1007/BF03338033.

[72] S.R. Wagstaff, Jet processing of direct chill cast aluminum ingots, 2017.

[73] Hydrazine Hydrate Market Size - Industry Share Report 2024, (n.d.). https://www.gminsights.com/industry-analysis/hydrazine-hydrate-market (accessed April 13, 2018).

[74] V. Giordani, D. Tozier, H. Tan, C.M. Burke, B.M. Gallant, J. Uddin, et al., A Molten Salt Lithium-Oxygen Battery, J. Am. Chem. Soc. 138 (2016) 2656–2663. doi:10.1021/jacs.5b11744.

[75] B.J. Cabana, L. Monconduit, D. Larcher, M.R. Palacín, Beyond Intercalation-Based Li-Ion Batteries : The State of the Art and Challenges of Electrode Materials Reacting Through Conversion Reactions, (2010) 170–192. doi:10.1002/adma.201000717.

[76] C.-H. Li, P. Sengodu, D.-Y. Wang, T.-R. Kuo, C.-C. Chen, Highly stable cycling of a lead oxide/copper nanocomposite as an anode material in lithium ion batteries, RSC Adv. 5 (2015) 50245–50252. doi:10.1039/C5RA07948A.

Appendix A: Alternative Chemistries and Unfinished Work

A.1 The Li|$LiNO_3$,KNO_3| PbBi system

A three-electrode setup similar to that in chapter 2 was used to study the feasibility of low temperature nitrate salts as electrolyte for Li based liquid metal batteries. Nitrate salts are attractive due to their low cost, low melting point < 150 °C and good thermal stability above 500°C. The salts were dried under vacuum at a temperature of 150° for 12 hours before being transferred into an argon filled glove box. The electrochemical window of this electrolyte has already been measured in the literature by Giordani et al. and is 3.8 Volt Vs. Li [74]. Our goal here is to test the feasibility of this electrolyte in a Li|PbBi electrochemical cell at 150°C. Note that at while PbBi is liquid at this temperature, Li is still solid. Hence this represents a multiphase (solid+liquid) metal battery. A schematic of our three-electrode setup is shown in figure 33, and electrochemical cycling data are shown in figure 34.

Here we observe two striking differences when compared to other Li based salts. One is the unexpected high voltage (>2V), which might result from the reaction of Bi with $LiNO_3$ to form Bi_2O_3 as

$$3LiNO_3+6Bi \rightarrow 3Bi_2O_3+Li_3N+N_{2(g)} \qquad (A.1)$$

Reaction A.1 is spontaneous and its associated free energy is -472.6 kJ. This could explain both the high voltage and the complete passivation after the first discharge. The observed cycling performance is closer to that of the Li|Bi_2O_3 primary battery than that of Li|Bi or Li|Pb secondary LMBs.

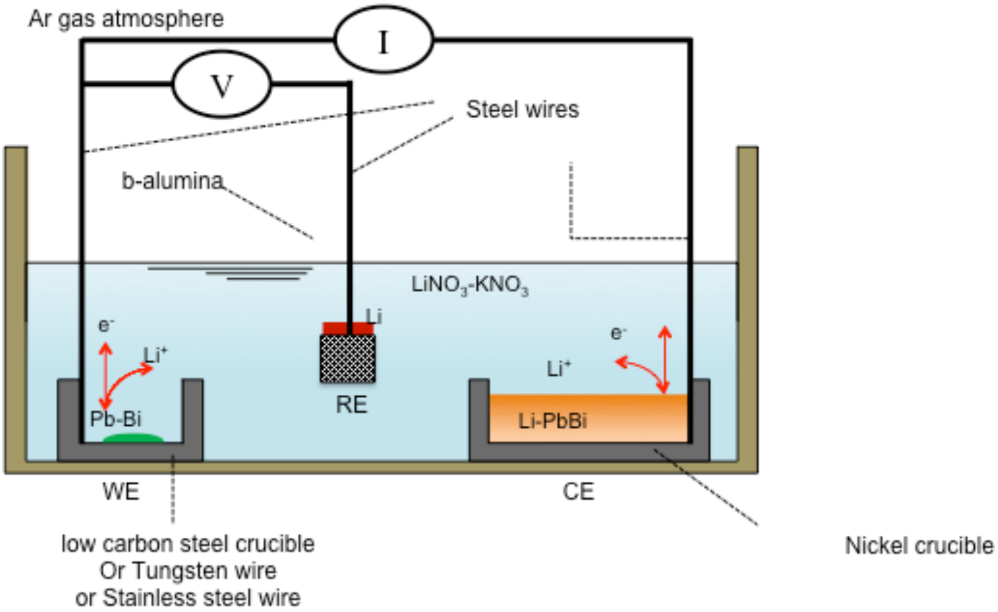

Figure 33 Three-electrode setup with solid Li in Ni-Fe foam reference electrode, a PbBi eutectic as a working electrode, and a 10% Li in PbBi as a counter electrode.

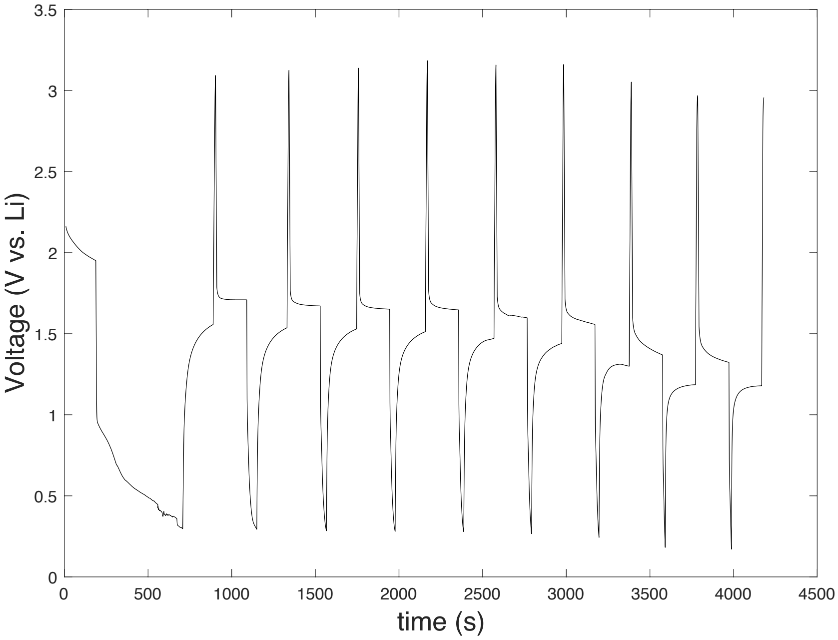

Figure 34 Electrochemical cycling using three-electrode setup described previously and a voltage limits of 0.05 and 3V vs. Li. Working electrode passivation occured after first discharge.

A.2 The Li | MO system

In this section we describe a novel battery, which operates through the formation and decomposition of Li_2O. The negative electrode employs Li metal in either liquid or solid state depending on the operating temperature. The electrolyte is composed of lithium containing molten salts, and the cathode is composed of a metal oxide (MO), where M can be Pb, Fe, Cu, Co or Mn. The half-cell electrode reactions are

$$2Li \rightarrow 2Li^+ + 2e^- \qquad \text{(anode)}$$
$$MO + 2Li^+ + 2e^- \rightarrow Li_2O + M \qquad \text{(cathode)}$$
$$2Li + MO \leftrightarrow Li_2O + M \qquad \text{(Overall)}$$

Depending on the chosen transition metal oxide and the operating temperature, the open circuit voltage of the battery is expected to be between 2 to 3 Volts. This battery concept has come to be known as a conversion battery. Such battery can have capacities in excess of 1000 Ah/kg compared to graphite based lithium-ion batteries 372 Ah/kg.[75]

The first cathode material we tested is PbO. This is mainly due to its low cost, and good theoretical capacity (582 Ah/kg). Previous work has already demonstrated the feasibility and stability of PbO as an anode in lithium ion batteries. [76] However, here we shall use PbO as a cathode, molten Li metal as an anode and a eutectic LiCl, KCl electrolyte. An example of electrochemical cycling of a full Li|LiCl,KCl|PbO cell operating at 400°C and a rate of 50A/kg, where to the rate is defined in terms the weight of active material PbO. Our cell works as a proof of concept and displays coulombic efficiencies up to 80%. However the measured energy efficiency was less than 40%. This is due to the use of a thick electrolyte layer (< 2cm) and the lack of conductive additives in the cathode.

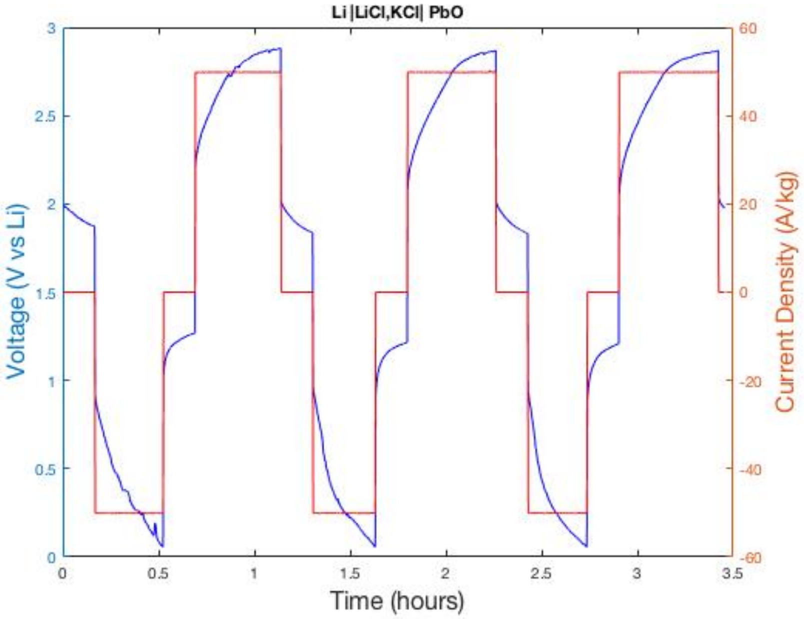

Figure 35 Electrochemical cycling of a membrane free Li|LiCl,KCl|PbO cell at 400°C. Voltage limits are 0.01 and 2.8V.

Another cathode materials that was tested is CuO. Due its extremely low cost and high theoretical capacity of 674 Ah/kg, and high open circuit voltage >2V, CuO is an attractive cathode material especially for grid scale storage applications where cost is king. Figure 36 shows an example of cycling performance of Li|LiCl,KCl|CuO battery at 400°C and a rate of 200 A/kg. Several batteries were tested during the course of this study. In general, CuO displayed better performance compared to PbO. Capacities in excess of 300 A/kg were obtained with CuO cathodes.

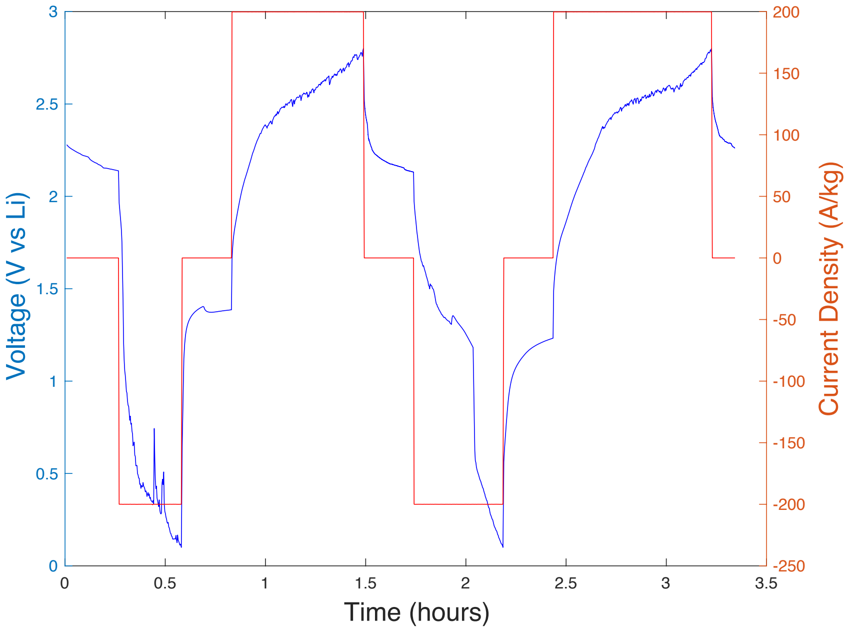

Figure 36 Electrochemical cycling of a membrane free Li|LiCl,KCl|CuO cell at 400°C. Voltage limits are 0.01 and 2.8V.

Current challenges with this Li|MO battery include: 1) Poor electrical conductivity of MO cathodes. 2) Dispersion of Li_2O in the molten salt electrolyte. Therefore, possible ways to overcome these challenges include increasing the conductivity of the cathode and using a ceramic separator to prevent the dispersion of Li_2O.